Universidad de Antioquia
Facultad de Ciencias Exactas y Naturales
Instituto de Física

Weak and Strong Gravity Effects in Astrophysics and Cosmology

By: **Camilo Santa Vélez**

UNIVERSIDAD
DE ANTIOQUIA
1803

Medellin, Colombia
2021

Weak and Strong Gravity Effects in Astrophysics and Cosmology

Camilo Santa Vélez

Research thesis to opt for the title of:
PhD in Physics

Advisor:
Antonio Enea Romano Ph. D.

Research group:
COSMOGRAV

There is more joy in heaven in a good approximation than in an exact solution.
Julian Schwinger

Abstract

Gravity is fundamental to formulate the standard cosmological model and understand smaller-scale astrophysical processes. This thesis studies different problems involving weak and strong gravitational effects in astrophysics and cosmology.

In the strong gravity regime, we use a neural network to reconstruct the parameters of a binary black hole merger from its gravitational wave signal. Effective one-body numerical relativity simulations are used to generate a template bank of gravitational waves spectrograms. This dataset is then used to train a neural network to estimate the masses of the black holes.

In the weak gravity regime, we study static spherically symmetric (SSS) metrics as generalizations of the de Sitter metric and find their form as perturbations of the FRW Universe using gauge-invariant variables. We then apply these results to compute the turnaround radius (TAR) and the gravitational stability mass (GSM) to constrain scalar-tensor gravity theories with observational data.

In the last part, we investigate the problem of reconstructing the density field from its weak lensing effects on the luminosity distance. First, we simulate many random configurations of cosmic structure, compute their effects on the luminosity distance using perturbation theory, and finally develop a neural network to reconstruct the density and velocity fields from the luminosity distance.

Keywords: Cosmological Perturbation Theory, Turn Around Radius, Gravitational Waves, Luminosity Distance, Artificial Intelligence, Deep Learning.

Contents

1 Introduction

1.1 Gravitational Waves

General relativity has been one of the most important discoveries in the last century. Unifying gravity with special relativity was able to explain and predict many phenomena, for example, Mercury's perihelion precession [1], gravitational lenses or the recently detected gravitational waves [2]. Signals from compact binary objects open a new window into multimessenger astrophysics, thanks to different collaborations' detection of gravitational waves and their electromagnetic counterpart. Their high sensitivity allows measurements of far-away binary systems thanks to the fact that the amplitude of gravitational waves scales linearly with the inverse of the distance instead of its square [3].

According to general relativity, gravitational waves propagate at the speed of light and in the linear perturbative regime are produced by the second-order time derivative of the quadrupole moment. The primary sources of gravitational waves detected at the Laser Interferometer Gravitational Wave Observatory (LIGO), and Virgo collaborations are the mergers of compact binary systems composed of black holes or neutron stars.

Due to the no-hair theorem, the merger of two black holes has no electromagnetic counterpart [4] but binary star mergers can have electromagnetic signals, opening a new window into multimessenger astronomy. These systems are known as standard sirens because the gravitational wave signal provides information of the distance to the objects independent of the cosmic distance ladder, and their electromagnetic counterparts provide information about their speed. Therefore, they can be used to measure the Hubble parameter [5, 4] or to constrain alternative gravity theories with superluminal or subluminal GW speeds [6].

To achieve this goal, the detectors must have a strain sensitivity of the order of $10^{-21}/\sqrt{Hz}$ [7] and the standard data analysis approach consists of using matched filtering to compare the detector signal to a bank of gravitational wave templates to determine the merger parameters. This data-driven approach has several drawbacks compared to kernel models, such as computational complexity and lack of interpolation. Neural networks can be used to denoise the raw signal [8, 9] as a preprocessing step before matched filtering. This data analysis process must be repeated for every signal, which can be very time-consuming and computationally expensive depending on the size of the template bank.

Another approach has been developed [10, 11, 12, 13, 14, 15, 16, 17, 18] in which the time domain detector data is processed by a convolutional neural network to predict the merger masses. Convolutional neural networks were used to capture the temporal and spatial dependence of the data. These deep neural networks methods capture the local structure by using multiple matrix convolutions with kernels that specialize in identifying complex features in the data.

Even though deep learning methods also require a template bank for training, the resulting model can perform inference much faster and even work on data that it was not trained on. To achieve this, we follow a procedure similar to the one in [10], predicting the mass of the original black holes based on the spectrogram of the gravitational wave signals. We achieve state-of-the-art results on a separate held-out dataset even for signals with a low signal-to-noise ratio [19].

1.2 Turn around radius

The only evidence of dark matter has been provided by gravitational observations such as flat rotational curves and the matter density from the current cosmological model. However, there has been no conclusive evidence of direct dark matter particle detection (considering that [20] has ruled out DAMA/LIBRA). Even if general relativity is consistent with the observations, there is a discrepancy between the total matter content in the universe and visible matter. Instead of adding additional particles, an alternative approach to account for this discrepancy is to modify general relativity or even to consider it an effective theory of another higher energy scale or unified theory [21, 22, 23]. If this is the case, this modified gravity theory must comply with the tests that general relativity has passed in both the weak and strong gravity regimes.

On a cosmological scale, the Turn Around Radius (TAR), or equivalent Gravitational Stability Mass (GSM), establishes a limit of the maximum size or mass for gravitationally bound structures. This limit occurs because there are two opposing effects in an expanding universe: on the one hand, there is an attractive force due to gravitational collapse, and on the other, there is a repulsive force due to dark energy. This limit depends on the cosmological constant and can be used to determine its value [24].

The Turn Around Radius was computed for different modifications of general relativity such as Brans-Dicke theory [25] and a perturbed FLRW universe [26]. This thesis aims to study static spherically symmetric (SSS) metrics as perturbations of the de Sitter Universe.

This perturbative form allows to compute the TAR and GSM for modified gravity theories (MGT) and test them by comparing them to observations. Using this approach, we have constrained the parameters of different modified gravity theories such as $f(R)$ or Quintessence [27].

1.3 Luminosity Distance

Supernovae are among the brightest astrophysical objects which can be observed in our universe, and this has allowed us to test the standard cosmological model at a redshift where no other observation is available, providing the first evidence of dark energy. Both gravitational lensing and gravitational redshift can affect the propagation of photons through an inhomogeneous medium, and consequently, the luminosity distance, so that besides allowing to determine the background cosmological model parameters, they can also be used to reconstruct the density and peculiar velocity fields [28], providing a unique tool to probe large scale structure at scales where other astrophysical objects are too dim to be observed. The inversion problem, consisting in reconstructing large scale structure from its weak field effects on the luminosity distance, has been solved only under certain simplifying symmetry assumptions [29, 30], and the solution is obtained by solving complicated systems of differential equations. This approach requires smooth functions as inputs, but observational data is rarely in a smooth form. To overcome these limitations in this thesis, we develop a novel numerical approach to the inverse problem solution based on artificial intelligence, specifically on the use of deep learning.

The inversion problem is a very general subject of research studied in many different fields such as medical physics [31] or seismic inversion [32], and recently deep learning has shown to be a promising approach for its solution [33, 34, 35, 36], taking advantage of the computational advances made possible by the availability of graphical processing units (GPU). We adopt a method based on creating a database of simulated luminosity distance data obtained by solving the direct problem for a large set of random density configurations.

The simulated data is then used to train a convolutional neural network (CNN) to solve the inversion problem, i.e., reconstructing the density and velocity fields from the luminosity distance. Since the physics of the direct problem is well-understood [37], there is virtually no limit in the amount of simulated data that can be created to train the CNN. Allowing good results in the learning process since supervised machine learning and, more specifically, deep learning performs well if there is a significant and high-quality labeled dataset. The model's performance is then tested with a separate held-out set which shows the reconstructed profiles match closely with the expected ones [38].

2 Artificial Intelligence

Artificial intelligence comprises any system that acts in any way that simulates human intelligence. However, this field is split into two different approaches. The first one, expert programming, relies on an expert to code the different rules that mimic human behavior. The second approach, machine learning, relies on historical data, which can train different algorithms to reproduce the expected behavior. In broad terms, most machine learning models have a set of trainable parameters w_j that produce a prediction $\hat{y}$ when they are fed with some features x_i:

$$\hat{y} = f(x_i, w_j). \tag{2-1}$$

This is repeated for each instance n in our data set:

$$\hat{y}_n = f(x_{ni}, w_j). \tag{2-2}$$

In the case of supervised machine learning, these predictions can be compared to the correct values y_n using a loss function $\mathcal{L}$ and the parameters of the model can be optimized to minimize the cost function:

$$w_j^* = \underset{w_j}{\operatorname{argmin}}\, \mathcal{L}(y_n, \hat{y}_n). \tag{2-3}$$

The most used minimization method is the iterative process of gradient descent, where the gradient of the cost function is computed, and repeated steps are taken in the opposite direction, which corresponds to the direction of steepest descent [39]. These steps are modulated by the learning rate α, and each iteration corresponds to:

$$w_j \rightarrow w_j - \alpha \frac{\partial \mathcal{L}}{\partial w_j}. \tag{2-4}$$

This training process is repeated until the model achieves a desired accuracy measured on a separate validation data set not used during training. This work will focus exclusively on neural networks such as Multilayer Perceptrons (MLP) and Convolutional Neural Networks (CNNs).

2.1 Deep Learning

Deep learning uses deep artificial neural networks as the machine learning model. Deep neural networks are made up of many subsequent layers of parameters trained by gradient descent. Thanks to the internet and social networks, deep learning has recently received much attention thanks to the latest advancements in software, GPU hardware, and data availability. For a comprehensive review, [40],[41] and [42] are recommended.

Before talking about neural networks, it's convenient to define a single artificial neuron [43] which produces prediction or output by applying a nonlinear function ϕ on a weighted sum of m input variables or features:

$$\hat{y}_n = \phi\left(\sum_i^m w_i x_{ni} + b\right), \tag{2-5}$$

where b is known as the bias term. The most commonly used nonlinear functions are the sigmoid or logistic function and the rectified linear unit (ReLU) function:

$$Sigmoid(z) = \frac{1}{1+e^{-z}} \tag{2-6}$$

$$ReLU(z) = max(0, z) \tag{2-7}$$

This can be extended to an arbitrary amount of layers l and of neurons j per layer if we consider the input features as the neurons in the first layer ($x_{ni} \rightarrow x_{ni}^{[0]}$) and the prediction $\hat{y}_n$ of the neural network as the output of the last layer L

$$x_{nj}^{[l]} = \phi^{[l]}\left(\sum_i^{m_l} w_{ji}^{[l]} x_{ni}^{[l-1]} + b_j^{[l]}\right), \tag{2-8}$$

$$\hat{y}_n = x_n^{[L]}, \tag{2-9}$$

where we have introduced m_l as the number of neurons in layer l and assumed the last layer L has only one feature (i.e. $m_L = 1$). It's important to note that each neuron j in layer l has an independent set of weights $w_{ji}^{[l]}$ and bias $b_j^{[l]}$ term which are initialized randomly but trained using gradient descent (2-4). However, the gradient must be computed for every layer in the network using the chain rule which is commonly known as backpropagation [44].

A new type of neural network architecture has been created to deal with high dimensional data such as images using matrix cross correlation between images and filters [45][46]. These networks train convolutional kernels or filters that transform images or extract features through a sliding inner product. Therefore, some neurons will have the same weights given by the convolutional kernels. Compared to the network described by (2-8) Convolutional Neural Networks (CNNs) have a higher degree of sparsity which, coupled to pooling operations that reduce the image size, allow training on current hardware even with high-resolution images.

3 General Relativity

This chapter is by no means an exhaustive recount of general relativity, for a full summary [47], [48] and [49] are recommended. Only the main results needed for this work are presented, and previous knowledge of the theory is assumed. Every computation is taken under the metric formalism, where the metric connection and curvature tensors are determined completely by the metric. Additionally, Einstein's notation of summation under repeated indices and natural units is used all along, where $c = G = 1$.

The metric $(g_{\mu\nu})$ determines the space-time interval between two events in a coordinate system x^μ:

$$ds^2 = g_{\mu\nu} dx^\mu dx^\nu, \tag{3-1}$$

where dx^μ represents the coordinate differentials. Additionally, the inverse of the metric can be defined such that $g^{\mu\sigma} g_{\sigma\nu} = \delta^\mu_\nu$. This interval can take positive, negative, or even null values depending on the speed needed to go from one event to another. If this speed is less than the speed of light, the interval is positive and is said to be time-like; this is the type of trajectories described by massive particles. If, on the other hand, the required speed is the speed of light, the space-time interval is zero, and it is known as lightlike. Lastly, if the required speed is greater than the speed of light, the interval is negative, called space-like. These signs depend on the metric signature; in this work, it is considered $(+,-,-,-)$. For a theory to be invariant under coordinate changes, it must be implemented in tensor notation. The components of an arbitrary tensor transform in the following way under the coordinate transformation $(x^\mu \to x'^\mu)$

$$T'^{\nu\cdots}{}_{\sigma\cdots} = \left(\frac{\partial x'^\nu}{\partial x^\alpha}\cdots\right)\left(\frac{\partial x_\sigma}{\partial x'_\beta}\cdots\right) T^{\alpha\cdots}{}_{\beta\cdots}, \tag{3-2}$$

it is important to take into account that scalars remain invariant. On the other hand, the tensor derivatives don't necessarily obey these rules. To have derivatives that transform as a tensor, the metric connection coefficients are needed. Under the metric formalism, the Christoffel symbols of the second kind can be used to build an affine metric connection:

$$\Gamma^\mu_{\nu\rho} = \frac{1}{2} g^{\mu\sigma} \left(\partial_\nu g_{\sigma\rho} + \partial_\rho g_{\sigma\nu} - \partial_\sigma g_{\nu\rho}\right), \tag{3-3}$$

where $\partial_\mu = \partial/\partial x^\mu$. Due to the symmetry of the metric tensor, this connection is torsionless because it is symmetric by definition:

$$\Gamma^\alpha_{\mu\nu} = \Gamma^\alpha_{\nu\mu}, \tag{3-4}$$

which can ease the computation of non-null components. These coefficients establish how tensor quantities change under parallel transport and allow a derivative in curved space, called covariant derivative which obeys the transformation law (3-2). The covariant derivative of an arbitrary tensor is obtained by contracting the indices of the connection with each index in the tensor respectively

$$\nabla_\mu T^{\nu\cdots}{}_{\sigma\cdots} = \partial_\mu T^{\nu\cdots}{}_{\sigma\cdots} + \Gamma^{\nu}_{\rho\mu} T^{\rho\cdots}{}_{\sigma\cdots} + \cdots - \Gamma^{\rho}_{\sigma\mu} T^{\nu\cdots}{}_{\rho\cdots} - \cdots \tag{3-5}$$

This connection, in particular, is a metric connection because the covariant derivative of the metric tensor is zero:

$$\nabla_\rho g_{\mu\nu} = 0. \tag{3-6}$$

The connection also defines the Riemann curvature tensor, which describes the change in a vector after parallel transport through 2 different paths:

$$R^{\mu}{}_{\nu\rho\sigma} = \partial_\rho \Gamma^{\mu}_{\nu\sigma} - \partial_\sigma \Gamma^{\mu}_{\nu\rho} + \Gamma^{\mu}_{\rho\lambda}\Gamma^{\lambda}_{\nu\sigma} - \Gamma^{\mu}_{\sigma\lambda}\Gamma^{\lambda}_{\nu\rho}. \tag{3-7}$$

Due to the shape of the tensor, only 20 of the 256 components are independent due to the following symmetries:

$$R_{\mu\nu\rho\sigma} = -R_{\nu\mu\rho\sigma} = -R_{\mu\nu\sigma\rho}, \tag{3-8}$$

$$R_{\mu\nu\rho\sigma} = R_{\rho\sigma\mu\nu}, \tag{3-9}$$

$$R_{\mu\nu\rho\sigma} + R_{\mu\rho\sigma\nu} + R_{\mu\sigma\nu\rho} = 0, \tag{3-10}$$

where this last one is known as the first Bianchi identity.

From the Riemann tensor, it is possible to build the Ricci tensor, which describes the volumetric change of a geodesic sphere in contrast to flat space-time. With respect to the Riemann tensor, the Ricci tensor is just an index contraction:

$$R_{\mu\nu} = R^{\sigma}{}_{\mu\sigma\nu}, \tag{3-11}$$

where, due to the Riemann tensor's symmetries, the Ricci tensor is symmetric in its two indices $R_{\mu\nu} = R_{\nu\mu}$. The Ricci scalar is the simplest scalar that can be computed with only one Riemann tensor and, being a scalar; it is invariant under coordinate transformations

$$\mathcal{R} = R^{\mu}{}_{\mu} = R^{\mu\nu}{}_{\mu\nu}. \tag{3-12}$$

On the other hand, the Kretschmann scalar is a quadratic quantity because it is defined as a contraction of two Riemann tensors, and it is an important scalar when analyzing metric singularities:

$$K = R^{\mu\nu\sigma\rho} R_{\mu\nu\sigma\rho}. \tag{3-13}$$

Finally, both the Riemann and Ricci tensors can be used to compute the Einstein tensor

$$G_{\mu\nu} = R_{\mu\nu} - \frac{1}{2} g_{\mu\nu} \mathcal{R}, \tag{3-14}$$

that will be useful when writing the field equations in a compact form, presented in the next section.

3.1 Einstein-Hilbert Action

In order to obtain equations invariant under general coordinate transformations, the action of general relativity must be a scalar. One possibility is to use the Ricci scalar $\mathcal{R}$, from which the Einstein-Hilbert action with lagrangian matter density $\mathcal{L}_M$ can be written as

$$\mathcal{S} = \int d^4x\sqrt{-g}\left(\frac{1}{16\pi}\mathcal{R} + \mathcal{L}_M\right), \tag{3-15}$$

where $g_{\mu\nu}$ is the metric and g is its determinant. The lagrangian density $\mathcal{L}_M$ describes the dynamic of matter inside a given space-time. The equations of motion can be derived using variational principles minimizing the action, taking into account that the variation of the action with respect to the metric must be zero $\delta S = 0$:

$$\begin{aligned} \delta\mathcal{S} &= \int d^4x\left[\frac{1}{16\pi}\frac{\delta\left(\sqrt{-g}\mathcal{R}\right)}{\delta g^{\mu\nu}} + \frac{\delta\left(\sqrt{-g}\mathcal{L}_M\right)}{\delta g^{\mu\nu}}\right]\delta g^{\mu\nu} \\ &= \int d^4x\left[\frac{1}{16\pi}\frac{1}{\sqrt{-g}}\frac{\delta\left(\sqrt{-g}\mathcal{R}\right)}{\delta g^{\mu\nu}} + \frac{1}{\sqrt{-g}}\frac{\delta\left(\sqrt{-g}\mathcal{L}_M\right)}{\delta g^{\mu\nu}}\right]\delta g^{\mu\nu}\sqrt{-g} \\ &= 0, \end{aligned} \tag{3-16}$$

where $\delta g^{\mu\nu}$ is the variation of the metric's inverse. This variation must cancel itself under any arbitrary variation $\delta g^{\mu\nu}$, which implies that the quantity inside the square brackets must be zero:

$$\begin{aligned} \frac{1}{16\pi}\frac{1}{\sqrt{-g}}\frac{\delta\left(\sqrt{-g}\mathcal{R}\right)}{\delta g^{\mu\nu}} &= -\frac{1}{\sqrt{-g}}\frac{\delta\left(\sqrt{-g}\mathcal{L}_M\right)}{\delta g^{\mu\nu}}, \\ \frac{1}{16\pi}\left[\frac{\delta\mathcal{R}}{\delta g^{\mu\nu}} + \frac{\mathcal{R}}{\sqrt{-g}}\frac{\delta\left(\sqrt{-g}\right)}{\delta g^{\mu\nu}}\right] &= -\frac{\delta\mathcal{L}_M}{\delta g^{\mu\nu}} - \frac{\mathcal{L}_M}{\sqrt{-g}}\frac{\delta\left(\sqrt{-g}\right)}{\delta g^{\mu\nu}}, \\ \frac{1}{8\pi}\left[\frac{\delta\mathcal{R}}{\delta g^{\mu\nu}} + \frac{\mathcal{R}}{2g}\frac{\delta g}{\delta g^{\mu\nu}}\right] &= -2\frac{\delta\mathcal{L}_M}{\delta g^{\mu\nu}} - \frac{\mathcal{L}_M}{g}\frac{\delta g}{\delta g^{\mu\nu}}, \end{aligned} \tag{3-17}$$

where the right-hand side of the equation defines the energy-momentum tensor $T_{\mu\nu}$.

To get the variations to the contravariant components of the metric $g^{\mu\nu}$, the variations with respect to the covariant components $g_{\mu\nu}$ must be computed first. With this in mind, the Jacobi formula allows to derive the variation of the determinant of a matrix with respect to one of its components:

$$\delta g = \delta det(g_{\mu\nu}) = Tr\left(g\, g^{\mu\nu}\delta g_{\nu\rho}\right) = g\, g^{\mu\nu}\delta g_{\nu\mu}. \tag{3-18}$$

This same procedure must be taken with the inverse of the metric considering that the determinant of the inverse is related to the determinant of the metric by $det(g^{\mu\nu}) = det(g_{\mu\nu})^{-1}$:

$$\begin{aligned} \delta\left(\frac{1}{g}\right) &= \delta det(g^{\mu\nu}) = Tr\left[\frac{g_{\mu\nu}}{g}\delta g^{\nu\rho}\right] = \frac{g^{\mu\nu}}{g}\delta g_{\nu\mu}, \\ \delta\left(\frac{1}{g}\right) &= -\frac{\delta g}{g^2}, \\ \delta g &= -g\, g_{\mu\nu}\delta g^{\mu\nu}. \end{aligned} \tag{3-19}$$

With the previous result, the variation of the determinant with respect to the metric $g^{\mu\nu}$ can now be computed. To obtain the variation of the Ricci scalar with respect to the metric, the variation of the Riemann tensor must be computed first:

$$\begin{aligned}\delta R^{\rho}{}_{\sigma\mu\nu} &= \partial_{\mu}\delta\Gamma^{\rho}_{\nu\sigma} - \partial_{\nu}\delta\Gamma^{\rho}_{\mu\sigma} + \delta\Gamma^{\rho}_{\mu\lambda}\Gamma^{\lambda}_{\nu\sigma} + \Gamma^{\rho}_{\mu\lambda}\delta\Gamma^{\lambda}_{\nu\sigma} - \delta\Gamma^{\rho}_{\nu\lambda}\Gamma^{\lambda}_{\mu\sigma} - \Gamma^{\rho}_{\nu\lambda}\delta\Gamma^{\lambda}_{\mu\sigma} \\ &= \nabla_{\mu}(\delta\Gamma^{\rho}_{\nu\sigma}) - \nabla_{\nu}(\delta\Gamma^{\rho}_{\mu\sigma}),\end{aligned} \tag{3-20}$$

where the last step considered that $\delta\Gamma$ is a tensor quantity, even if the individual connection coefficients are not tensor quantities because it's the difference between two connection coefficients. With this previous result at hand, the variation of the Ricci tensor is:

$$\delta R_{\mu\nu} = \delta R^{\rho}{}_{\mu\rho\nu} = \nabla_{\rho}(\delta\Gamma^{\rho}_{\nu\mu}) - \nabla_{\nu}(\delta\Gamma^{\rho}_{\rho\mu}). \tag{3-21}$$

Finally, using the previous results, it is possible to compute the variation of the Ricci scalar considering a metric connection ($\nabla_{\sigma}g^{\mu\nu} = 0$):

$$\delta R = R_{\mu\nu}\delta g^{\mu\nu} + \nabla_{\sigma}\left(g^{\mu\nu}\delta\Gamma^{\sigma}_{\nu\mu} - g^{\mu\sigma}\delta\Gamma^{\rho}_{\rho\mu}\right), \tag{3-22}$$

The last term turns into a total derivative and gives rise to the York-Gibbons-Hawking boundary term [50],[51]. If the variation of the metric tends to zero at infinity, this term can be ignored due to Stokes theorem, and the variation of the Ricci scalar with respect to the variation of the metric is:

$$\frac{\delta\mathcal{R}}{\delta g^{\mu\nu}} = R_{\mu\nu}, \tag{3-23}$$

the Einstein field equations are obtained by substituting this into (3-17):

$$\begin{aligned} R_{\mu\nu} - \frac{1}{2}g_{\mu\nu}\mathcal{R} &= 8\pi T_{\mu\nu}, \\ G_{\mu\nu} &= 8\pi T_{\mu\nu},\end{aligned} \tag{3-24}$$

where the last step involves the definition of the Einstein tensor (3-14). These are second-order equations in the metric and determine which metrics are compatible with different matter fields. Therefore, matter establishes the curvature of space-time. This result can be extended considering a constant Λ in the Einstein-Hilbert action:

$$\mathcal{S} = \int d^4x\sqrt{-g}\left[\frac{1}{16\pi}(\mathcal{R} - 2\Lambda) + \mathcal{L}_M\right], \tag{3-25}$$

which modifies the Einstein field equations accordingly:

$$\begin{aligned} &R_{\mu\nu} - \frac{1}{2}g_{\mu\nu}\mathcal{R} - g_{\mu\nu}\Lambda = 8\pi T_{\mu\nu}, \\ &G_{\mu\nu} - g_{\mu\nu}\Lambda = 8\pi T_{\mu\nu}.\end{aligned} \tag{3-26}$$

Einstein introduced this constant, known as the cosmological constant, to have a static universe. However, due to Georges Lemaitre and Edwin Hubble's observations of an expanding universe, Einstein abandoned the cosmological constant and called it his biggest blunder. Recently, the use of Type IA supernova catalogs has determined that the universe is currently in a stage of accelerated expansion with a positive but close to zero cosmological constant [52, 53].

If the value of the cosmological constant is taken to the right-hand side of the equation, it can be interpreted as the vacuum's energy-momentum tensor:

$$T^{\Lambda}_{\mu\nu} = \frac{\Lambda}{8\pi} g_{\mu\nu}, \tag{3-27}$$

which corresponds to a perfect fluid with negative pressure. The value of Λ obtained from analyzing observational data disagrees with the one predicted by particle physics by several orders of magnitude [54], a circumstance which has been defined as the worst prediction in the history of theoretical physics [55].

In 1971 David Lovelock [56] proved that in four dimensions, the most general divergenceless tensor which can be constructed from the first two derivatives of the metric is

$$E^{\mu\nu} = \alpha\left(R^{\mu\nu} - \frac{1}{2} g^{\mu\nu} R\right) + \lambda g^{\mu\nu} \tag{3-28}$$

where α and λ are arbitrary constants, which is exactly the geometric part of the Einstein's equations eq.(3-26). This implies that in order to modify General Relativity we need violate some of the hypotheses of the Lovelock's theorems by introducing :

- field equations depending on derivatives higher than 2, obtainable from actions involving higher derivatives of the metric
- additional fields
- higher dimensional spaces
- non-divergenceless field equations

As noted by Lovelock [57], it can be shown that Einstein-Hilbert's action is not the most general action that gives rise to Einstein's field equations.

The geodesic equations for a given space-time will be derived in the next section. This shows how space-time affects the trajectory of a test particle.

3.2 Geodesics in General Relativity

Geodesic equations describe a free particle's path in a given space-time. Such trajectories are known as the particles world line. The principle of least action must be used to find the curve the particles describe. The space-time distance travelled by a particle from point p_1 to point p_2 is given by:

$$I = \int_{p_1}^{p_2} ds = \int_{p_1}^{p_2} L du, \tag{3-29}$$

where u is an affine parameter along the geodesic, in the case of massive particles, proper time can be used. The term under the integral is $L = \sqrt{g_{\mu\nu}\partial_u x^\mu \partial_u x^\nu}$. It is also possible to work with the square of this term to avoid square roots:

$$I_2 = \int_{p_1}^{p_2} L^2 du, \tag{3-30}$$

however, this integral no longer represents the physical distances traveled by the particle. The curves that minimize this integral, known as geodesics, can be found thanks to the principle of least action. According to the Euler-Lagrange equations, the geodesic trajectory must follow

$$\frac{\partial L^2}{\partial x^\sigma} - \frac{d}{du}\left(\frac{\partial L^2}{\partial \dot{x}^\sigma}\right) = 0, \tag{3-31}$$

where the dot $(\dot{\ })$ corresponds to a derivative in the affine parameter. Replacing L^2 in the previous equation:

$$\begin{aligned}\frac{\partial L^2}{\partial x^\sigma} - \frac{d}{du}\left(\frac{\partial L^2}{\partial \dot{x}^\sigma}\right) &= \frac{\partial(g_{\mu\nu}\dot{x}^\mu\dot{x}^\nu)}{\partial x^\sigma} - \frac{d}{du}\left(\frac{\partial(g_{\mu\nu}\dot{x}^\mu\dot{x}^\nu)}{\partial \dot{x}^\sigma}\right)\\ &= \partial_\sigma g_{\mu\nu}\dot{x}^\mu\dot{x}^\nu - 2\frac{d}{du}\left(g_{\mu\sigma}\dot{x}^\mu\right)\\ &= \partial_\sigma g_{\mu\nu}\dot{x}^\mu\dot{x}^\nu - 2g_{\mu\sigma}\ddot{x}^\mu - 2\partial_\nu g_{\mu\sigma}\dot{x}^\mu\dot{x}^\nu\\ &= \partial_\sigma g_{\mu\nu}\dot{x}^\mu\dot{x}^\nu - 2g_{\mu\sigma}\ddot{x}^\mu - \partial_\nu g_{\mu\sigma}\dot{x}^\mu\dot{x}^\nu - \partial_\mu g_{\nu\sigma}\dot{x}^\nu\dot{x}^\mu\\ &= -2g_{\mu\sigma}\ddot{x}^\mu - \left(\partial_\nu g_{\mu\sigma} + \partial_\mu g_{\nu\sigma} - \partial_\sigma g_{\mu\nu}\right)\dot{x}^\mu\dot{x}^\nu.\end{aligned} \tag{3-32}$$

The geodesic equations are obtained by rearranging these equations, contracting the σ index, and taking into account the definition of the Christoffel symbols:

$$\begin{aligned}\ddot{x}^\lambda + \frac{1}{2}g^{\lambda\sigma}\left(\partial_\nu g_{\mu\sigma} + \partial_\mu g_{\nu\sigma} - \partial_\sigma g_{\mu\nu}\right)\dot{x}^\mu\dot{x}^\nu &= 0\\ \ddot{x}^\lambda + \Gamma^\lambda{}_{\mu\nu}\frac{dx^\mu}{d\tau}\frac{dx^\nu}{d\tau} &= 0.\end{aligned} \tag{3-33}$$

Besides, it is important to note that the space-time interval is positive (time-like $ds^2 > 0$) for massive particles and zero for massless particles (lightlike $ds^2 = 0$). In the weak-field regime, this expression matches Newton's law of universal gravitation. In that limit, a linear order perturbative metric must be considered such that:

$$ds^2 = (1+2\Psi)dt^2 - (1-2\Phi)\left[dr^2 + r^2 d\Omega^2\right], \tag{3-34}$$

where Φ and Ψ are the gravitational potentials and with low velocities, such that

$$\frac{dx^\mu}{d\tau} \approx (1,0,0,0), \tag{3-35}$$

where the proper time was taken as the affine parameter and is approximately the temporal coordinate in this limit. According to these approximations, the geodesics correspond to

$$\begin{aligned} \ddot{x}^i + \Gamma^i_{00} &= 0, \\ \ddot{x}^i &= -\Gamma^i_{00}, \\ \ddot{\vec{x}} &= \nabla\Psi. \end{aligned} \tag{3-36}$$

In a following chapter, a spherically symmetric metric in general relativity has the gravitational potentials $\Psi = \Phi = -\frac{m}{r}$ and Newton's gravitational law of universal gravitation is recovered:

$$\ddot{\vec{x}} = -\frac{m\hat{x}}{r^2}. \tag{3-37}$$

It is also possible to state these equations in terms of the time coordinate, considering that $\frac{d}{d\tau} = \frac{dt}{d\tau}\frac{d}{dt}$, and the goedesic becomes:

$$\frac{d^2t}{d\tau^2} = -\Gamma^0_{\mu\nu}\frac{dx^\mu}{d\tau}\frac{dx^\nu}{d\tau}. \tag{3-38}$$

Finally, the geodesic equations in the time coordinate can be computed by replacing the previous equation in (3-33):

$$\begin{aligned} \frac{dt}{d\tau}\frac{d}{dt}\left(\frac{dt}{d\tau}\frac{dx^\lambda}{dt}\right) + \Gamma^\lambda_{\mu\nu}\left(\frac{dt}{d\tau}\right)^2\frac{dx^\mu}{dt}\frac{dx^\nu}{dt} &= 0, \\ \frac{d^2t}{d\tau^2}\frac{dx^\lambda}{dt} + \left(\frac{dt}{d\tau}\right)^2\frac{d^2x^\lambda}{dt^2} + \Gamma^\lambda_{\mu\nu}\left(\frac{dt}{d\tau}\right)^2\frac{dx^\mu}{dt}\frac{dx^\nu}{dt} &= 0, \\ -\Gamma^0_{\mu\nu}\frac{dx^\mu}{d\tau}\frac{dx^\nu}{d\tau}\frac{dx^\lambda}{dt} + \left(\frac{dt}{d\tau}\right)^2\frac{d^2x^\lambda}{dt^2} + \Gamma^\lambda_{\mu\nu}\left(\frac{dt}{d\tau}\right)^2\frac{dx^\mu}{dt}\frac{dx^\nu}{dt} &= 0, \\ -\Gamma^0_{\mu\nu}\left(\frac{dt}{d\tau}\right)^2\frac{dx^\mu}{dt}\frac{dx^\nu}{dt}\frac{dx^\lambda}{dt} + \left(\frac{dt}{d\tau}\right)^2\frac{d^2x^\lambda}{dt^2} + \Gamma^\lambda_{\mu\nu}\left(\frac{dt}{d\tau}\right)^2\frac{dx^\mu}{dt}\frac{dx^\nu}{dt} &= 0, \\ \frac{d^2x^\lambda}{dt^2} + \left(\Gamma^\lambda_{\mu\nu} - \Gamma^0_{\mu\nu}\frac{dx^\lambda}{dt}\right)\frac{dx^\mu}{dt}\frac{dx^\nu}{dt} &= 0. \end{aligned} \tag{3-39}$$

The geodesics can now be computed in coordinate time, without the need of introducing an affine parameter. This eases the comparison with the Newtonian limit directly in the low-speed regime $\frac{dx^i}{dt} \approx 0$:

$$\begin{aligned} \frac{d^2x^\lambda}{dt^2} + \left(\Gamma^\lambda_{\mu\nu} - \Gamma^0_{\mu\nu}\frac{dx^\lambda}{dt}\right)\frac{dx^\mu}{dt}\frac{dx^\nu}{dt} &= 0, \\ \frac{d^2x^i}{dt^2} &= -\Gamma^i_{00}, \\ \frac{d^2x^i}{dt^2} &= -\frac{m}{r^3}x^i, \end{aligned} \tag{3-40}$$

reproducing the Newtonian limit completely consistent with the previous result, which used the affine parameter.

3.3 Friedmann Equations

The Friedmann-Lemaitre-Robertson-Walker (FLRW) metric describes a homogenous and isotropic universe. In this case, the spatial part of the metric can depend only on the time coordinate through the scale factor $a(t)$, which describes the size of the universe. In spherical coordinates, the FLRW metric is:

$$ds^2 = dt^2 - a(t)^2 \left[\frac{dr^2}{1 - kr^2} + r^2 \left(d\theta^2 + \sin^2 \theta d\phi^2 \right) \right], \tag{3-41}$$

where the curvature parameter k can be $+1, 0, -1$ if the universe is closed (positive curvature), flat (zero curvature) or open (negative curvature) respectively. The first components of the Einstein tensor (3-14) for this metric are given by:

$$\begin{aligned} G_{00} &= \frac{3(k + \dot{a}^2)}{a^2}, \\ G_{11} &= \frac{k + \dot{a}^2 + 2a\ddot{a}}{kr^2 - 1}, \end{aligned} \tag{3-42}$$

and due to the isotropy and homogeneity of the universe, the energy-momentum tensor $T_{\mu\nu}$ corresponds to a perfect fluid with density ρ and isotropic pressure:

$$T^{\mu}_{\ \nu} = (\rho + p) u^{\mu} u_{\nu} - p \delta^{\mu}_{\nu} \tag{3-43}$$

where u^{μ} is it's four-velocity. In comoving coordinates the four-velocity is $u^{\mu} = (1, 0, 0, 0)$ and the energy-momentum tensor can be written as

$$T^{\mu}_{\ \nu} = \begin{pmatrix} \rho & 0 & 0 & 0 \\ 0 & \mathrm{p} & 0 & 0 \\ 0 & 0 & \mathrm{p} & 0 \\ 0 & 0 & 0 & \mathrm{p} \end{pmatrix}. \tag{3-44}$$

From here, Einstein's field equations are:

$$\begin{aligned} \frac{3(k + \dot{a}^2)}{a^2} &= 8\pi\rho, \\ \frac{k + \dot{a}^2 + 2a\ddot{a}}{a^2} &= 8\pi p. \end{aligned} \tag{3-45}$$

Differenciating the first equation with respect to time and adding the second equation multiplied by $-3\dot{a}/a$

$$\begin{aligned} 8\pi\dot{\rho} + 24\pi p \frac{\dot{a}}{a} &= \frac{6\dot{a}\ddot{a}a - 6\dot{a}(k + \dot{a}^2)}{a^3} - 3\frac{\dot{a}}{a} \frac{k + \dot{a}^2 + 2a\ddot{a}}{a^2}, \\ &= -3\frac{\dot{a}}{a} \frac{3k + 3\dot{a}^2}{a^2}, \\ &= -24\pi\rho\frac{\dot{a}}{a}, \end{aligned} \tag{3-46}$$

which can be rewritten as

$$\frac{d}{dt}(\rho a^3) + p\frac{d}{dt}(a^3) = 0, \tag{3-47}$$

$$\frac{d\rho}{dt} + 3\frac{\dot{a}}{a}(\rho + p) = 0. \tag{3-48}$$

This can be interpreted as the energy conservation equation taking into account that the volume $V \propto a^3$ and the energy $E = \rho V$. Given the equation of state $p = w\rho$, the continuity equation becomes

$$\frac{dln\rho}{dlna} = -3(1 + w), \tag{3-49}$$

where $w = 1/3, 0, -1$ for a radiation, matter or cosmological constant dominated universe respectively. This equation can be solved to yield

$$\rho a^{3(1+w)} = constant. \tag{3-50}$$

Friedmann's equations can be derived from Einstein's field equations (3-45)

$$H^2 = \left(\frac{\dot{a}}{a}\right)^2 = \frac{8\pi}{3}\rho - \frac{k}{a^2}, \tag{3-51}$$

$$\frac{\ddot{a}}{a} = -\frac{4\pi}{3}(\rho + 3p), \tag{3-52}$$

where the Hubble parameter can be identified as $H = \dot{a}/a$. Under the assumption that different fluids have the same four-velocity, the total density and pressure are the sum of the individual species (denoted by the subindex i)

$$\rho = \sum_i \rho_i \tag{3-53}$$

$$p = \sum_i p_i \tag{3-54}$$

The first Friedmann's equation (3-51) can be rewritten in terms the critical density $\rho_c = \frac{3H_0^2}{8\pi}$ as

$$H^2 = \frac{8\pi}{3H_0^2}H_0^2\rho - \frac{k}{a^2} = H_0^2\frac{\rho}{\rho_c} - \frac{k}{a^2} = H_0^2\sum_i\frac{\rho_i}{\rho_c} - \frac{k}{a^2}, \tag{3-55}$$

where the subindex 0 refers to a quantity measured at present time. Without loss of generality, the present time scale factor can be normalized as $a(t_0) = 1$ and after defining the density parameters $\Omega_i = \rho_{i,0}/\rho_c$ we get:

$$\begin{aligned} \left(\frac{H}{H_0}\right)^2 &= \sum_i \Omega_i a^{-3(1+\omega_i)} + \Omega_k a^{-2}, \\ &= \Omega_r a^{-4} + \Omega_m a^{-3} + \Omega_\Lambda + \Omega_k a^{-2}, \end{aligned} \tag{3-56}$$

with $\Omega_k = -k/a_0^2H_0^2$. Evaluating the above equation at present time $t = t_0$ gives the important relation

$$\sum_i \Omega_i = 1. \tag{3-57}$$

3.3.1 Flat Universe Solutions

In a flat universe the scale factor can be obtained for a single fluid, with equation of state $p = \omega\rho$, by substituting equation (3-50) in (3-51)

$$a(t) \propto \begin{cases} t^{2/3(1+w)} & \text{if } w \neq -1, \\ e^{Ht} & \text{if } w = -1. \end{cases} \tag{3-58}$$

This implies that for a matter dominated universe ($w = 0$)

$$a(t) \propto t^{2/3}, \tag{3-59}$$

for a radiation dominated universe ($w = 1/3$)

$$a(t) \propto t^{1/2}, \tag{3-60}$$

and a universe dominated by cosmological constant ($\omega = -1$)

$$a(t) \propto e^{Ht}. \tag{3-61}$$

According to cosmic microwave background and large scale structure observations, the universe is approximately flat, and the matter and cosmological constant density parameters correspond roughly to $\Omega_m = 0.27$ and $\Omega_\Lambda = 0.72$, as seen in figure **3-1** [58].

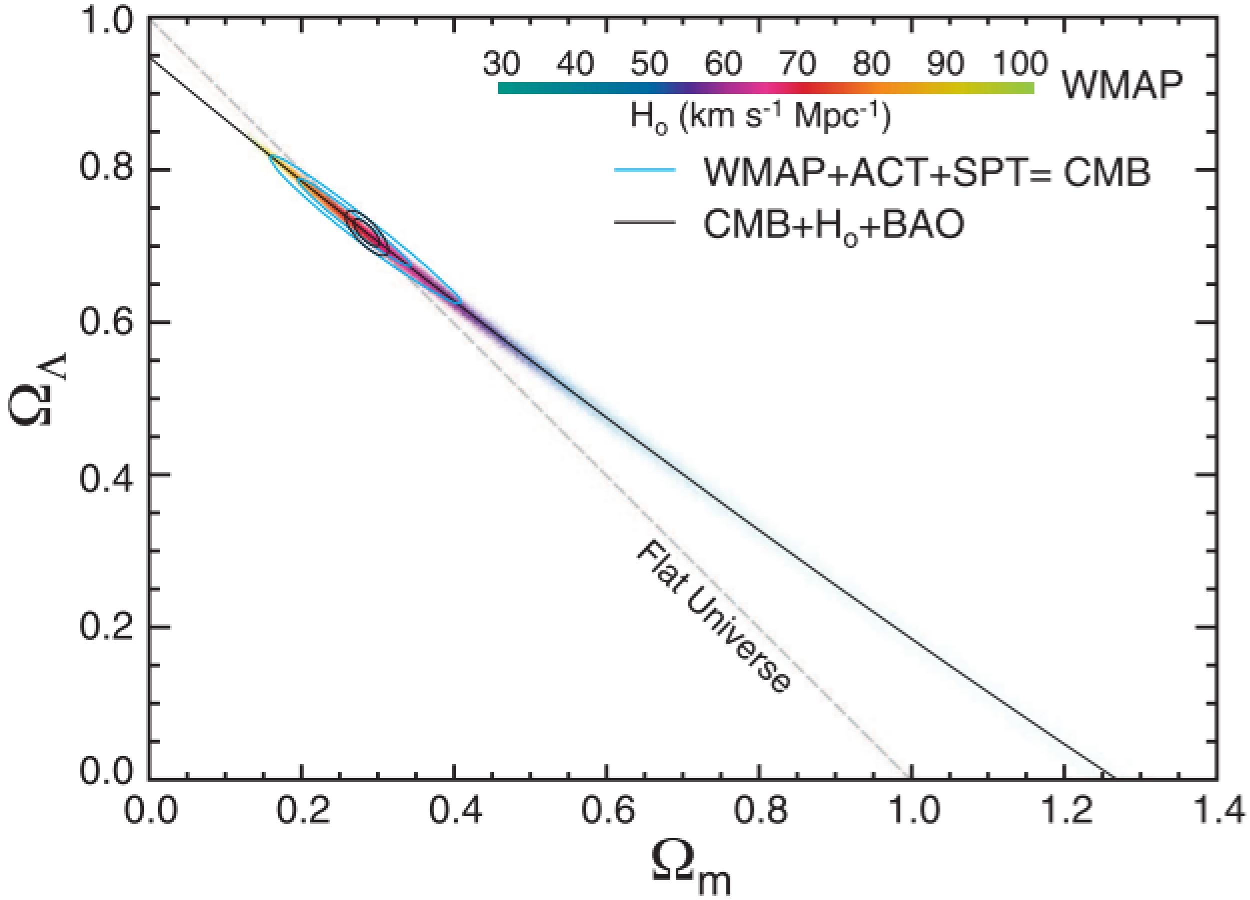

Figure 3-1: WMAP 9 year results constraining curvature and density parameters.

4 Cosmological Perturbation Theory

Newtonian gravity is a good approximation at local scales and low speeds, but it does not successfully explain several observational measurements, such as Mercury's perihelion's precession. On the other hand, General Relativity explains these phenomena, and in the weak field regime, it should match Newtonian Gravity. With cosmological perturbation theory, results from general relativity can be analyzed in the weak field limit and compared directly with Newtonian gravity results. For a full review of cosmological perturbation theory, [59], [60] and [61] are recommended. This work only considers vacuum solutions; therefore, only the metric perturbations contribute, not the perturbations coming from the energy-momentum tensor:

$$g_{\mu\nu} = \tilde{g}_{\mu\nu} + \delta g_{\mu\nu}, \tag{4-1}$$

where the background solution $\tilde{g}$ is the flat FLRW metric (3-41) which describes an homeogenous universe

$$ds^2 = dt^2 - a(t)^2(dx^2 + dy^2 + dz^2). \tag{4-2}$$

The de Sitter metric is equivalent to a flat FLRW metric with an exponential scale factor and can also be used as a background solution. The spatial coordinates in (4-2) are comoving and are related to the physical coordinates by:

$$\begin{aligned} x^i_{(physical)} &= a(t)x^i_{(comoving)}, \\ R &= a(t)r, \end{aligned} \tag{4-3}$$

where the physical radius R has been defined in terms of the comoving radius r. Depending on the sign of $\dot{a}$, this metric describes an expanding, static, or contracting universe. To describe the current accelerated expansion rate of the universe, $a > 0$ is assumed. In this case, the comoving distances can be thought of as a grid of points that expands with the universe; therefore, the comoving distance between two points in the grid remains constant while the physical distance increases. It is convenient to redefine the temporal coordinate according to

$$d\tau = \frac{dt}{a(t)}, \tag{4-4}$$

which results in the metric

$$ds^2 = a(\tau)^2 \left[d\tau^2 - dx^2 - dy^2 - dz^2\right], \tag{4-5}$$

where the new time coordinate is known as the conformal time and should not be confused with a particle's proper time from previous chapters. It receives this name because the resulting metric is conformally equivalent to Minkowski's metric, with conformal factor $a(\tau)$. Due to symmetry, spherical coordinates are preferred. The flat FLRW metric in spherical coordinates and conformal time takes the following form:

$$ds^2 = a(\tau)^2 \left[d\tau^2 - dr^2 - r^2 d\Omega^2\right]. \tag{4-6}$$

where $d\Omega^2 = d\theta^2 + \sin^2\theta d\phi^2$ is the metric of a sphere.

4.1 Scalar-Vector-Tensor Decomposition

The cosmological perturbation metric can be written in conformal time as:

$$ds^2 = a^2(\tau)\left[(1+2A)d\tau^2 - 2B_i d\tau dx^i - (\delta_{ij} + h_{ij})dx^i dx^j\right], \tag{4-7}$$

where, in general, A, B_i, h_{ij} can depend on both space and time. In this case, the ten independent coordinates of the symmetric tensor δg can be decomposed into a scalar A, a spatial vector B_i and a spatial symmetric tensor h_{ij}. Under this decomposition, the original 10 degrees of freedom are decomposed into $1+3+6$ degrees of freedom, respectively. Spatial indices can be lowered and raised with a Kronecker delta because only linear perturbation equations are considered

$$h^i{}_j = \delta^{ik} h_{kj}. \tag{4-8}$$

The advantage of cosmological perturbation theory is that it can decompose perturbations into Scalars, Vectors, and Tensors (SVT). Einstein field equations do not mix scalar, vector, or tensor perturbations at the linear level, and each one can be treated separately. According to the Helmholtz decomposition theorem, a vector can be split into the gradient of a scalar function and a solenoidal (divergence-free) vector

$$B_i = \partial_i B + \hat{B}_i, \tag{4-9}$$

where the hat ($\hat{}$) denotes divergenceless quantities ($\partial^i \hat{B}_i = 0$). The first term is the scalar component of the vector, and the second is its vectorial part, in such a way that the 3 degrees of freedom are split into a scalar (1 degree of freedom) and a solenoidal vector (2 degrees of freedom). Likewise, a tensor can be decomposed into its scalar, vector, and tensor parts:

$$h_{ij} = 2C\delta_{ij} + 2\partial_{\langle i}\partial_{j\rangle}E + 2\partial_{(i}\hat{E}_{j)} + 2\hat{E}_{ij}, \tag{4-10}$$

where the first two terms are its scalar parts, the third is the vector part and the last term is the traceless solenoidal tensor part ($\hat{E}^i{}_i = 0$). The following operators have been defined

$$\partial_{\langle i}\partial_{j\rangle}E = \left(\partial_i\partial_j - \frac{1}{3}\delta_{ij}\nabla^2\right)E, \tag{4-11}$$

$$\partial_{(i}\hat{E}_{j)} = \frac{1}{2}\left(\partial_i\hat{E}_j + \partial_j\hat{E}_i\right), \tag{4-12}$$

this decomposition splits the 6 degrees of freedom of the symmetric matrix h_{ij} into 2 scalar degrees of freedom C, E, 2 vectorial degrees of freedom corresponding to the solenoidal vector $\hat{E}_i$ and 2 tensorial degrees of freedom given by the traceless and divergenceless tensor $\hat{E}_{ij}$. In total, the metric perturbations had 10 degrees of freedom due to a symmetric 4x4 matrix. Now there are 4 scalar degrees of freedom due to the scalar components A, B, C, E, 4 vectorial degrees of freedom from the solenoidal vectors $\hat{E}_i, \hat{B}_i$ and 2 degrees of freedom from the traceless and divergenceless tensor $\hat{E}_{ij}$. Under this decomposition the metric becomes:

$$\begin{aligned} ds^2 = a^2(\tau)\Big[&(1+2A)d\tau^2 - 2\left(\partial_i B + \hat{B}_i\right) d\tau dx^i \\ &- (\delta_{ij} + 2C\delta_{ij} + 2\partial_{\langle i}\partial_{j\rangle}E + 2\partial_{(i}\hat{E}_{j)} + 2\hat{E}_{ij})dx^i dx^j\Big]. \end{aligned} \tag{4-13}$$

However, these perturbations are not unique and are related by coordinate transformations. In the next section, this gauge freedom is addressed, and a convenient gauge fixing method is discussed, which will ease the turnaround radius computation.

4.2 Gauge Transformations

It is possible that, under a coordinate transformation, metric perturbations change or even new perturbations can appear. However, these perturbations are due only to a coordinate system choice and could not even be physical. Therefore, there is a gauge freedom to choose the coordinate system. For example, doing a coordinate change in a flat unperturbed FLRW metric $\tilde{x}^i = x^i + \zeta^i$ the differentials transform as

$$dx^i = d\tilde{x}^i - \partial_\tau \zeta^i d\tau - \partial_k \zeta^i d\tilde{x}^k, \tag{4-14}$$

and the metric in the new coordinates takes the form

$$ds^2 = a(\tau)^2\left[d\tau^2 - 2\partial_\tau \zeta_i d\tilde{x}^i d\tau - (\delta_{ij} + 2\partial_{(i}\zeta_{j)})d\tilde{x}^i d\tilde{x}^j\right], \tag{4-15}$$

where it seems as the perturbations $B_i = \partial_\tau \zeta_i$ and $\hat{E}_i = \zeta_i$ are present. However, as this is equivalent to a flat unperturbed FLRW metric, these perturbations would disappear by reverting to the original coordinates. To get gauge-invariant perturbations, it's necessary to analyze how perturbations transform under both time and space translations known as gauge transformations.

Under a space or time translation like $\tilde{x}^u = x^\mu + \zeta^\mu$ with $\zeta^0 = T$ and $\zeta^i = L^i = \partial^i L + \hat{L}^i$ the metric transforms as a rank 2 tensor:

$$g_{\mu\nu} = \frac{\partial \tilde{x}^\alpha}{\partial x^\mu}\frac{\partial \tilde{x}^\beta}{\partial x^\nu}\tilde{g}_{\alpha\beta}. \tag{4-16}$$

Specifically, the perturbations transform as:

$$\begin{aligned}
A &\to A - T' - \mathcal{H}T, \\
B &\to B + T - L', \\
C &\to C - \mathcal{H}T - \frac{1}{3}\nabla^2 L, \\
E &\to E - L, \\
\hat{B}_i &\to \hat{B}_i - \hat{L}_i', \\
\hat{E}_i &\to \hat{E}_i - \hat{L}_i, \\
\hat{E}_{ij} &\to \hat{E}_{ij},
\end{aligned} \tag{4-17}$$

where $\mathcal{H} = \frac{a'}{a}$ and the prime ($'$) denotes derivative with respect to conformal time. It is interesting to see that the perturbation $\hat{E}_{ij}$ remains invariant under gauge transformations. The metric can be rewritten in terms of gauge-invariant potentials. The following perturbations, known as Bardeen potentials [62], are invariant under gauge transformations:

$$\begin{aligned}
&\Psi = A + \mathcal{H}(B - E') + (B - E')', \\
&\Phi = -C - \mathcal{H}(B - E') + \frac{1}{3}\nabla^2 E, \\
&\hat{\Phi}_i = \hat{E}_i' - \hat{B}_i, \\
&\hat{E}_{ij}.
\end{aligned} \tag{4-18}$$

The Bardeen potentials consist of 2 scalars, one divergenceless spatial vector, and traceless and divergenceless tensor, which implies that the other degrees of freedom are not physical. In other words, from the four scalar degrees of freedom A, B, C, E, only two are physical. The same is true for $\hat{B}_i$ and $\hat{E}_i$. It must be noted that the Bardeen potential Φ has a relative sign with respect to the one originally defined in [62].

Not depending on the choice of the coordinate system, these perturbations can be interpreted as physical perturbations. The invariance under gauge transformations (4-17) of the Bardeen potential Ψ is proved below:

$$\begin{aligned}
&\Psi \to A - T' - \mathcal{H}T + \mathcal{H}[B + T - L' - (E - L)'] + [B + T - L' - (E - L)']' \\
&\Psi \to A - T' - \mathcal{H}T + \mathcal{H}[B + T - E'] + [B + T - E']' \\
&\Psi \to A - T' - \mathcal{H}T + \mathcal{H}T + T' + \mathcal{H}[B + T - E'] + [B - E']' \\
&\Psi \to A + \mathcal{H}(B - E') + (B - E')' \\
&\Psi \to \Psi.
\end{aligned} \tag{4-19}$$

The invariance of the other Bardeen potentials can also be proved, specifically for the other scalar Φ

$$\begin{aligned}
&\Phi \to -(C - \mathcal{H}T - \frac{1}{3}\nabla^2 L) - \mathcal{H}[B + T - L' - (E - L)'] + \frac{1}{3}\nabla^2(E - L)\\
&\Phi \to -C + \mathcal{H}T + \frac{1}{3}\nabla^2 L - \mathcal{H}T - \mathcal{H}[B - E'] + \frac{1}{3}\nabla^2 E - \frac{1}{3}\nabla^2 L\\
&\Phi \to -C - \mathcal{H}[B - E'] + \frac{1}{3}\nabla^2 E\\
&\Phi \to \Phi,
\end{aligned} \tag{4-20}$$

finally, for $\hat{\Phi}_i$ given that $\hat{E}_{ij}$ is trivially invariant

$$\begin{aligned}
&\hat{\Phi}_i \to (\hat{E}_i - \hat{L}_i)' - (\hat{B}_i - \hat{L}_i')\\
&\hat{\Phi}_i \to \hat{E}_i' - \hat{B}_i\\
&\hat{\Phi}_i \to \hat{\Phi}_i.
\end{aligned} \tag{4-21}$$

In order to verify that these are indeed the physical perturbations, the Bardeen potentials are computed for the transformed FLRW metric (4-15) with non-physical perturbations $B_i = \partial_\tau \zeta_i$ and $\hat{E}_i = \zeta_i$

$$\begin{aligned}
\Psi &= A + \mathcal{H}(B - E') + (B - E')' = 0,\\
\Phi &= -C - \mathcal{H}(B - E') + \frac{1}{3}\nabla^2 E = 0,\\
\hat{\Phi}_i &= \hat{E}_i' - \hat{B}_i = \partial_\tau \zeta_i - \partial_\tau \zeta_i = 0,\\
\hat{E}_{ij} &= 0.
\end{aligned} \tag{4-22}$$

All the Bardeen potentials are effectively zero since it was initially an unperturbed metric. Bardeen potentials will be valuable in calculating the turnaround radius because they can be computed in any gauge, as long as the Bardeen potentials are obtained.
Only spherical symmetric metrics are considered in this work, and due to this symmetry consideration, only the scalar perturbations are relevant. The previous expressions can be simplified even more, and it is going to be revisited in the following section.

4.3 Spherical Coordinates

A spherical symmetric metric can be used as a first and simple approximation to cosmological structures. In this case, there is no privileged direction, that's why only the scalar perturbations A, B, C, E contribute to the metric [63]. Therefore, the metric can be simplified much more:

$$ds^2 = a^2(\tau)\left[(1 + 2A)d\tau^2 - 2\partial_i B d\tau dx^i - (\delta_{ij} + 2C\delta_{ij} + 2\partial_{\langle i}\partial_{j\rangle}E)dx^i dx^j\right], \tag{4-23}$$

Given the symmetry, it's more natural to use spherical coordinates where perturbations are only a function of the temporal and radial coordinates. Taking into account that the cartesian derivative in spherical coordinates takes the following form

$$\partial_i = \frac{\partial}{\partial x^i} = \frac{\partial r}{\partial x^i}\frac{\partial}{\partial r} = \frac{x_i}{r}\frac{\partial}{\partial r}, \tag{4-24}$$

the differential operator (4-11) transforms as

$$\begin{aligned}
\partial_{\langle i}\partial_{j\rangle}E\ dx^i dx^j &= \left[\partial_i\left(\frac{x_j}{r}\partial_r\right) - \frac{1}{3}\delta_{ij}\frac{1}{r^2}\partial_r\left(r^2\partial_r\right)\right]E\ dx^i dx^j \\
&= \left[\frac{\delta_{ij}}{r}\partial_r + \frac{x_i x_j}{r^2}\partial_r\partial_r - \frac{x_i x_j}{r^3}\partial_r - \frac{\delta_{ij}}{3}\partial_r\partial_r - \frac{2\delta_{ij}}{3r}\partial_r\right]E\ dx^i dx^j \\
&= \left[\frac{1}{r^2}\partial_r\partial_r - \frac{1}{r^3}\partial_r\right]E x_i x_j dx^i dx^j + \frac{1}{3}\left[\frac{1}{r}\partial_r - \partial_r\partial_r\right]E\delta_{ij}dx^i dx^j \qquad (4\text{-}25) \\
&= \left[\partial_r\partial_r - \frac{1}{r}\partial_r\right]E dr^2 - \frac{1}{3}\left[\partial_r\partial_r - \frac{1}{r}\partial_r\right]E\left(dr^2 + r^2 d\Omega^2\right) \\
&= \frac{2}{3}\left[\partial_r\partial_r - \frac{1}{r}\partial_r\right]E dr^2 - \frac{1}{3}\left[\partial_r\partial_r - \frac{1}{r}\partial_r\right]E r^2 d\Omega^2,
\end{aligned}$$

where both $\delta_{ij}dx^i dx^j = dr^2 + r^2 d\Omega^2$ and $x_i x_j dx^i dx^j = r^2 dr^2$ were considered. This coordinate choice corresponds to the following metric:

$$ds^2 = a^2\left[(1+2A)d\tau^2 - 2\partial_r B d\tau dr - \left(1 - 2C + \frac{2}{3}\mathcal{E}\right)dr^2 - \left(1 - 2C - \frac{1}{3}\mathcal{E}\right)r^2 d\Omega^2\right], \tag{4-26}$$

where the scalar perturbation $\mathcal{E}$ has been defined:

$$\mathcal{E} = 2\partial_r\partial_r E - 2\frac{\partial_r E}{r}, \tag{4-27}$$

and ∂_r denotes a derivative with respect to the radial coordinate r. Which is completely equivalent to the one present in [63] with $A = \psi$, $C = \phi$, $B = \omega$ and $2E = \chi$:

$$ds^2 \;=\; a^2\Big[(1+2\psi)d\tau^2 - \left(1 - 2\phi + \frac{2}{3}\mathcal{E}\right)dr^2 - 2\omega' d\tau dr - \left(1 - 2\phi - \frac{1}{3}\mathcal{E}\right)r^2 d\Omega^2\Big] \tag{4-28}$$

where

$$\mathcal{E} = \chi'' - \frac{\chi'}{r}, \tag{4-29}$$

and the prime $'$ denotes derivative respect to r.

It is important to remember that this radial coordinate is comoving and it is related to the physical radius by (4-3).

In the next section, the Newton Gauge will be fixed. This gauge will allow a direct comparison between general relativity and Newtonian gravity. Additionally, the potentials in the Newton gauge will be equivalent to the Bardeen potentials, which will allow the turnaround radius computation in an arbitrary gauge.

4.4 Newton Gauge

To fix the gauge in spherical coordinates, fixing 2 of the 4 scalar potentials is enough. In the Newton gauge the fixed potentials are $B = E = 0$ which results in the following isotropic metric:

$$ds^2 = a^2(\tau)\left[(1+2A)d\tau^2 - (1+2C)\left(dr^2 + r^2 d\Omega^2\right)\right]. \tag{4-30}$$

According to (4-17), it is possible to achieve $E \to 0$ and $B \to 0$ with the following translations:

$$L = E, \tag{4-31}$$
$$T = E' - B. \tag{4-32}$$

Under this gauge transformation, the other two scalar potentials take a particular form:

$$\begin{aligned} &A \to A - (E'-B)' - \mathcal{H}(E'-B) \\ &A = \Psi, \\ \\ &C \to C - \mathcal{H}(E'-B) - \frac{1}{3}\nabla^2 E \\ &C = -\Phi. \end{aligned} \tag{4-33}$$

The previous perturbations in the Newton gauge, are equivalent to the Bardeen potentials. Therefore, the metric in the Newton gauge can be rewritten using gauge-invariant potentials:

$$ds^2 = a^2(\tau)\left[(1+2\Psi)d\tau^2 - (1-2\Phi)\left(dr^2 + r^2 d\Omega^2\right)\right]. \tag{4-34}$$

In general, these two potentials are different but in the absence of any anisotropy, they will be equal $\Phi = \Psi$ [64]. Under the Newton Gauge, considering that the Bardeen potentials depend on both time and radius, the non-null Christoffel symbols are:

$$
\begin{aligned}
\Gamma^0_{00} &= \frac{a'}{a} + \Psi', \\
\Gamma^0_{01} = \Gamma^0_{10} &= \partial_r \Psi, \\
\Gamma^0_{11} &= \frac{a'}{a}(1 - 2\Phi - 2\Psi) - \Phi', \\
\Gamma^0_{22} &= -\frac{a' r^2}{a}(1 - 2\Phi - 2\Psi) - \Phi', \\
\Gamma^0_{33} &= \Gamma^0_{22} \sin^2\theta, \\
\Gamma^1_{00} &= \partial_r \Psi, \\
\Gamma^1_{01} = \Gamma^1_{10} &= \frac{a'}{a} - \Phi', \\
\Gamma^1_{11} &= -\partial_r \Phi, \\
\Gamma^1_{22} &= -r + r^2 \partial_r \Phi, \\
\Gamma^1_{33} &= \Gamma^1_{22} \sin^2\theta, \\
\Gamma^2_{02} = \Gamma^2_{20} &= \frac{a'}{a} - \Phi', \\
\Gamma^2_{12} = \Gamma^2_{21} &= \frac{1}{r} - \partial_r \Phi, \\
\Gamma^2_{33} &= -\cos\theta \sin\theta, \\
\Gamma^3_{03} = \Gamma^3_{30} &= \frac{a'}{a} - \Phi', \\
\Gamma^3_{13} = \Gamma^3_{31} &= \frac{1}{r} - \partial_r \Psi, \\
\Gamma^3_{23} = \Gamma^3_{32} &= \cot\theta,
\end{aligned}
\tag{4-35}
$$

where, once again, the prime ($'$) denotes a derivative with respect to conformal time and ∂_r a derivative with respect to the comoving radius r. These connection coefficients will be used to obtain the radial geodesics for the perturbed metric to compute the turnaround radius.

5 Deep learning merger masses estimation from gravitational waves signals in the frequency domain

We present the results of applying Convolutional Neural Networks (CNN) to the frequency domain data of a Gravitational Wave merger signal (GW), i.e., the Fourier transform of the time domain strain data. We call this neural network FCNN to distinguish it from the CNN applied to time domain data, denoted as TCNN.

The FCNN relies on the short-time Fourier transform to extract the frequency domain features needed to train the network. This approach reduces the input's dimensionality, and the FCNN has around 50.000 parameters, compared with almost 550.000 of the TCNN. Consequently, FCNN has better out-of-sample performance than TCNN and tends to also have a lower over-fit due to the significantly lower model complexity.

In this section, we consider different sources of gravitational waves. Current observations from the LIGO and Virgo collaborations confirm the luminal propagation of gravitational waves. These new results can be used to constrain modified gravity theories such as Horndeski gravity [65].

5.1 Gravitational Waves

In order to understand the physics of gravitational waves it is useful to write the Einstein's equations in the weak field limit. All the calculations which follow are at first order in perturbations. The metric tensor can be written as

$$g_{\mu\nu} = \eta_{\mu\nu} + \epsilon h_{\mu\nu}, \tag{5-1}$$

where $\eta_{\mu\nu}$ is the Minkowski metric. The metric connection coefficients and the Riemann tensor are therfore

$$\Gamma^{\sigma}_{\mu\nu} = \frac{1}{2}\epsilon\left(h^{\sigma}{}_{\mu,\nu} + h^{\sigma}{}_{\nu,\mu} - h_{\mu\nu,}{}^{\sigma}\right), \tag{5-2}$$

$$R_{\mu\nu\sigma\rho} = \frac{1}{2}\epsilon\left(h_{\mu\rho,\nu\sigma} + h_{\nu\sigma,\mu\rho} - h_{\mu\sigma,\nu\rho} - h_{\nu\rho,\mu\sigma}\right). \tag{5-3}$$

The Ricci scalar and the Einstein tensor are respectively

$$R = \epsilon(h^{\mu\nu}{}_{,\mu\nu} - \Box h) \tag{5-4}$$

$$G_{\mu\nu} = \frac{1}{2}\epsilon({h^{\rho}}_{\mu,\nu\rho} + {h^{\rho}}_{\nu,\mu\rho} - \Box h_{\mu\nu} - h_{,\mu\nu} - \eta_{\mu\nu}{h^{\rho\sigma}}_{\rho\sigma} + \eta_{\mu\nu}\Box h), \tag{5-5}$$

where $\Box = \eta^{\mu\nu}\partial_\mu\partial_\nu$ is the d'Alambertian operator. In the Einstein's gauge, defined by ${h^{\mu}}_{\nu,\mu} - h_{,\nu}/2 = 0$, using eq.(5-5), the vacuum Einstein's equations become a wave equation for the metric perturbation

$$\Box h_{\mu\nu} = 0. \tag{5-6}$$

The solution in presence of a source can be written in the transverse-traceless gauge as [66]

$$h_{jk} = \frac{2}{r}\ddot{Q}_{jk}(t-r). \tag{5-7}$$

where Q is the mass quadrupole moment. Possible sources are systems with a large quadrupole moment such as coalescing black holes or neutron stars, asymmetric spinning bodies, or supernovae.

We will focus on gravitational waves generated by binary mergers, which were first detected by the LIGO collaboration [2]. Binary black hole mergers lose energy in the form of gravitational waves as they orbit each other, which causes their inspiral. The gravitational wave emission peaks during the merger phase, while the remaining black hole, with a null quadrupole mass moment, no longer generates gravitational wave radiation.

Without an analytical solution to the general relativity two-body problem, the evolution of the binary system must be modeled and approximated using a combination of methods. The post-Newtonian theory applies during the initial inspiral phase when both black holes are sufficiently apart. The merger phase, which involves the strong gravity regime, starts once the black holes cross the innermost stable circular orbit. In this phase the quadrupole formula (5-7) is not an accurate approximation and the full Einstein's equations must be solved numerically. In the ringdown phase after the merger the Einstein's equations can be solved numerically or an approximate analytical solution can be obtained by perturbing the Kerr's solution.

The waveforms in this thesis are computed using the package PyCBC [67], which uses the effective one-body formalism. A waveform example is shown in figure **5-1**.

5.2 Training Data generation

The training data is generated using the PyCBC package, developed by the PyCBC Development Team and the LIGO / Virgo Collaborations, whose purpose is the study of gravitational waves.

This library contains a method to generate the waveform corresponding to a GW event and accepts as inputs several different parameters. In the waveform generation, we assumed for simplicity the spins and orbital eccentricities to be zero, as in [10]. Data with $\pi/2$ polarization was also generated to evaluate the robustness of the neural network to signals with different parameters. The networks were trained to predict the two masses of the merger, while other parameters were kept fixed in the data generation.

We kept the default values for the other parameters of the waveform generator function except for The approximant is chosen to be the fourth version of Spin Effective One Body Numerical Relativity (SEOBNR) due to its efficiency. An example of a merger GW simulated signal is shown in fig.(**5-1**).

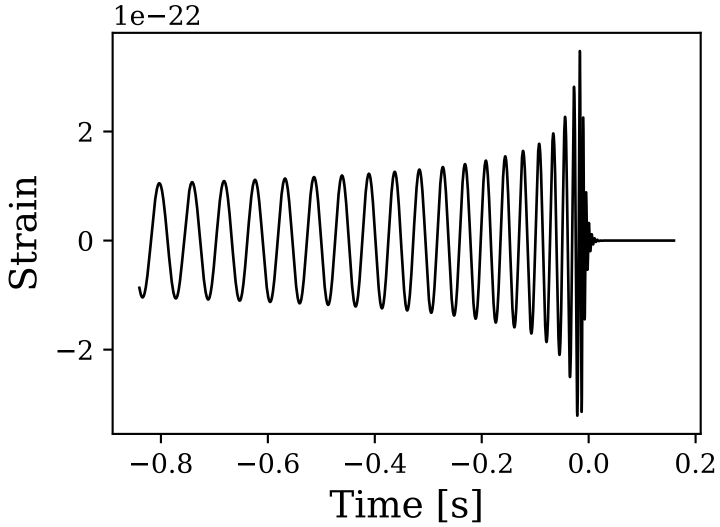

Figure 5-1: Simulated strain of a black hole merger with 57 and 33 solar masses at a distance of 2000 MPc, sampled at 8192 Hz.

We add noise to the simulated signal to train the networks with realistic data. Similarly to [10], to account for translations in the signal, the data was augmented by applying a random temporal shift in the interval [0,0.2]. We generated data with different signal-to-noise ratios (SNR), and colored noise was added according to LIGO's power spectral density (PSD).

The matched-filter SNR between a template h and a signal s is defined by [68]:

$$SNR = \frac{|\langle s|h\rangle(t)|^2}{\langle h|h\rangle}, \tag{5-8}$$

the bracket notation involves the following correlation:

$$\langle s|h\rangle(t) = 4\int_0^\infty \frac{\hat{s}(f)\hat{h}(f)}{S_n(f)}e^{2\pi i f t}df, \tag{5-9}$$

where $\hat{s}$ and $\hat{h}$ are the Fourier transforms of the signal and template, respectively, and S_n is the PSD of the detector. An example of the signal and the corresponding noised signal is shown in fig.(**5-2**).

We train the FCNN using spectrograms, which are two-dimensional matrices whose columns are related to the frequency power spectra of the strain ST at different times, according to

$$SP_\omega = 10 * \log_{10}(|ST_\omega|^2)\,, \tag{5-10}$$

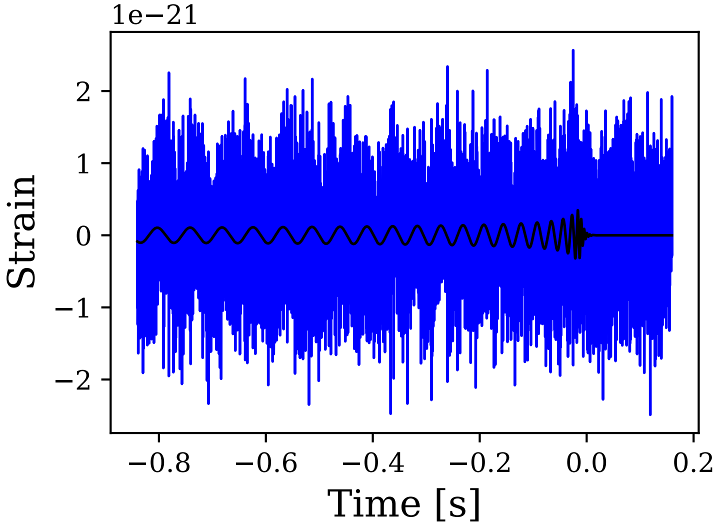

Figure 5-2: Simulated strain superimposed with noise sampled from LIGO's aLIGOZeroDetHighPower PSD, with a SNR of 18.5.

where SP_ω is the spectrogram, and ST_ω is the Fourier transform of ST over different time intervals.

The spectrograms are obtained by performing a Fast Fourier Transform (FFT) using equally spaced time intervals, with a sampling frequency of 4096 Hz, windows of 128 elements, a zero-padding of 896 elements, and overlap between windows of 64 elements.

The spectrogram of a merger GW signal is shown in fig.(**5-3**), and the spectrogram of the corresponding noised signal is shown in fig.(**5-4**), where it can be seen that the merger signal is mainly noticeable at low frequency. Consequently, to train the FCNN, the spectrograms were cropped at 120 Hz.

5.3 CNN architectures

The TCNN described in [10], summarized in Table **5-1**, was implemented as a benchmark to compare the performance of the FCNN.

The FCNN, whose architecture is shown in Table **5-2**, consists of three convolutional layers that perform 2D convolutions on the zero-padded signal, followed by a max-pooling layer. The resulting output of the pooling layer is then flattened into a one-dimensional vector of 1024 entries, which is fed into a two-layer fully connected net that predicts the two masses of the merger.

The FCNN has about 50.000 parameters, compared with almost 550.000 of the TCNN. The smaller number of parameters has a regularization effect by reducing the variance of the model, making it less prone to over-fitting as the number of degrees of freedom is significantly reduced. This is achieved because the spectrogram reduces the total number of input

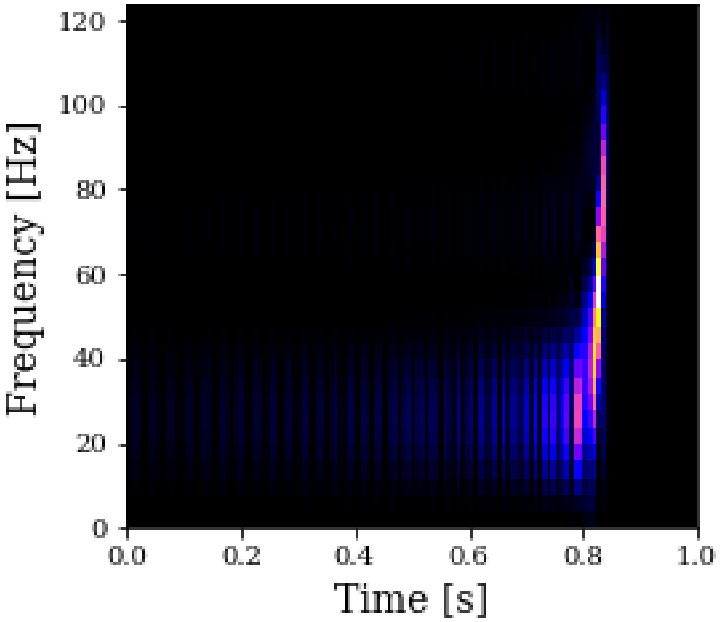

Figure 5-3: Spectrogram of the GW signal of a binary black hole merger with 33 and 57 solar masses.

components, the number of convolutions is less than the TCNN, and the two-dimensional pooling operation reduces the number of components more than the one-dimensional pooling. The latter significantly reduces the number of input components before the flatten layer and the number of parameters in the subsequent dense layers.

To improve the performance of the models, the input data was normalized before training. The normalization that gave the best results was the min-max scaling defined by

$$SP_{\omega\, norm} = \frac{SP_\omega - \min(SP_\omega)}{\max(SP_\omega) - \min(SP_\omega)} \tag{5-11}$$

5.4 Over-fit

When the training set error is very low, there is a risk of over-fitting due to a high number of parameters, which manifests in a significant difference between the training and validation errors. Even if the model's error on the training set reaches low values, it does not necessarily imply that its predictive ability, when applied on data different from the training set, will be as good. To quantify the difference between the training and the validation errors, we define the following over-fitting estimator.

$$\mathrm{O} = \left| \frac{\text{train error } - \text{ test error}}{\text{test error}} \right| . \tag{5-12}$$

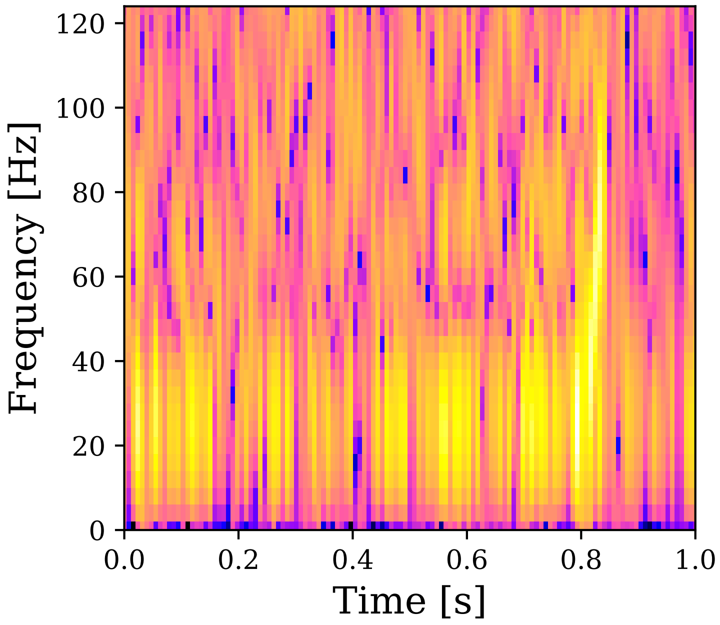

Figure 5-4: Spectrogram of the noised GW signal of a binary black hole merger of 57 and 33 solar masses and SNR=18.5.

Low values of the over-fitting estimator correspond to a slight relative difference between the training and validation errors, implying the model will have a performance on out-of-sample data similar to the one on training data.

5.5 Training Metric

This model aims to predict the masses of the merger from the spectrogram of the gravitational wave's strain signal. We train the model by iteratively minimizing the mean absolute percentage error (MAPE) each epoch, defined as

$$MAPE = \frac{1}{n}\sum_{i=1}^{n}\sum_{j=1}^{2}\left|\frac{\hat{M}_{ij} - M_{ij}}{M_{ij}}\right| \tag{5-13}$$

where n is the number of samples in each epoch, $\hat{M}_{i1}$ and $\hat{M}_{i2}$ are the masses of the merger predicted by the model, while M_{i1} and M_{i2} are the masses from the training set used in the simulation for the i-th sample.

5.6 Comparing FCNN to TCNN performance

The merger GW data was simulated with a sampling rate of 8192 Hz, generated for mass values from $10M_{\odot}$ to $75M_{\odot}$, with a mass ratio less than ten and a distance of 2000 MPc,

	Layer	Size
	Input	vector (8192)
1	Convolution (ReLu)	matrix (8192 × 16)
2	Pooling	matrix (2048 × 16)
3	Convolution(ReLu)	matrix (2048 × 32)
4	Pooling	matrix (512 × 32)
5	Convolution (ReLu)	matrix (512 × 64)
6	Pooling	matrix (128 × 64)
7	Flatten	vector(8192)
8	Dense layer (ReLu)	vector (64)
	Output	vector (2)

Table 5-1: Architecture of the TCNN used in [10].

	Layer	Size
	Input	matrix (32 × 127 × 1)
1	Convolution (ReLu)	matrix (32 × 127 × 16)
2	Convolution (ReLu)	matrix (32 × 127 × 8)
3	Convolution (ReLu)	matrix (32 × 127 × 4)
4	Pooling	matrix (8 × 32 × 4)
5	Flatten	vector(1024)
6	Dense layer (ReLu)	vector (32)
7	Dense layer (ReLu)	vector (16)
	Output	vector (2)

Table 5-2: Architecture of the FCNN.

resulting in a total of 9346 mergers with SNRs in the 5 to 25 range. The data was split evenly between modeling and validation sets as shown in fig.(**5-5**). The modeling set was further split with a 70/30 ratio into training and development sets. The training set was used to optimize the model parameters, and the development set was used for hyperparameter tuning, specifically to find better performance performing network architectures. The same procedure was applied to the two data sets simulated with polarization equal to 0 and $\pi/2$.

The error of FCNN and TCNN models on the validation data over the range of SNRs is shown in fig.(**5-6**) for data with polarization equal to 0.

In fig.(**5-7**), the over-fit of the two models over the range of SNRs is shown, as defined in eq.(5-12). As mentioned earlier, the FCNN has much fewer parameters than TCNN, and it is expected to have a lower over-fit than TCNN.

To test the robustness of the models under the change of other merger parameters, we also created another set of training and validation data using a different polarization angle. Gravitational-wave signals with a polarization angle of $\pi/2$ were simulated, keeping all other

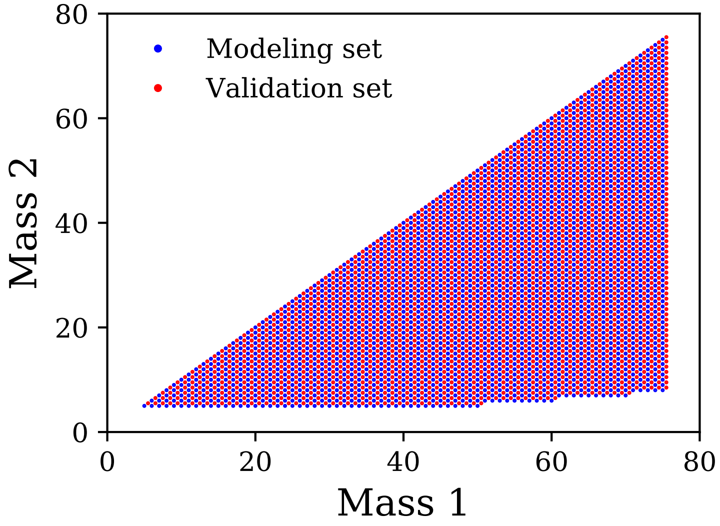

Figure 5-5: Scatter plot of the mass pairs used to simulate the data. The modelling and validation data sets are chosen as in [10].

parameters fixed. We used the same number of simulated samples, and the masses of the mergers ranged from $10M_\odot$ to $75M_\odot$ with a mass ratio less than or equal to 10.

The error of the TCNN and FCNN models on the validation set for data with polarization equal to $\pi/2$ is shown in fig.(**5-9**). Likewise, the over-fit of TCNN models for this data is shown in fig.(**5-10**). The FCNN over-fit was lower than for TCNN, suggesting that FCNN generalizes better than TCNN on signals from gravitational waves with different parameters.

As can be seen in fig.(**5-6**) and fig.(**5-9**), the performance of TCNN and FCNN is approximately the same, but for low SNRs, the FCNN is slightly better. Nonetheless, from the over-fit plots, it can be seen that thanks to the reduced number of parameters, FCNN has a better out-of-sample performance. A comparison of the MAPE of the mass predictions for out-of-sample data is shown in fig.(**5-8**).

The execution time of the FCNN is, in general, much lower than the TCNN because the FCNNs have much fewer parameters. If we add to this execution time the time necessary to compute the spectrogram using scipy.signal.spectrogram, we obtain a total computational time which is on average only about 6% greater than that of a CNN working on the time domain data, but with a better MAPE and less over-fit due to the smaller number of parameters. Using more efficient implementations of the FFT to compute the spectrogram and parallelizing it could reduce the FCNN pipeline execution time.

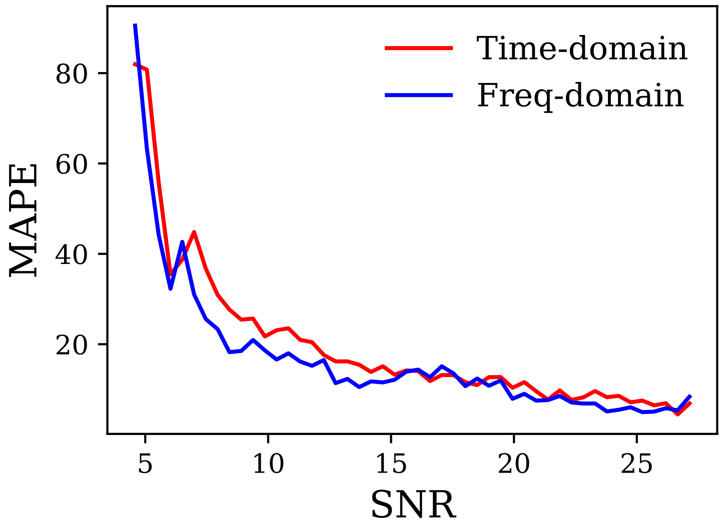

Figure 5-6: The MAPE of the TCNN and FCNN models, evaluated on the validation data set with a polarization equal to 0, is plotted as a function of the SNR.

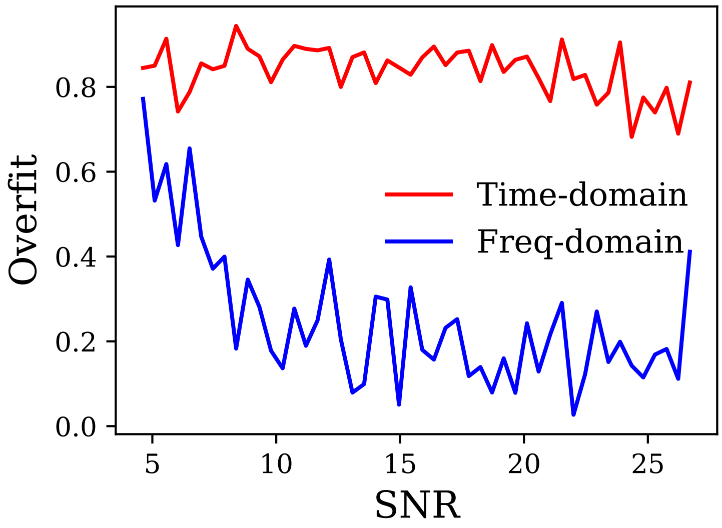

Figure 5-7: The over-fit estimator, as defined in eq.(5-12), is plotted for TCNN and FCNN models as a function of the SNR, for data with polarization equal to 0.

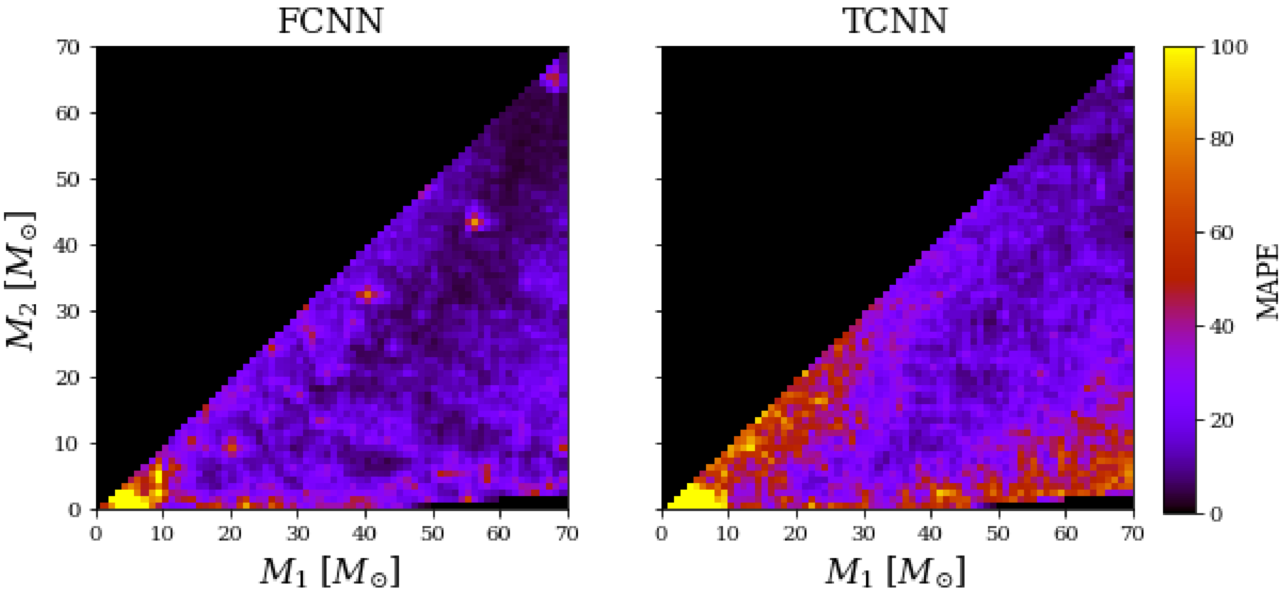

Figure 5-8: The MAPE of the prediction for out sample data with SNR=10 is plotted for different mass pairs.

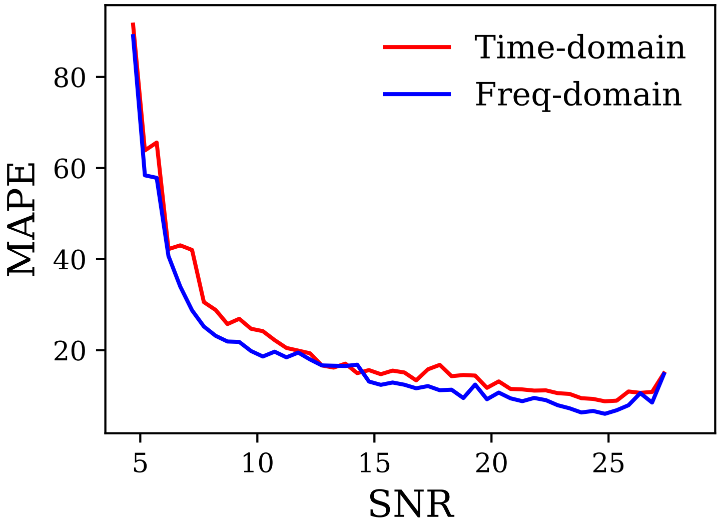

Figure 5-9: The MAPE of the TCNN and FCNN models, evaluated on the validation data set with a polarization equal to $\pi/2$, is plotted as a function of the SNR.

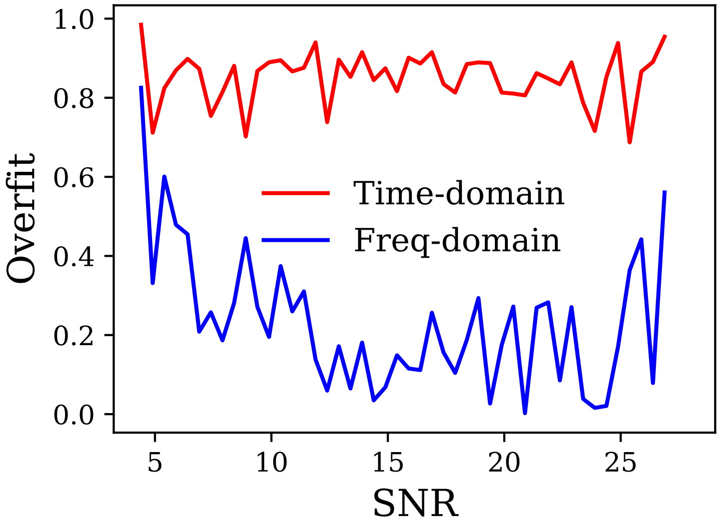

Figure 5-10: The over-fit estimator, as defined in eq.(5-12), is plotted for TCNN and FCNN models as a function of the SNR, for data with polarization equal to $\pi/2$.

6 Schwarzschild-de Sitter (SDS) Metric

The Schwarzschild-de Sitter's metric describes a spherically symmetric space-time in an expanding universe. It is pretty helpful to study Schwarzschild and de Sitter metrics separately before diving into the Schwarzschild-de Sitter metric, which has a lot of common properties with both. The Schwarzschild metric will be analyzed first, along with its singularity and event horizon; a coordinate transformation will be used to show that the event horizon is not a space-time singularity. On the other hand, the de Sitter metric, being the simplest solution to Einstein's field equations with a cosmological constant, will be analyzed along with its cosmological horizon. Another coordinate transformation will be used to prove the equivalence with a flat FLRW metric, which allows the de Sitter metric to be used as a background solution under Cosmological perturbation theory. All of the relevant quantities will be computed for both metrics, such as the Riemann, Ricci, and Einstein tensors; the Christoffel symbols, and the Ricci scalar.

Finally, the Schwarzschild-de Sitter metric will be derived in static coordinates and transformed to isotropic coordinates and a perturbative regime with linear approximations. For an in-depth study of black holes, [69] is recommended.

6.1 Schwarzschild Metric

The Schwarzschild metric was the first exact, non-trivial solution to Einstein's field equations [70]. Karl Schwarzschild obtained this solution through symmetry considerations in 1915 and was published in 1916. According to Birkhoff's theorem, the spherical limit in general relativity implies a static metric, and under these static coordinates, the metric takes the following form:

$$ds^2 = \left(1 - \frac{2m}{R}\right) dT^2 - \left(1 - \frac{2m}{R}\right)^{-1} dR^2 - R^2 \left(d\theta^2 + \sin^2\theta d\phi^2\right). \tag{6-1}$$

At first sight, this metric appears to have singularities at both $R = 0$ and $R = 2m$, but the singularity at $R = 2m$, known as the Schwarzschild radius, is not physical and it is due only to the coordinate system chosen by Schwarzschild. This singularity disappears by using Eddington-Finkelstein coordinates:

$$\tilde{R} = R + 2m \log\left(\frac{R}{2m} - 1\right), \tag{6-2}$$

$$\tilde{T} = T \pm \tilde{R}, \tag{6-3}$$

where the sign ± depends on the sign of $\tilde{T}$ for incoming or outgoing null geodesics, which correspond to advanced or retarded coordinates respectively. Under these coordinates, the metric is written as

$$ds^2 = \left(1 - \frac{2m}{R}\right) d\tilde{T}^2 - 2d\tilde{T}d\tilde{R} - \tilde{R}^2\left(d\theta^2 + \sin^2\theta d\phi^2\right). \tag{6-4}$$

There is no longer a singularity at $R = 2m$ but the sign of the g_{00} component changes when $R < 2m$. If the radial geodesics are plotted, it is possible to see that when a particle or light ray crosses this horizon, it cannot go back under advanced Eddington-Finkelstein coordinates. Under these coordinates, the metric also has a singularity in the origin, such as (6-1). This singularity is a space-time singularity according to the Kretschmann scalar:

$$K = \frac{48m^2}{R^6}. \tag{6-5}$$

The connection coefficients in spherical coordinates for the metric (6-1) are

$$\begin{aligned}
\Gamma^0_{01} = \Gamma^0_{10} &= -\frac{m}{2mR - R^2}, \\
\Gamma^1_{00} &= \frac{m(R-2m)}{R^3}, \\
\Gamma^1_{11} &= -\frac{m}{2mR - R^2}, \\
\Gamma^1_{33} = \sin^2\theta\Gamma^1_{22} &= (2m - R)\sin^2\theta, \\
\Gamma^2_{12} = \Gamma^2_{21} &= \frac{1}{R}, \\
\Gamma^2_{33} &= -\cos\theta\sin\theta, \\
\Gamma^3_{13} = \Gamma^3_{31} &= \frac{1}{R}, \\
\Gamma^3_{23} = \Gamma^3_{32} &= \cot\theta,
\end{aligned} \tag{6-6}$$

which shows that under the weak field limit $\Gamma^i_{00} = \frac{m}{R}$ in accordance to (3-40). With these coefficients, it is possible to compute the non-null components of the Riemann tensor:

$$\begin{aligned}
R_{0101} &= \frac{2m}{R^3}, \\
R_{0202} &= \frac{m(2m-R)}{R^2}, \\
R_{0303} &= R_{0202}\sin^2\theta, \\
R_{1212} &= -\frac{m}{2m-R}, \\
R_{1313} &= R_{1212}\sin^2\theta, \\
R_{2323} &= 2mR\sin^2\theta,
\end{aligned} \tag{6-7}$$

where the other coordinates are either zero or determined by the tensor's symmetry properties. It is important to note that, even if this metric describes a spherically symmetric mass distribution, Schwarzschild's metric is an exterior solution to Einstein's field equations in a vacuum. Therefore, the Einstein tensor, Ricci tensor, and Ricci scalar are zero.

6.2 de Sitter Universe

If a cosmological constant is included in Einstein's equations, the simplest solution is de Sitter's metric. This metric describes an expanding universe, which is useful to model dark energy. In static coordinates it is described by the following line interval:

$$ds^2 = \left(1 - \frac{\Lambda}{3}R^2\right) dT^2 - \left(1 - \frac{\Lambda}{3}R^2\right)^{-1} dR^2 - R^2\left(d\theta^2 + \sin^2\theta d\phi^2\right), \tag{6-8}$$

in this case, there is an event horizon at $r = \sqrt{3/\Lambda}$, known as the cosmological horizon. As in the Schwarzschild horizon, it is possible to do a coordinate transformation to remove the singularity at $r = \sqrt{3/\Lambda}$. The de-Sitter metric can also be written in isotropic coordinates according to the following coordinate transformation

$$\begin{aligned} R &= a(t)r\ , && \text{(6-9)} \\ T &= t - \frac{1}{2H}\log(r^2a^2(t) - H^{-2})\,, && \text{(6-10)} \\ ds^2 &= dt^2 - a^2(t)(dr^2 + r^2d\Omega^2), && \text{(6-11)} \end{aligned}$$

where $a(t) = e^{Ht} = e^{t/l}$ is the scale factor and $l^2 = \frac{3}{\Lambda}$. This metric is equivalent to a flat FLRW metric with a scale factor $a(t) = e^{t/l}$. In this work, the de Sitter metric will be chosen as the background solution for cosmological perturbation theory. Additionally, under conformal time the metric is

$$ds^2 = a^2(\tau)\left[d\tau^2 - \left(dr^2 + r^2d\Omega^2\right)\right], \tag{6-12}$$

or in cartesian coordinates

$$ds^2 = a^2(\tau)\left[d\tau^2 - \delta_{ij}dx^idx^j\right]. \tag{6-13}$$

This last expression is similar to the metric of cosmological perturbations in conformal time and comoving coordinates.

The non-null connection coefficients for the static metric (6-8) are

$$\begin{aligned}
\Gamma^0_{01} = \Gamma^0_{10} &= \frac{R\Lambda}{r^2\Lambda - 3},\\
\Gamma^1_{00} &= \frac{1}{9}R\Lambda(R^2\Lambda - 3),\\
\Gamma^1_{11} &= \frac{R\Lambda}{R^2\Lambda - 3},\\
\Gamma^1_{33} = \sin^2\theta\Gamma^1_{22} &= \frac{1}{3}R(R^2\Lambda - 3)\sin^2\theta,\\
\Gamma^2_{12} = \Gamma^2_{21} &= \frac{1}{R},\\
\Gamma^2_{33} &= -\cos\theta\sin\theta,\\
\Gamma^3_{13} = \Gamma^3_{31} &= \frac{1}{R},\\
\Gamma^3_{23} = \Gamma^3_{32} &= \cot\theta.
\end{aligned} \tag{6-14}$$

The non-null and independent components of the Riemann tensor are:

$$\begin{aligned}
R_{0101} &= \frac{\Lambda}{3},\\
R_{0202} &= -\frac{R^2\Lambda}{9}(R^2\Lambda - 3),\\
R_{0303} &= R_{0202}\sin^2\theta,\\
R_{1212} &= \frac{R^2\Lambda}{R^2\Lambda - 3},\\
R_{1313} &= R_{1212}\sin^2\theta,\\
R_{2323} &= -\frac{R^4\Lambda\sin^2\theta}{3}.
\end{aligned} \tag{6-15}$$

In this case, this is not a vacuum solution due to the cosmological constant. Therefore, the Ricci tensor is diagonal but not null:

$$\begin{aligned}
R_{00} &= \frac{\Lambda}{3}(R^2\Lambda - 3),\\
R_{11} &= \frac{3\Lambda}{3 - R^2\Lambda},\\
R_{22} &= R^2\Lambda,\\
R_{33} &= R_{22}\sin^2\theta,
\end{aligned} \tag{6-16}$$

which implies that the Ricci scalar is constant $\mathcal{R} = -4\Lambda$. The Kretschmann scalar is also constant $K = \frac{8\Lambda^2}{3}$ and, as expected, there is no singularity at the cosmological horizon.

Finally, the non-null components of the Einstein tensor are

$$\begin{aligned} G_{00} &= -\frac{\Lambda}{3}(R^2\Lambda - 3), \\ G_{11} &= -\frac{3\Lambda}{3 - R^2\Lambda}, \\ G_{22} &= -R^2\Lambda, \\ G_{33} &= -G_{22}\sin^2\theta, \end{aligned} \tag{6-17}$$

In the following section, a Dirac delta will be used to derive the Schwarzschild-de Sitter metric and fix integration constants, without the need to use the weak field limit or to find a correspondence between an inner and outer solution. Schwarzschild coordinates will be used to derive this metric, but it will also be written in isotropic coordinates.

6.3 Schwarzschild-de Sitter Metric in Static Coordinates

The most general spherically symmetric metric is:

$$ds^2 = AdT^2 - 2BdTdR - CdR^2 - Dd\Omega^2, \tag{6-18}$$

where $d\Omega^2 = d\theta^2 + \sin^2(\theta)d\phi^2$ is the line element of the 2-dimensional sphere and A, B, C, D are functions of both T and T to be determined. Through the redefinition of the radial coordinate $\tilde{R} = R\sqrt{D}$, the metric becomes:

$$ds^2 = \tilde{A}dT^2 - 2\tilde{B}dTd\tilde{R} - \tilde{C}d\tilde{R}^2 - \tilde{R}^2d\Omega^2. \tag{6-19}$$

Considering the following expression:

$$\tilde{A}dT - \tilde{B}d\tilde{R}, \tag{6-20}$$

according to differential equations theory, it is possible to build an exact differential multiplying by an integration function. With this result, a new time coordinate can be built:

$$d\tilde{T} = I(\tilde{A}dT - \tilde{B}d\tilde{R}), \tag{6-21}$$

$$d\tilde{T}^2 = I^2(\tilde{A}dT - \tilde{B}d\tilde{R})^2 = I^2(\tilde{A}^2dT^2 - 2\tilde{A}\tilde{B}dTd\tilde{R} + \tilde{B}^2d\tilde{R}^2). \tag{6-22}$$

It is possible to reorder the following terms in the metric:

$$\tilde{A}dT^2 - 2\tilde{B}dTd\tilde{R} = \frac{d\tilde{T}^2}{\tilde{A}I^2} - \frac{\tilde{B}^2d\tilde{T}^2}{\tilde{A}}, \tag{6-23}$$

in order to rewrite the metric without a crossed term $dTd\tilde{R}$:

$$\begin{aligned} ds^2 &= \frac{d\tilde{T}^2}{\tilde{A}I^2} - \frac{\tilde{B}^2d\tilde{R}^2}{\tilde{A}} - \tilde{C}d\tilde{R}^2 - \tilde{R}^2d\Omega^2 \\ &= Ad\tilde{T}^2 - Bd\tilde{R}^2 - \tilde{R}^2d\Omega^2, \end{aligned} \tag{6-24}$$

where the following definition was used in the last step:

$$
\begin{aligned}
A(T,R) &= \frac{1}{\tilde{A}I^2},\\
B(T,R) &= \tilde{C} + \frac{\tilde{B}}{\tilde{A}^2}.
\end{aligned}
\tag{6-25}
$$

The only non-null components of the Einstein tensor corresponding to the metric (6-24) are:

$$
G_{00} = \frac{A\left(RB' + (B-1)B\right)}{R^2B^2}, \tag{6-26}
$$

$$
G_{01} = \frac{\dot{B}}{RB}, \tag{6-27}
$$

$$
G_{11} = \frac{\frac{RA'}{A} - B + 1}{R^2}, \tag{6-28}
$$

$$
G_{33} = \frac{AR\left[R\left(\dot{B}^2 - \partial_R A \partial_R B\right) + 2B\left(\partial_R A + R\partial_R\partial_R A - R\ddot{B}\right)\right] + R^2B\left[\dot{A}\dot{B} - (\partial_R A)^2\right] - 2A^2R\partial_R B}{4A^2B^2}, \tag{6-29}
$$

$$
G_{33} = \sin^2(\theta)G_{22}, \tag{6-30}
$$

where ∂_R is a derivative with respect to the radial coordinate and the dot $(\dot{})$ is a time derivative. Given that the only non-null component of the energy-momentum tensor $T_{\mu\nu}$ will be the one corresponding to the density T_{00}, Einstein field equations yield $G_{01} = 0$, which results in $\dot{B} = 0$ and the dependence of B will be only radial. Additionally, considering a cosmological constant:

$$
\begin{aligned}
G_{00} - \Lambda g_{00} &= \frac{A\left(R\partial_R B + (B-1)B\right)}{R^2B^2} - \Lambda A\\
&= \left[\frac{R\partial_R B + (B-1)B}{R^2B^2} - \Lambda\right]A\\
&= \left[1 - \partial_R\left(\frac{R}{B}\right) - \Lambda R^2\right]\frac{A}{R^2}.
\end{aligned}
\tag{6-31}
$$

The only matter content to be considered is a point mass in the origin, which has the following mass density $\rho = \frac{m\delta(R)}{4\pi R^2}$, where $\delta(R)$ is the Dirac delta function. Therefore, as in [71] the energy-momentum tensor is:

$$
T^{\mu}{}_{\nu} = \begin{pmatrix} \rho & 0 & 0 & 0\\ 0 & 0 & 0 & 0\\ 0 & 0 & 0 & 0\\ 0 & 0 & 0 & 0 \end{pmatrix}. \tag{6-32}
$$

According to Einstein field equations, $G_{00} - \Lambda g_{00} = 8\pi T_{00}$ which can be integrated to find B:

$$
\begin{aligned}
8\pi g_{00}\rho &= \left[1 - \partial_R\left(\frac{R}{B}\right) - \Lambda R^2\right]\frac{A}{R^2},\\
2m\frac{A}{R^2}\delta(R) &= \left[1 - \partial_R\left(\frac{R}{B}\right) - \Lambda R^2\right]\frac{A}{R^2},\\
\partial_R\left(\frac{R}{B}\right) &= 1 - \Lambda R^2 - 2m\delta(R),\\
\frac{R}{B} &= R - \frac{\Lambda}{3}R^3 - 2m,\\
\frac{1}{B} &= 1 - \frac{\Lambda}{3}R^2 - \frac{2m}{R},\\
B &= \left(1 - \frac{\Lambda}{3}R^2 - \frac{2m}{R}\right)^{-1}.
\end{aligned}
\tag{6-33}
$$

Substituting B into the G_{11} equation

$$
\begin{aligned}
G_{11} - \Lambda g_{11} &= \frac{\frac{R\partial_R A}{A} - \frac{3\Lambda R^3 + 3R}{-6m + \Lambda R^3 + 3R} + 1}{R^2},\\
0 &= \frac{R\partial_R A}{A} - \frac{-3\Lambda R^3 + 3R}{-6m + \Lambda R^3 + 3R} + \frac{-6m + \Lambda R^3 + 3R}{-6m + \Lambda R^3 + 3R},\\
\frac{R\partial_R A}{A} &= \frac{3\Lambda R^3 - 6m}{-6m + \Lambda R^3 + 3R},\\
\partial_R(\log A) &= \frac{3\Lambda R^3 - 6m}{-6mR + \Lambda R^4 + 3R^2},
\end{aligned}
\tag{6-34}
$$

it can be integrated to find A:

$$A = 3\left(1 - \frac{\Lambda}{3}R^2 - \frac{2m}{R}\right)D(T), \tag{6-35}$$

where $D(t)$ is an integration constant. The resulting metric is:

$$ds^2 = 3D(T)\left(1 - \frac{2m}{R} - \frac{\Lambda}{3}R^2\right)dT^2 - \left(1 - \frac{2m}{R} - \frac{\Lambda}{3}R^2\right)^{-1}dR^2 - R^2 d\Omega^2. \tag{6-36}$$

Finally, it is possible to reabsorb the function D with a time coordinate redefinition such that

$$3D(T)dT \to dT. \tag{6-37}$$

After this coordinate transformation, the Schwarzschild-de Sitter metric in static coordinates is obtained:

$$ds^2 = \left(1 - \frac{2m}{R} - \frac{\Lambda}{3}R^2\right)dT^2 - \left(1 - \frac{2m}{R} - \frac{\Lambda}{3}R^2\right)^{-1}dR^2 - R^2 d\Omega^2. \tag{6-38}$$

This metric has the same terms as the Schwarzschild (6-1) and de Sitter (6-8) metrics. Therefore, it will have the singularity at the origin and both the Schwarzschild and cosmological horizons. However, the region between both horizons ($2m \ll R \ll \sqrt{3/\Lambda}$) will be approximately flat.

6.3.1 Christoffel Symbols and Curvature Tensors

The connection coefficients are useful when computing the geodesics and curvature tensors; with that in mind, a list of the non-null Christoffel symbols is presented in this section along with the Ricci scalar and Riemann, Ricci, and Einstein tensors. These quantities must match the ones corresponding to the Schwarzschild metric in the $\Lambda \to 0$ limit and the de Sitter ones in the $m \to 0$ limit.

$$\begin{aligned}
\Gamma^0_{01} = \Gamma^0_{10} &= \frac{-3m + \Lambda R^3}{6mR - 3R^2 + \Lambda R^4}, \\
\Gamma^1_{00} &= \frac{\left(\Lambda R^3 - 3m\right)\left(6m - 3R + \Lambda R^3\right)}{9R^3}, \\
\Gamma^1_{11} &= \frac{3m - \Lambda R^3}{6mr - 3R^2 + \Lambda R^4}, \\
\Gamma^1_{22} &= 2m - R + \frac{\Lambda}{3}R^3, \\
\Gamma^1_{33} &= \Gamma^1_{22}\sin^2\theta, \\
\Gamma^2_{12} = \Gamma^2_{21} &= \frac{1}{R}, \\
\Gamma^2_{33} &= -\cos\theta\sin\theta, \\
\Gamma^3_{13} = \Gamma^3_{31} &= \frac{1}{R}, \\
\Gamma^3_{23} = \Gamma^3_{32} &= \cot\theta.
\end{aligned} \tag{6-39}$$

Effectively, all of the components match (6-6) when $\Lambda \to 0$ and (6-14) when $m \to 0$. With these connection coefficients, the non-null components of the Riemann tensor are computed

$$\begin{aligned}
R_{0101} &= \frac{\Lambda}{3}, \\
R_{0202} &= -\frac{(3m - R^3\Lambda)(6m - 3R + R^3\Lambda)}{R^2}, \\
R_{0303} &= R_{0202}\sin^2\theta, \\
R_{1212} &= \frac{R^3\Lambda - 3m}{6m - 3R + R^3\Lambda}, \\
R_{1313} &= R_{1212}\sin^2\theta, \\
R_{2323} &= -\frac{R}{3}(6m + R^3\Lambda)\sin^2\theta,
\end{aligned} \tag{6-40}$$

which once again match (6-7) and (6-15) on the respective limits. According to this, the Ricci tensor is

$$\begin{aligned} R_{00} &= \frac{\Lambda(R^3\Lambda - 3R + 6m)}{3R}, \\ R_{11} &= -\frac{3R\Lambda}{R^3\Lambda - 3R + 6m}, \\ R_{22} &= R^2\Lambda, \\ R_{33} &= R_{22}\sin^2\theta. \end{aligned} \tag{6-41}$$

Even though there are mass terms in the Ricci tensor, all components are zero when $\Lambda \to 0$, which matches the Schwarzschild case. From here, the Ricci curvature scalar can be computed, and it matches completely with the de Sitter case, with no mass terms

$$\mathcal{R} = -4\Lambda, \tag{6-42}$$

which implies that the mass has no asymptotic effects and is only a local perturbation. The Einstein tensor also has mass terms, but for $\Lambda \to 0$ and $m \to 0$, it matches the Schwarzschild and de Sitter metrics, respectively

$$\begin{aligned} G_{00} &= -\frac{\Lambda}{3}(R^2\Lambda - 3) - \frac{2m\Lambda}{R}, \\ G_{11} &= -\frac{3R\Lambda}{3 - R^2\Lambda - 6m}, \\ G_{22} &= -R^2\Lambda, \\ G_{33} &= -G_{22}\sin^2\theta. \end{aligned} \tag{6-43}$$

Lastly, the Kretschmann scalar is consistent with the previous metrics

$$K = \frac{48m^2}{R^6} + \frac{8\Lambda^2}{3}, \tag{6-44}$$

where the singularity at the center is still present.

6.4 Schwarzschild-de Sitter Metric in Isotropic Coordinates

According to [72] it is possible to write the Schwarzschild-de Sitter metric in isotropic coordinates. However, in these coordinates, the metric will no longer be static, but the spatial component of the metric will be equivalent to flat space in spherical coordinates. This metric is useful in the Newtonian limit, given that in this regime, time and space decouple by considering an absolute time separate from three-dimensional space. From the metric in static coordinates:

$$ds^2 = \left(1 - \frac{2m}{R} - \frac{\Lambda}{3}R^2\right) dT^2 - \frac{dR^2}{\left(1 - \frac{2m}{R} - \frac{\Lambda}{3}R^2\right)} - R^2 d\Omega^2, \tag{6-45}$$

the following coordinate transformation is done:

$$T = t + f(R), \tag{6-46}$$

$$R = e^{t/l} r + m + \frac{m^2}{4e^{t/l} r}, \tag{6-47}$$

where the function f is defined by:

$$\frac{df}{dR} = -\frac{R^2}{l\sqrt{R-m}(1 - \frac{m}{R} - \frac{R^2}{l^2})}. \tag{6-48}$$

In this coordinate system, the Schwarzschild-de Sitter metric is equivalent to the McVittie metric [73],[74]:

$$ds^2 = \left(\frac{1 - \frac{m}{2a(t)r}}{1 + \frac{m}{2a(t)r}} \right)^2 dt^2 - a(t)^2 \left(1 + \frac{m}{2a(t)r} \right)^4 \left[dr^2 + r^2 d\Omega^2 \right], \tag{6-49}$$

where the scale factor is $a(t) = \exp(t/l)$ and $l^2 = 3/\Lambda$. This metric can be written exactly in terms of conformal time through transformation given in (4-4)

$$ds^2 = a(\tau)^2 \left[\left(\frac{1 - \frac{m}{2a(\tau)r}}{1 + \frac{m}{2a(\tau)r}} \right)^2 d\tau^2 - \left(1 + \frac{m}{2a(\tau)r} \right)^4 \left(dr^2 + \rho^2 d\Omega^2 \right) \right], \tag{6-50}$$

Under the weak field limit, the metric is similar to the cosmological perturbation metric in the Newton gauge with $\Phi = \Psi = -\frac{m}{ar}$:

$$ds^2 = a(\tau)^2 \left[\left(1 - \frac{2m}{a(\tau)r} \right) d\tau^2 - \left(1 + \frac{2m}{a(\tau)r} \right) \left(dr^2 + r^2 d\Omega^2 \right) \right]. \tag{6-51}$$

7 Schwarzschild-de Sitter metric as the cosmological perturbation of an expanding Universe

The Schwarzschild-de Sitter metric can be interpreted as a cosmological perturbation metric in the region between both horizons and far from them $2m \ll r \ll \sqrt{3/\Lambda}$. The SDS metric in static coordinates is:

$$ds^2 = \left(1 - \frac{2m}{R} - H^2R^2\right) dT^2 - \left(1 - \frac{2m}{R} - H^2R^2\right)^{-1} dR^2 - R^2 d\Omega^2. \tag{7-1}$$

Our goal is to re-write it as a perturbation of the FRW metric, and we will achieve this by performing the coordinate transformation from static to comoving coordinates given in eq.(6-9) and eq.(6-10).

Far away from the Schwarzschild horizon ($m \ll R$) we get:

$$\begin{aligned} ds^2 = &\left[1 - \frac{2m\left(H^2r^2a^2+1\right)}{ar\left(H^2r^2a^2-1\right)^2}\right] dt^2 - a^2\left[1 + \frac{2m\left(H^2r^2a^2+1\right)}{ra\left(H^2r^2a^2-1\right)^2}\right] dr^2 \\ &- \left[\frac{8Hma}{\left(H^2r^2a^2-1\right)^2}\right] dt dr - r^2a^2 d\Omega^2, \end{aligned} \tag{7-2}$$

and after introducing conformal time $d\tau = dt/a(t)$

$$\begin{aligned} ds^2 = a^2 \Bigg\{ &\left[1 - \frac{2m\left(H^2r^2a^2+1\right)}{ra\left(H^2r^2a^2-1\right)^2}\right] d\tau^2 - \left[1 + \frac{2m\left(H^2r^2a^2+1\right)}{ra\left(H^2r^2a^2-1\right)^2}\right] dr^2 \\ &- \left[\frac{8Hm}{\left(H^2r^2a^2-1\right)^2}\right] d\tau dr - r^2 d\Omega^2 \Bigg\} . \end{aligned} \tag{7-3}$$

Comparing with equation (4-28) we obtain

$$\psi = -\frac{m\left(H^2r^2a^2+1\right)}{ra\left(H^2r^2a^2-1\right)^2}, \tag{7-4}$$

$$\phi = -\frac{H^2mr^2a^2+m}{3ra\left(H^2r^2a^2-1\right)^2}, \tag{7-5}$$

$$\omega' = \frac{4Hm}{\left(H^2r^2a^2-1\right)^2}, \tag{7-6}$$

$$\mathcal{E} = \frac{2\left(H^2mr^2a^2+m\right)}{ra\left(H^2r^2a^2-1\right)^2}. \tag{7-7}$$

After integrating eq.(4-29) and eq.(7-6) we finally get the scalar cosmological perturbations variables as defined in eq.(4-28)

$$
\begin{aligned}
\omega &= \frac{2m\tanh^{-1}(Hra)}{a} - \frac{2Hmr}{H^2r^2a^2-1}\,, && \text{(7-8)}\\
\chi &= \frac{2mr\left(Hra\tanh^{-1}(Hra)-1\right)}{a} + \frac{1}{2}r^2C(\tau) + D(\tau)\,, && \text{(7-9)}
\end{aligned}
$$

where C and D are functional constants of integration. Since we are only interested in perturbations that should vanish in a limit in which the mass vanishes, the physically interesting solutions correspond to $C = D = 0$.

Using CPT we can derive explicitly the gauge transformation between the static coordinates and the Newton gauge. Under an infinitesimal space-time translation of the form

$$
\begin{aligned}
\tilde{x}^0 &= x^0 + \zeta, && \text{(7-10)}\\
\tilde{x}^i &= x^i + \partial^i\beta, && \text{(7-11)}
\end{aligned}
$$

the gauge transformations are [63]

$$
\begin{aligned}
\tilde{\phi} &= \phi - \frac{1}{3}\nabla^2\beta + \frac{a_\tau}{a}\zeta, && \text{(7-12)}\\
\tilde{\omega} &= \omega + \zeta + \beta_\tau, && \text{(7-13)}\\
\tilde{\psi} &= \psi - \zeta_\tau - \frac{a_\tau}{a}\zeta, && \text{(7-14)}\\
\tilde{\chi} &= \chi + 2\beta\,, && \text{(7-15)}
\end{aligned}
$$

where we are denoting with a subscript the derivative respect to conformal time, i.e. for example $a_\tau = \frac{da}{d\tau}$. Imposing the Newton gauge condition

$$\omega_N = \chi_N = 0, \tag{7-16}$$

after solving the differential equations (7-13) and (7-15) we get

$$
\begin{aligned}
\beta_N &= mr\left[\frac{1}{a} - Hr\tanh^{-1}(Hra)\right], && \text{(7-17)}\\
\zeta_N &= \frac{m\left[-ra_\tau - 2H^2r^2a^3\tanh^{-1}(Hra) + 2Hra^2 + 2a\tanh^{-1}(Hra)\right]}{a^2\left(H^2r^2a^2-1\right)}. && \text{(7-18)}
\end{aligned}
$$

After substituting eq.(7-4,7-5) and eq.(7-17,7-18) in the gauge transformations in eq.(7-12) and eq.(7-14) we finally obtain the perturbations in the Newton gauge

$$
\begin{aligned}
\Psi_N &= \psi - \partial_\tau\zeta_N - \frac{a_\tau}{a}\zeta_N = -\frac{m}{ar}, && \text{(7-19)}\\
\Phi_N &= \phi - \frac{1}{3}\nabla^2\beta_N + \frac{a_\tau}{a}\zeta_N = -\frac{m}{ar}. && \text{(7-20)}
\end{aligned}
$$

Instead of finding the transformation taking to the Newton gauge given in eq.(7-17,7-18) we could have also computed the Bardeen's potentials [62] directly from eqs.(7-4-7-7)

$$\Psi_B = \psi - \frac{1}{a}\left[a\left(\frac{\chi_\tau}{2} - \omega\right)\right]_\tau \quad = -\tfrac{m}{ar}, \tag{7-21}$$

$$\Phi_B = \phi + \frac{1}{6}\nabla^2\chi - \frac{a_\tau}{a}\left(\omega - \frac{\chi_\tau}{2}\right) \quad = -\tfrac{m}{ar}\,. \tag{7-22}$$

As expected the Bardeen's potentials reduce to the Newton gauge potentials obtained in eq.(7-20) and eq.(7-19), and the metric takes the form

$$ds^2 \;=\; a^2\left[\left(1 - \frac{2m}{ar}\right)d\tau^2 - \left(1 + \frac{2m}{ar}\right)\left(dr^2 + r^2 d\Omega^2\right)\right]. \tag{7-23}$$

The metric above is the weak field limit of the McVittie solutions, and an exact coordinate transformation from the SDS metric in static coordinates to the McVittie solution is known. We can deduce that the combination of the radial coordinate transformation $R = a\,r$ and the gauge transformation given in eq.(7-17,7-18) is the weak field limit of such an exact coordinate transformation. This confirms that our method is correct since we have independently obtained the relation between the two metrics.

For solutions where an exact coordinate transformation is unknown, the method we developed has the advantage of allowing to write an SSS metric as a perturbed FRW solution even in the absence of an exact coordinate transformation.

8 Weak field limit of SSS metrics as perturbations of FLRW

In a modified gravity theory (MGT), the spherically symmetric vacuum solution associated with a point mass may differ from the SDS metric, and we could make an ansatz with a de Sitter background of this type

$$ds^2 \;=\; \left(1-mh_t(R)-H^2R^2\right)dT^2-\left(1-mh_r(R)-H^2R^2\right)^{-1}dR^2-R^2d\Omega^2\,, \tag{8-1}$$

where we are not assuming anymore that $g_{tt}=g_{rr}^{-1}$ because in an MGT, the field equations may not imply this relation under the assumption of spherical symmetry. In a generic MGT, spherical symmetry may also not imply that, as in GR, $\partial_t g_{tt}=\partial_t g_{rr}=0$, but here we will only consider solutions that can be written in static coordinates. We will not assume any specific MGT and adopt a purely phenomenological approach to obtain the Newtonian gauge form of these SSS metrics. These can then be used to test them with observational data, and only after the metrics compatible with observations have been identified could we try to find which MGT they are solutions of.

After applying to eq.(8-1) the coordinate transformations given in eq.(6-9) and eq.(6-10), far from the Schwarzschild horizon, i.e. assuming $m \ll R$, we get

$$\begin{aligned}
ds^2 = a^2 \Bigg\{ & \frac{H^6r^6a^6-H^4r^4a^4[mh_r(ra)+3]-1+mh_t(ra)}{\left(H^2r^2a^2-1\right)^3}d\tau^2 \\
& + \frac{H^2r^2a^2\left[m^2h_r(ra)^2+mh_r(ra)-mh_t(ra)\right]+3H^2r^2a^2}{\left(H^2r^2a^2-1\right)^3}d\tau^2 \\
& - \left[1+\frac{mh_r(ra)\left(H^2r^2a^2-mh_r(ra)-1\right)+H^2mr^2a^2\left(H^2r^2a^2-1\right)h_t(ra)}{\left(H^2r^2a^2-1\right)^3}\right]dr^2 \\
& - \frac{2Hmra\left[h_r(ra)\left(H^2r^2a^2-mh_r(ra)-1\right)+\left(H^2r^2a^2-1\right)h_t(ra)\right]}{\left(H^2r^2a^2-1\right)^3}d\tau dr - r^2d\Omega^2 \Bigg\}\,.
\end{aligned} \tag{8-2}$$

Comparing the metrics in eq.(8-2) and eq.(4-28) we can identify the perturbation variables in the case of spherical symmetry as

$$\begin{aligned}
\psi &= \frac{H^2r^2a^2m\left[h_r(ra)\left(-H^2r^2a^2+mh_r(ra)+1\right)-h_t(ra)\right]+mh_t(ra)}{2\left(H^2r^2a^2-1\right)^3}\,, && \text{(8-3)}\\
\phi &= \frac{m^2h_r(ra)^2-m\left(H^2r^2a^2-1\right)\left[H^2r^2a^2h_t(ra)+h_r(ra)\right]}{6\left(H^2r^2a^2-1\right)^3}\,, && \text{(8-4)}\\
\mathcal{E} &= \frac{m\left(H^2r^2a^2-1\right)\left[H^2r^2a^2h_t(ra)+h_r(ra)\right]-m^2h_r(ra)^2}{\left(H^2r^2a^2-1\right)^3}\,, && \text{(8-5)}\\
\omega' &= \frac{Hmra\left(H^2r^2a^2-1\right)\left[h_r(ra)+h_t(ra)\right]-Hm^2rah_r(ra)^2}{\left(H^2r^2a^2-1\right)^3}. && \text{(8-6)}
\end{aligned}$$

Solving equation (4-29) and integrating eq.(8-6) we can finally find the perturbations in the general form

$$\begin{aligned}
\omega &= Hma\int\frac{r[h_r(ra)+h_t(ra)]}{\left(H^2r^2a^2-1\right)^2}\,dr, && \text{(8-7)}\\
\chi &= m\int k_1\int\frac{H^2k_2^2a^2h_t(k_2a)+h_r(k_2a)}{k_2\left(H^2k_2^2a^2-1\right)^2}\,dk_2\,dk_1 && \text{(8-8)}\\
&\quad+\frac{1}{2}r^2C+D, && \text{(8-9)}
\end{aligned}$$

where C and D are integration constants. Well behaved perturbations require $C = D = 0$. These can be replaced in eq.(7-21) and eq.(7-22) to obtain the Bardeen's potentials.

For applications such as the study of gravitationally bounded objects, we are interested in regions of space-time far from the cosmological horizon, i.e., $a\,r \ll 1/H$. Under this assumption, the perturbations can be written as

$$\begin{aligned}
\psi &= \frac{1}{2}mh_t(ra)\,, && \text{(8-10)}\\
\phi &= -\frac{1}{6}mh_r(ra)[mh_r(ra)+1]\,, && \text{(8-11)}\\
\omega &= Hma\int r[h_r(ra)+h_t(ra)]\,dr\,, && \text{(8-12)}\\
\chi &= m\int k_1\int\frac{h_r(k_2a)}{k_2}\,dk_2\,dk_1. && \text{(8-13)}
\end{aligned}$$

In this limit, the Bardeen's potentials take the form

$$\Phi_B = \frac{m}{2}\int\frac{h_r(ar)dr}{r}\,, \tag{8-14}$$

$$\Psi_B = -\frac{m}{2}h_t(ar). \tag{8-15}$$

It is easy to check that for $h_t(R) = h_r(R) = 2/R$ the Bardeen's potentials in eq.(8-14) and eq.(8-15) reduce to the SDS Newton gauge perturbations obtained in eqs.(7-20) and (7-19).

As shown above, contrary to the case of general relativity, the two potentials Φ_B and Ψ_B can be different, which is a consequence of the fact that, for a general SSS metric, $h_t(R)$ and $h_r(R)$ can be different. Bardeen's potentials can be used to test these SSS metrics using physical observables, which are more conveniently computed in the framework of cosmological perturbation theory. Once the SSS metrics in agreement with observational data have been identified using both their static coordinates and cosmological perturbations form, it will be possible to search for the modified gravity theories they are solutions to. The advantage of this approach is that it is independent of the modified gravity theory and narrows the search of modified gravity theories to the ones that admit the SSS metric compatible with observational data as solutions.

9 Turn Around Radius in Static Spherically Symmetric Metric

The turnaround radius is the distance from the center of the coordinate system where the gravitational attraction cancels with the universe's expansion and the radial acceleration is zero. If a test particle is placed inside this radius, it will fall inwards due to gravitational collapse, and if it is placed outside, it will drift away due to the universe's accelerated expansion. Therefore, both the radial velocity and acceleration of a test mass must cancel at this radius. This result agrees with the maximum radius of spherical collapse.

In this chapter, the turnaround radius is computed for a general static metric through the formalism of spherical collapse and radial geodesics. This result is applied to the Schwarzschild-de Sitter metric in static coordinates (6-38) and is extended to include non-static metrics. Afterward, the same computation is taken for a perturbed metric in the Newton gauge, but, thanks to the Bardeen potentials, this result is entirely general and gauge independent. Similarly, it is also applied to the Schwarzschild-de Sitter metric matching the result obtained in static coordinates.

9.1 Maximum Spherical Collapse Radius

The turnaround radius is computed under the spherical collapse formalism according to the procedure presented in [75], and [76]. Under this formalism, a spherical overdensity is considered inside a homogeneous and isotropic expanding universe. The gravitational pull created by the overdensity may halt the expansion in a spherical region, collapsing to a point of infinite density. It will not collapse into a singularity; it will stop when all particles have virialized according to:

$$E_k = -\frac{E_p}{2}, \tag{9-1}$$

where E_k and E_p are the kinetic and potential energies, respectively. Both mass and vacuum energy density are present in the spherical region due to the overdensity and the cosmological constant. Due to this, it must follow the Friedmann equation (3-56) with $\Omega = \Omega_m + \Omega_\Lambda$ and the density parameter corresponding to dark energy satisfies the equation $\Omega_\Lambda = \omega\Omega_m$ with

$\omega = 2\pi\rho/\Lambda$:

$$\begin{aligned}\left(\frac{\dot{a}}{a}\right)^2 &= H_0^2\left(\Omega_m + \Omega_\Lambda\right) - \frac{k}{a^2} \\ &= H_0^2\Omega_{m,0}a^{-3}\left(a^3\omega - \kappa a + 1\right),\end{aligned} \tag{9-2}$$

where $\Omega_{m,0}H_0^2\kappa = k$ has been defined. The turnaround radius occurs where $\dot{a}$ is zero:

$$a^3\omega - \kappa a + 1 = 0. \tag{9-3}$$

the minimum value of κ to have a positive real solution for (9-3) must be [77]

$$\kappa_{min} = 3\sqrt[3]{\frac{\omega}{4}}. \tag{9-4}$$

According to this value, the solution of (9-3) is a maximum scale factor:

$$a_{max} = \sqrt[3]{2\omega} = \sqrt[3]{4\pi\rho/\Lambda}. \tag{9-5}$$

Finally, the maximum size of the spherical region corresponding to this scale factor can be computed taking into account the overdensity $\rho = m/V = \frac{3m}{4\pi r^3}$, where r is the comoving radius, while the physical radius is:

$$R_{TA} = a_{max}r = a_{max}\sqrt[3]{\frac{3m}{4\pi\rho}} = \sqrt[3]{4\pi\rho/\Lambda}\sqrt[3]{\frac{3m}{4\pi\rho}} = \sqrt[3]{\frac{3m}{\Lambda}}. \tag{9-6}$$

This limit represents the maximum size a structure can reach before collapsing gravitationally. A similar method to obtain this limit is approached in the following sections.

9.2 Turn Around Radius in Static Coordinates

In general relativity, Birkhoff's theorem guarantees that a spherical symmetric metric will be static [23] and can be written according to (6-24):

$$ds^2 = F(R)dT^2 - \frac{dR^2}{H(R)} + R^2 d\Omega^2, \tag{9-7}$$

where F y H, are different functions in general. The geodesic equations (3-33) describe the motion of a matter particle inside this metric and, due to its symmetry, it's enough to consider only the radial geodesic

$$\frac{d^2R}{ds^2} = \frac{1}{2}H(R)\frac{\partial F(R)}{\partial R}\left(\frac{dT}{ds}\right)^2 - \frac{1}{2H(R)}\frac{\partial H(R)}{\partial R}\left(\frac{dR}{ds}\right)^2, \tag{9-8}$$

this equation determines if the particle falls inward or drifts outwards. According to this, the turnaround radius is the point where the acceleration is zero. However, the radial velocity must also be zero to have the particle fixed at the turnaround radius. This means that $\frac{dR}{ds} = 0$, and the geodesic equation becomes:

$$\frac{d^2R}{ds^2} = \frac{1}{2}H(R)\frac{\partial F(R)}{\partial R}\left(\frac{dT}{ds}\right)^2. \tag{9-9}$$

This implies that to have no radial acceleration, the turn around radius r_{TA} must follow

$$\left.\frac{\partial F}{\partial R}\right|_{R_{TA}} = 0, \tag{9-10}$$

according to this, given a metric, the turnaround radius can be computed by deriving the g_{00} component and solving (9-10) as long as the metric has the same form as (6-24).

In modified gravity theories, spherical symmetry no longer guarantees a static metric. With this in mind, the same computation is carried out for a non-static metric. The ansatz (6-24) is completely general and independent of the gravity theory, but it is no longer static

$$ds^2 = F(T,R)dT^2 - \frac{dR^2}{H(T,R)} + R^2 d\Omega^2, \tag{9-11}$$

where the functions F and H now depend on both T and R. In this case, the radial geodesic is

$$\frac{d^2R}{ds^2} = \frac{1}{2}H(T,R)\frac{\partial F(T,R)}{\partial R}\left(\frac{dT}{ds}\right)^2 - \frac{1}{2H(T,R)}\frac{\partial H(T,R)}{\partial R}\left(\frac{dR}{ds}\right)^2 - \frac{1}{H(T,R)}\frac{\partial H(T,R)}{\partial T}\left(\frac{dT}{ds}\right)\left(\frac{dR}{ds}\right), \tag{9-12}$$

as in the static case, null radial velocity is required $\frac{dR}{ds} = 0$ and a similar result is obtained

$$\frac{d^2R}{ds^2} = \frac{1}{2}H(T,R)\frac{\partial F(T,R)}{\partial R}\left(\frac{dT}{ds}\right)^2, \tag{9-13}$$

it is expected as both metrics have a similar Γ^1_{00} connection coefficient which, according to (3-36), is related to the Newtonian gravitational potential. This result arises from the definition of the Christoffel symbols (3-3), as spherical symmetry allows the metric to be expressed diagonally. From here, the same condition is achieved for the turnaround radius R_{TA}

$$\left.\frac{\partial F}{\partial R}\right|_{R_{TA}} = 0, \tag{9-14}$$

As an example, this result will be applied to the Schwarzschild-de Sitter metric.

9.2.1 SDS Turn Around Radius

The static Schwarzschild-de Sitter metric (6-38) is given by

$$F(R) = H(R) = \left(1 - \frac{2m}{R} - \frac{\Lambda R^2}{3}\right). \tag{9-15}$$

Deriving with respect to the radial coordinate

$$\partial_R F(R) = \left(\frac{2m}{R^2} - 2\frac{\Lambda R}{3}\right). \tag{9-16}$$

According to (9-10) the turnaround radius R_{TA} must be a solution to the equation:

$$\frac{2m}{R_{TA}^2} - \frac{2\Lambda}{3} R_{TA} = 0. \tag{9-17}$$

Therefore, the turnaround radius for the static Schwarzschild-de Sitter metric is

$$R_{TA} = \sqrt[3]{\frac{3m}{\Lambda}}. \tag{9-18}$$

This result agrees with what is expected intuitively due to both opposing effects. A higher mass increases the gravitational pull, which allows even bigger structures. On the other hand, a greater gravitational constant accelerates the universe's expansion, reducing the turnaround radius. The previous computation is completely general and agrees with the one found in [75]. However, it is not always possible to take the metric to the form given by (6-24) required to use the result in (9-10). The turnaround radius will be computed under the theory of cosmological perturbations as a function of the gauge-invariant potentials to generalize this result. However, to compare the results, the Bardeen potentials of the static metric will first be obtained in the following section.

9.3 Gauge Independent Turn Around Radius

To obtain the turnaround radius, a condition similar to the one in (9-10) will be computed using cosmological perturbation theory. In this section, the procedure from [26] is extended to consider time-dependent perturbations. However, the same turnaround radius expression is achieved. Additionally, it is gauge-independent by using the Bardeen potentials. In Newton's gauge, the Bardeen potentials are $A = \Psi$ and $C = -\Phi$, which will ease the computation. To apply this result, the cosmological perturbation Schwarzschild-de Sitter metric (7-23) will be used. In the Newton gauge, the metric can be written as:

$$ds^2 = a^2\left[(1+2\Psi)d\tau^2 - (1-2\Phi)\left(dr^2 + r^2 d\Omega^2\right)\right], \tag{9-19}$$

which is completely general considering the Bardeen potentials. The non-null Christoffel symbols for this metric are given by (4-35), taking into account that the perturbations can be a function of both the radius and time. Therefore, the geodesic equations are

$$\frac{dv^\mu}{ds} + \Gamma^\mu_{00}(v^0)^2 + 2\Gamma^\mu_{01}v^0v^1 + \Gamma^\mu_{11}(v^1)^2 = 0. \tag{9-20}$$

For a radially moving particle, the four-velocity is:

$$v^\mu = (v^0, v^1, 0, 0). \tag{9-21}$$

However, only the first two geodesic equations are needed:

$$\frac{dv^0}{ds} + \left(\frac{a'}{a} + \Psi'\right)(v^0)^2 + 2\partial_r\Psi v^0 v^1 + \left[\frac{a'}{a}(1 + 2\Phi - 2\Psi) + \Phi'\right](v^1)^2 = 0, \tag{9-22}$$

$$\frac{dv^1}{ds} + \partial_r\Psi(v^0)^2 + 2\left(\frac{a'}{a} + \Phi'\right)v^0 v^1 + \partial_r\Phi(v^1)^2 = 0, \tag{9-23}$$

where the prime ($'$) is a derivative with respect to conformal time τ. On the other hand, the physical radius is defined as $R = ar$, and its derivatives with respect to the cosmological time in terms of the comoving radius r are:

$$\frac{dR}{dt} = \dot{a}r + a\dot{r}, \tag{9-24}$$

$$\frac{d^2R}{dt^2} = \ddot{a}r + 2\dot{a}\dot{r} + a\ddot{r}, \tag{9-25}$$

where the dot ($\dot{}$) corresponds to a derivative with respect to cosmological time t. These derivatives can be simplified considering the following relations:

$$\dot{r} = \frac{dr}{dt} = \frac{dr}{d\tau}\frac{d\tau}{dt} = \frac{1}{a}\frac{dr}{ds}\frac{ds}{d\tau} = \frac{v^1}{av^0}, \tag{9-26}$$

$$\ddot{r} = \frac{d}{dt}\left(\frac{v^1}{av^0}\right) = -\frac{\dot{a}}{a^2}\frac{v^1}{v^0} + \frac{1}{a^2v^0}\frac{d}{ds}\left(\frac{v^1}{v^0}\right). \tag{9-27}$$

Substituting in (9-25):

$$\begin{aligned} \frac{d^2R}{dt^2} &= \ddot{a}r + 2\dot{a}\frac{v^1}{av^0} + a\left[-\frac{\dot{a}}{a^2}\frac{v^1}{v^0} + \frac{1}{a^2v^0}\frac{d}{ds}\left(\frac{v^1}{v^0}\right)\right] \\ &= \ddot{a}r + \dot{a}\frac{v^1}{av^0} + \frac{1}{av^0}\left[\frac{1}{v^0}\frac{dv^1}{ds} - \frac{v^1}{(v^0)^2}\frac{dv^0}{ds}\right]. \end{aligned} \tag{9-28}$$

Similar to the computation in static coordinates, the turnaround radius is the distance where both the radial velocity and acceleration are zero:

$$\frac{d^2R}{dt^2} = 0. \tag{9-29}$$

$$\frac{dR}{dt} = 0, \tag{9-30}$$

Additionally, the four-velocity can be expressed perturbatively such that it can be considered at rest at zeroth order:

$$v^\mu = v_0^\mu + \delta v^\mu = (1/a, 0, 0, 0) + \delta v^\mu, \tag{9-31}$$

this velocity is replaced in both the turnaround condition (9-29) and the geodesic equation (9-23) up to linear order

$$\ddot{a}r + 2\dot{a}\delta v^1 + a\frac{d\delta v^1}{ds} = 0, \tag{9-32}$$

$$\frac{d\delta v^1}{ds}+\frac{\partial_r\Psi}{a^2}+2\left(\frac{a'}{a}+\Phi'\right)\frac{\delta v^1}{a}=0. \tag{9-33}$$

Finally, considering that $\dot{a}=\frac{da}{dt}=\frac{da}{d\tau}\frac{d\tau}{dt}=\frac{a'}{a}$, it is substituted in (9-33) and (9-32):

$$\begin{aligned}\ddot{a}r+2\dot{a}\delta v^1+a\left[-\frac{\partial_r\Psi}{a^2}-2\left(\frac{a'}{a}+\Phi'\right)\frac{\delta v^1}{a}\right]&=0,\\ \ddot{a}r+2\dot{a}\delta v^1-\frac{\partial_r\Psi}{a}-2\frac{a'}{a}\delta v^1-2\Phi'\delta v^1&=0,\\ \ddot{a}r+2\dot{a}\delta v^1-\frac{\partial_r\Psi}{a}-2\dot{a}\delta v^1-2\Phi'\delta v^1&=0,\\ \ddot{a}r-\frac{\partial_r\Psi}{a}-2\Phi'\delta v^1&=0.\end{aligned} \tag{9-34}$$

Considering a null radial velocity, the turnaround radius must follow the condition

$$\ddot{a}r-\frac{\partial_r\Psi}{a}=0, \tag{9-35}$$

where once again the dot ($\dot{}$) denotes a cosmological time (t) derivative. This is the same result found in [26] but for non-static metrics. The result is again independent of the static nature of the metric, which is probably due to the spherical symmetry. However, this method does not rely on having a metric of the form (6-24) which makes this result much more general than the previously computed. Knowing the Bardeen potentials, specifically Ψ, the turnaround radius can be computed using equation (9-35). This can be achieved in any gauge according to (4-18).

9.3.1 SDS Turn Around Radius

The cosmological perturbation Schwarzschild-de Sitter metric (7-23) has Bardeen potentials $\Psi = \Phi = -\frac{m}{ar}$, where the integration constant D has been ignored. The turnaround radius can be computed by deriving Ψ with respect to r

$$\partial_r \Psi = \frac{m}{ar^2} \tag{9-36}$$

The turnaround radius is a solution to (9-35):

$$\ddot{a}r - \frac{\partial_r \Psi}{a} = \ddot{a}r - \frac{m}{r^2 a^2} = 0. \tag{9-37}$$

In this case, the following turnaround radius is obtained:

$$r_{TA} = \sqrt[3]{\frac{m}{\ddot{a}a^2}}, \tag{9-38}$$

where $a = e^{t/l}$ is the de Sitter scale factor. Therefore, the comoving turn around radius is

$$r_{TA} = e^{-t/l}\sqrt[3]{ml^2}. \tag{9-39}$$

Going back to the physical coordinates according to (4-3) the physical turnaround radius is

$$R_{TA} = e^{t/l} r_{TA} = \sqrt[3]{ml^2} = \sqrt[3]{3m/\Lambda}. \tag{9-40}$$

This result matches exactly the one obtained in a similar way for static coordinates (9-18). However, this formalism can be applied to any cosmological perturbation metric by computing the Bardeen potentials.

In this chapter, the turnaround radius was computed under three different methods: spherical collapse, radial geodesics of the static metric, and the cosmological perturbation metric. All of the results are consistent for the Schwarzschild-de Sitter metric, with a turnaround radius of $R_{TA} = \sqrt[3]{\frac{3m}{\Lambda}}$.

9.4 Gauge invariant computation of the turnaround radius for SSS metrics

The advantage of the gauge-invariant definition given in eq.(9-35) is that we can obtain the turnaround radius from the metric of cosmological perturbations in any gauge. For example, starting from the SDS metric written in a gauge different from the Newton gauge, such as in eq.(7-3), we could compute the Bardeen's potentials defined in eq.(7-22) and eq.(7-21), and then solve eq.(9-35).

The equivalence between eq.(9-10) and eq.(9-35) can be shown for example for the class of SSS metric in eq.(8-1) for which

$$F(R) = 1 - mh_t(R) - H^2R^2 \,, \tag{9-41}$$

and for which the corresponding Bardeen's potential Ψ_B is given eq.(8-15).

Combining eq.(8-15) and eq.(9-35) we get the general gauge invariant condition for the turn around radius

$$2H^2R + mh_t'(R) = 0 \tag{9-42}$$

which is in agreement with eq.(9-10).

We can apply this method for example to the SDS metric, corresponding to $h_t = 2/R$, for which eq.(9-42) takes the form

$$2H^2R - 2\frac{m}{R^2} = 0, \tag{9-43}$$

which gives the solution

$$R_{TA} = \sqrt[3]{\frac{m}{H^2}} \tag{9-44}$$

in agreement with the result obtained in static coordinates.

9.5 Newton gauge form for different SSS metrics

9.5.1 Brans-Dicke Theory

In Brans-Dicke (BD) theory, the Jebsen-Birkhoff theorem [78] is valid if the scalar field is time-independent. Consequently, under the assumption of a static scalar field, the static ansatz for the metric adopted in [25] should also give the most general spherically symmetric solution. Applying a perturbative approach the solution of the field equations for the Brans-Dicke theory can be written as [79]

$$ds^2 = \left[1 - (1+\epsilon)\frac{2m}{R} - (1-2\epsilon)H^2R^2\right]dt^2 - \left[1 - (1-\epsilon)\frac{2m}{R} - (1-4\epsilon)H^2R^2\right]dR^2 - R^2d\Omega^2 \,, \tag{9-45}$$

where $\epsilon = \frac{1}{2\omega_{BD}+3}$ and ω_{BD} is the Brans-Dicke scalar field's coupling constant [80]. This solution reduces to SDS assuming the observer is far from the cosmological horizon ($R \ll 1/H$) in the limit $\epsilon \to 0$, which is also the limit in which the BD theory reduces to GR.

Applying the coordinate transformation given in eq.(6-9) and eq.(6-10) and using conformal time $dt = a\,d\tau$ the metric in eq.(9-45) takes the form

$$\begin{aligned} ds^2 = a^2 \Bigg[&\left(1 - \frac{2m(1+\epsilon)}{ar} + 2\epsilon H^2r^2a^2\right)\tau^2 - \left(1 - \frac{2m(1+\epsilon)}{ar} - 4\epsilon H^2r^2a^2\right)dr^2 \\ &-8Hm\,d\tau dr - r^2d\Omega^2\Big] \,. \end{aligned} \tag{9-46}$$

Comparing with equation (4-28) and integrating eq.(4-29) we get

$$\psi = \frac{\epsilon H^2 a^3 r^3 - m(1+\epsilon)}{ar}, \tag{9-47}$$

$$\phi = \frac{2\epsilon H^2 a^3 r^3 - m(1-\epsilon)}{3ar}, \tag{9-48}$$

$$\omega = 4Hmr, \tag{9-49}$$

$$\chi = -\frac{2mr(1-\epsilon)}{a} - \frac{\epsilon}{2} H a^2 r^4. \tag{9-50}$$

From eq.(7-16) we can find the transformation to go to the Newton Gauge gauge, defined by

$$\beta_N = -\frac{mr(1-\epsilon)}{a} - \frac{\epsilon}{4} H a^2 r^4, \tag{9-51}$$

$$\zeta_N = -Hmr(3+\epsilon) - \frac{\epsilon}{2} H^3 r^4 a^3. \tag{9-52}$$

After substituting eqs.(9-47-9-48) and eqs.(9-51-9-52) in the gauge transformations in eq.(7-12) and eq.(7-14) we finally obtain the perturbations in the Newton gauge

$$\Psi_N = \psi - \partial_\tau \zeta_N - \frac{a_\tau}{a} \zeta_N = H^2 R^2 \epsilon - \frac{m(1+\epsilon)}{R}, \tag{9-53}$$

$$\Phi_N = \phi - \frac{1}{3} \nabla^2 \beta_N + \frac{a_\tau}{a} \zeta_N = -H^2 R^2 \epsilon - \frac{m(1-\epsilon)}{R}, \tag{9-54}$$

where $R = a\,r$. Alternatively, we can obtain the same result without computing any gauge transformation, taking advantage of the gauge invariance of the Bardeen's potentials, substituting in eq.(7-21) and eq.(7-22) the perturbations obtained in eq.(9-47-9-50), getting again

$$\Psi_B = H^2 R^2 \epsilon - \frac{m(1+\epsilon)}{R}, \tag{9-55}$$

$$\Phi_B = -H^2 R^2 \epsilon - \frac{m(1-\epsilon)}{R}, \tag{9-56}$$

which coincide with the Newton gauge result as expected due to the gauge invariance of Ψ_B and Φ_B.

The same result can also be obtained from eq.(8-14) and eq.(8-15) with $h_t = 2(1+\epsilon)/R - 2\epsilon H^2 R^2/m$ and $h_r = 2(1-\epsilon)/R - 4\epsilon H^2 R^2/m$. The potentials reduce to the GR result $\Phi_N = \Psi_N = -\frac{m}{ar}$ in eq.(7-19,7-20) when $\epsilon \to 0$.

From the Bardeen's potential computed in eq.(9-55) we get the turnaround radius

$$r_{TA} = \frac{1+\epsilon}{a} \sqrt[3]{\frac{m}{H^2}}, \tag{9-57}$$

which corresponds to the physical radius

$$R_{TA} = a r_{TA} = \sqrt[3]{\frac{m}{H^2}} (1+\epsilon), \tag{9-58}$$

in agreement with [25].

In general relativity, the absence of anisotropic pressure perturbations in the vacuum implies that $\Phi_N = \Psi_N$ while in BD theory, the field equations do not imply this anymore, and they can be different. Note we have recovered, far from the cosmological horizon, the metric computed in [25] solving the perturbation equations in the Newton gauge. This explicitly shows the coordinate transformation between the solution in static and comoving coordinates and that the solutions are indeed the same. The advantage of this approach is that it allows deriving the metric as a Newton gauge perturbation of the FLRW solution directly from the metric in static coordinates, without the need to solve the perturbed field equations again as it was done in [25].

9.5.2 Power law modifications of the de Sitter metric

Flat rotational curves can be explained by a metric with a power law dependence in the radius [81] as seen in the final section of this chapter. This is the motivation for studying more general power law modifications. Let's consider the sub-class of SSS metrics given in eq.(8-1) corresponding to this choice of h_t, h_r

$$h_t(R) = \lambda_1 R^{n_1}\,, \tag{9-59}$$

$$h_r(R) = \lambda_2 R^{n_2}. \tag{9-60}$$

Following the same procedure shown in the previous section, we first identify the perturbations in the spherically symmetric form given in eq.(4-28)

$$\phi = -\frac{1}{6}\left[m\lambda_2(ra)^n_2 + m^2\lambda_2^2(ra)^{2n_2}\right]\,, \tag{9-61}$$

$$\psi = -\frac{1}{2}m\lambda_1(ra)^{n_1}\,, \tag{9-62}$$

$$\omega = Hmar^2\left[\frac{\lambda_1(ar)^{n_1}}{2+n_1} + \frac{\lambda_2(ar)^{n_2}}{2+n_2}\right]\,, \tag{9-63}$$

$$\chi = \frac{\lambda_2 m r^2(ar)^{n_2}\left(\frac{\lambda_2 m(ra)^{n_2}}{n_2+1} + \frac{4}{n_2+2}\right)}{4n_2}\,. \tag{9-64}$$

We can then compute the Bardeen's potentials in the region $m \ll R \ll 1/H$

$$\Psi_B = -\frac{m\lambda_1(ra)^{n_1}}{2}, \tag{9-65}$$

$$\Phi_B = \frac{m\lambda_2(ra)^{n_2}}{2n_2}. \tag{9-66}$$

The difference between the Ψ and Φ is due to the difference between g_{tt} and g_{rr}^{-1} in static coordinates, and it could arise in vacuum solutions of modified gravity theories admitting this SSS solution.

The turnaround radius in comoving coordinates is given by

$$r_{TA} = \frac{1}{a}\left(-\frac{m\lambda_1 n_1}{2H^2}\right)^{\frac{1}{2-n_1}}\,, \tag{9-67}$$

while in static coordinates it is

$$R_{TA} = \left(-\frac{m\lambda_1 n_1}{2H^2}\right)^{\frac{1}{2-n_1}}, \tag{9-68}$$

which reduces to eq.(9-40) when $\lambda_1 = 2$ and $n_1 = -1$.

9.5.3 Exponential modifications of the de Sitter metric

Exponential modifications could be interpreted as a possible large-scale extension of the power law (i.e. power law could be considered the leading order term of the exponential), but we didn't investigate this in the thesis. For the sub-class of SSS metrics given in eq.(8-1) corresponding to this choice of h_t, h_r

$$h_t(R) = \lambda_1 e^{b_1 R}, \tag{9-69}$$

$$h_r(R) = \lambda_2 e^{b_2 R}, \tag{9-70}$$

for the metric perturbations we get

$$\phi = -\frac{m\lambda_2 e^{b_2 ra} + m^2\lambda_2^2 e^{2b_2 ra}}{6}, \tag{9-71}$$

$$\psi = -\frac{m\lambda_1 e^{b_1 ra}}{2}, \tag{9-72}$$

$$\omega = \frac{Hm\left[b_1^2\lambda_2 e^{b_2 ra}(b_2 ra-1) + b_2^2\lambda_1 e^{b_1 ra}(b_1 ra-1)\right]}{2b_1^2 b_2^2 a}, \tag{9-73}$$

$$\chi = \frac{\lambda_2^2 m^2 e^{2b_2 ra}}{8b_2^2 a^2} + \frac{\lambda_2 m e^{b_2 ra}}{2b_2^2 a^2} + \frac{1}{2}\lambda_2^2 m^2 r^2 \mathrm{Ei}(2b_2 ra) + \frac{1}{2}\lambda_2 m r^2 \mathrm{Ei}(b_2 ra) \tag{9-74}$$

$$- \frac{\lambda_2^2 m^2 r e^{2b_2 ra}}{4b_2 a} - \frac{\lambda_2 m r e^{b_2 ra}}{2b_2 a}, \tag{9-75}$$

where $Ei(z)$ is the exponential integral function defined as

$$Ei(z) = -\int_{-z}^{\infty} \frac{e^{-t}}{t} dt. \tag{9-76}$$

The corresponding Bardeen's potentials are

$$\Psi_B = -\frac{1}{2}\lambda_1 m e^{b_1 ra}, \tag{9-77}$$

$$\Phi_B = \frac{1}{2}\lambda_2 m \mathrm{Ei}(b_2 ra). \tag{9-78}$$

Note that in the above expressions we are only giving the leading order terms in the region $m \ll R \ll 1/H$.

9.5.4 Logarithmic modifications of the de Sitter metric

Logarithmic modifications are studied from a mathematical point of view without any specific physical motivation. In the sub-class of SSS metrics given in eq.(8-1) corresponding to this choice of h_t, h_r

$$\begin{aligned} h_t(R) &= \lambda_1 \log b_1 R\,, \qquad (9\text{-}79)\\ h_r(R) &= \lambda_2 \log b_2 R, \qquad (9\text{-}80) \end{aligned}$$

the cosmological perturbations are

$$\begin{aligned} \phi &= -\frac{m\lambda_2 \log(arb_2) + m^2\lambda_2^2[\log(arb_2)]^2}{6}, \qquad (9\text{-}81)\\ \psi &= -\frac{m\lambda_1 \log(arb_1)}{2}, \qquad (9\text{-}82)\\ \omega &= \frac{1}{4}Hmr^2a[2\lambda_1\log(b_1ra) + 2\lambda_2\log(b_2ra) - \lambda_1 - \lambda_2], \qquad (9\text{-}83)\\ \chi &= \frac{1}{6}\lambda_2^2m^2r^2\log^3(b_2ra) - \frac{1}{4}\lambda_2^2m^2r^2\log^2(b_2ra) + \frac{1}{4}\lambda_2^2m^2r^2\log(b_2ra) \qquad (9\text{-}84)\\ &+ \frac{1}{4}\lambda_2mr^2\log^2(b_2ra) - \frac{1}{4}\lambda_2mr^2\log(b_2ra) - \frac{1}{8}\lambda_2^2m^2r^2 + \frac{1}{8}\lambda_2mr^2. \qquad (9\text{-}85) \end{aligned}$$

and the corresponding Bardeen's potentials far away from the horizons ($m \ll R \ll 1/H$) are

$$\begin{aligned} \Psi_B &= -\frac{1}{2}\lambda_1 m\log(b_1ra)\,, \qquad (9\text{-}86)\\ \Phi_B &= \frac{1}{4}\lambda_2 m\left[\log(b_2ra)\right]^2. \qquad (9\text{-}87) \end{aligned}$$

The turnaround radius can be calculated analytically by solving eq.(9-10), obtaining

$$r_{TA} = \frac{1}{Ha}\sqrt{\frac{m\lambda_1}{2}}\,, \qquad (9\text{-}88)$$

which in static coordinates gives

$$R_{TA} = \frac{1}{H}\sqrt{\frac{m\lambda_1}{2}}. \qquad (9\text{-}89)$$

9.6 SSS metrics giving flat rotation curves

The SSS metric[81] which gives flat rotation curves is

$$ds^2 = \left(\frac{R}{R_c}\right)^{2v^2} dt^2 - \left[1 - v^2 f(R) - H^2R^2\right] dR^2 - R^2 d\Omega^2. \qquad (9\text{-}90)$$

Applying the coordinate transformation given in eq.(6-9) and eq.(6-10) and using conformal time, in the low tangential velocity regime and far from the cosmological horizon ($v \ll 1, R \ll 1/H$), the metric takes the following form

$$\begin{aligned} ds^2 = a^2 \Bigg\{ & \left[1 + H^2 r^2 a^2 + 2v^2 \log \frac{ar}{R_c}\right] d\tau^2 - \left[1 - 2H^2 r^2 a^2 - v^2 f(ar)\right] dr^2 \\ & - \left[6H^3 r^3 a^3 + 2Hrv^2 a \left(f(ar) + 2\log\frac{ar}{R_c}\right)\right] dr d\tau - r^2 d\Omega^2 \Bigg\} . \end{aligned} \tag{9-91}$$

Comparing with equation (4-28) and integrating eq.(4-29) we get

$$\psi = \frac{H^2 r^2 a^2}{2} + v^2 \log\left(\frac{ar}{R_c}\right) , \tag{9-92}$$

$$\phi = \frac{1}{3} H^2 r^2 a^2 + \frac{v^2}{6} f(ar) , \tag{9-93}$$

$$\omega = \frac{1}{2}\int_0^r \left\{ -2Hrv^2 a \left[f(ra) + 2\log\left(\frac{ra}{R_c}\right)\right] - 6H^3 r^3 a^3 \right\} dr , \tag{9-94}$$

$$\chi = \int_0^r k_1 \int_0^{k_1} \left(-\frac{v^2 f(k_2 a)}{k_2} - 2H^2 k_2 a^2 \right) dk_2\, dk_1 . \tag{9-95}$$

We can then compute the Bardeen's potential by substituting eqs.(9-92-9-95) in eq.(7-21)

$$\Psi_B = v^2 \log\left(\frac{R}{R_c}\right) - \frac{1}{2} H^2 R^2. \tag{9-96}$$

This agrees with the results obtained in [81] with an additional term due to the cosmological constant.

To better understand this solution we can compute the radial energy density profile using Einstein's equation ${G^0}_0 = 8\pi {T^0}_0 = 8\pi\rho$

$$8\pi\rho = {G^0}_0 = 3H^2 + 2\nabla^2\Phi - 6H\Phi' = \frac{2v^2}{a^2 r^2} - 6H^2. \tag{9-97}$$

In terms of the physical radius $R = a\, r$ we get

$$\rho(R) = \frac{2v^2}{8\pi R^2} - \frac{3H^2}{4\pi} , \tag{9-98}$$

and assuming flatness the total energy contained inside a sphere of radius R is obtained by integrating the density ρ

$$M(R) = \int_0^R 4\pi R'^2 \rho(R') dR' = \int_0^R \left(v^2 - 3H^2 R'^2\right) dR' = v^2 R - H^2 R^3. \tag{9-99}$$

We have obtained the expected linear behavior as in [81] with an additional cosmological constant term. This confirms that the method we have used to re-write the SSS solution in eq.(9-90) as a perturbed FRW metric is giving correct results.

10 Gravitational Stability Mass in scalar-tensor theories

We will focus on the class of scalar-tensor theories defined by the action in [82]:

$$\mathcal{S} = \int d^4x\sqrt{-g}\left[\frac{1}{2}f(\mathcal{R},\phi,X) - 2\Lambda + \mathcal{L}_m\right], \tag{10-1}$$

where Λ is the bare cosmological constant, ϕ is a scalar field, and $X = -\frac{1}{2}\partial_\mu\phi\partial^\mu\phi$ is the scalar field's kinetic term, and we used a system of units in which $c = 1$.

For non-relativistic matter with energy-momentum tensor

$$\delta T^0_0 = \delta\rho_m,\ \delta T^0_i = -\rho_m v_{m,i}, \tag{10-2}$$

where v_m is the matter velocity potential, and using the metric for scalar perturbations in the Newton gauge

$$ds^2 = -(1+2\Psi)dt^2 + a^2(1-2\Phi)\delta_{ij}dx^i dx^j, \tag{10-3}$$

the Fourier's transform of the Einstein's equations give the modified Poisson equation [82]

$$\Psi_k = -4\pi\tilde{G}_{eff}\frac{a^2}{k^2}\rho_m\delta_k, \tag{10-4}$$

where k is the comoving wave number, the subscript k denotes the corresponding Fourier modes, and δ_k is the gauge-invariant matter density contrast. The quantity $\tilde{G}_{eff}$, normally interpreted as the effective gravitational "constant", is given by [82]

$$\tilde{G}_{eff} = \frac{1}{8\pi F}\frac{f_{,X} + 4\left(f_{,X}\frac{k^2}{a^2}\frac{F_{,R}}{F} + \frac{F^2_{,\phi}}{F}\right)}{f_{,X} + 3\left(f_{,X}\frac{k^2}{a^2}\frac{F_{,R}}{F} + \frac{F^2_{,\phi}}{F}\right)}, \tag{10-5}$$

where $F = \frac{\partial f}{\partial\mathcal{R}}$.

10.1 Gravitational stability mass

According to [83] and [26] the turnaround radius can be computed from the gauge-invariant Bardeen potentials by solving the equation

$$\ddot{a}r - \frac{\Psi'}{a} = 0, \tag{10-6}$$

where the dot and the prime denote derivatives with respect to time and the radial coordinate, respectively. Note that the above condition is independent of the gravity theory since it is only based on the use of the metric of cosmological perturbations in the Newton gauge, and *it does not* assume any gravitational field equation. We can take advantage of the generality of eq.(10-6) and apply it to any gravity theory, in particular to the theories defined in eq.(10-1).

For the theories we will consider, and in the sub-horizon limit, we can then take the inverse Fourier's transform of eq.(10-4) to get a real space modified Poisson's equation of the form

$$\Delta\Psi = -4\pi G_{eff}\rho_m\delta\,. \tag{10-7}$$

The gravitational potential outside a spherically symmetric object of mass m is then obtained by integrating the modified Poisson's equation (10-7)

$$\Psi = -\frac{G_{eff}m}{r}, \tag{10-8}$$

which substituted in eq.(10-6) allows deriving a general expression for the turnaround radius for all the scalar-tensor theories defined in eq.(10-1)

$$r_{TA} = \sqrt[3]{\frac{3G_{eff}m}{\Lambda}}\,. \tag{10-9}$$

It is convenient to define the ratio between the Newton constant G and the effective gravitational constant as $\Delta = G/G_{eff}$ and the gravitational stability mass (GSM) as:

$$m_{gs} = \frac{\Lambda r_{obs}^3}{3G_{eff}} = m_{GR}\Delta\,, \tag{10-10}$$

where $m_{GR}(r_{obs}) = \Lambda r_{obs}^3/3G$ is the value of the GSM predicted by GR. Any object of mass m_{obs} should have a radius $r_{obs} < r_{TA}(m_{obs})$, or viceversa any gravitational bounded object of radius r_{obs} should have a mass larger than m_{gs}

$$m_{obs}(r_{obs}) > m_{gs}(r_{obs}) = \frac{\Lambda r_{obs}^3}{3G_{eff}} = m_{GR}(r_{obs})\Delta\,. \tag{10-11}$$

In fact objects of size r_{obs} with a mass smaller than $m_{gs}(r_{obs})$ would not be gravitationally stable, since the effective force is due to dark energy will dominate the attractive gravitational force.

In order to compare theories to experiments, it is crucial to establish the size of gravitationally bounded structures, and for this purpose, the caustic method has been developed [84], showing good accuracy when applied to simulated data. In the rest of this work, we will use this method to set constraints on the parameters of the different MGT.

Galaxy clusters data [85, 86] can be used to set upper bounds on GSM, and to consequently set constraints on G_{eff}, since from eq.(10-11) we get

$$\Delta < \frac{m_{obs}}{m_{GR}}\,. \tag{10-12}$$

10.2 Gravity theory independent constraints

Before considering the constraints on specific gravity theories in the following sections, we can derive some general gravity theory independent constraints for G_{eff}. Note that since the GSM only gives a lower bound for the mass of an object of a given radius, we cannot fit the data points one by one, since each different gravity theory predicts a range of masses $m > m_{gs}(r_{obs})$, not a single value. Consequently, most constraints come from the objects with the lowest mass to size ratio. Most of the data are consistent with GR, except few data points corresponding to the galaxy clusters A655, A1413 and NGC5353/4, which give respectively $\Delta < 0.9162 \pm 0.2812$, $\Delta < 0.9723 \pm 0.0151$ and $\Delta < 0.0969^{+0.3215}_{-0.0178}$, as shown in fig.(**10-1-10-2**).

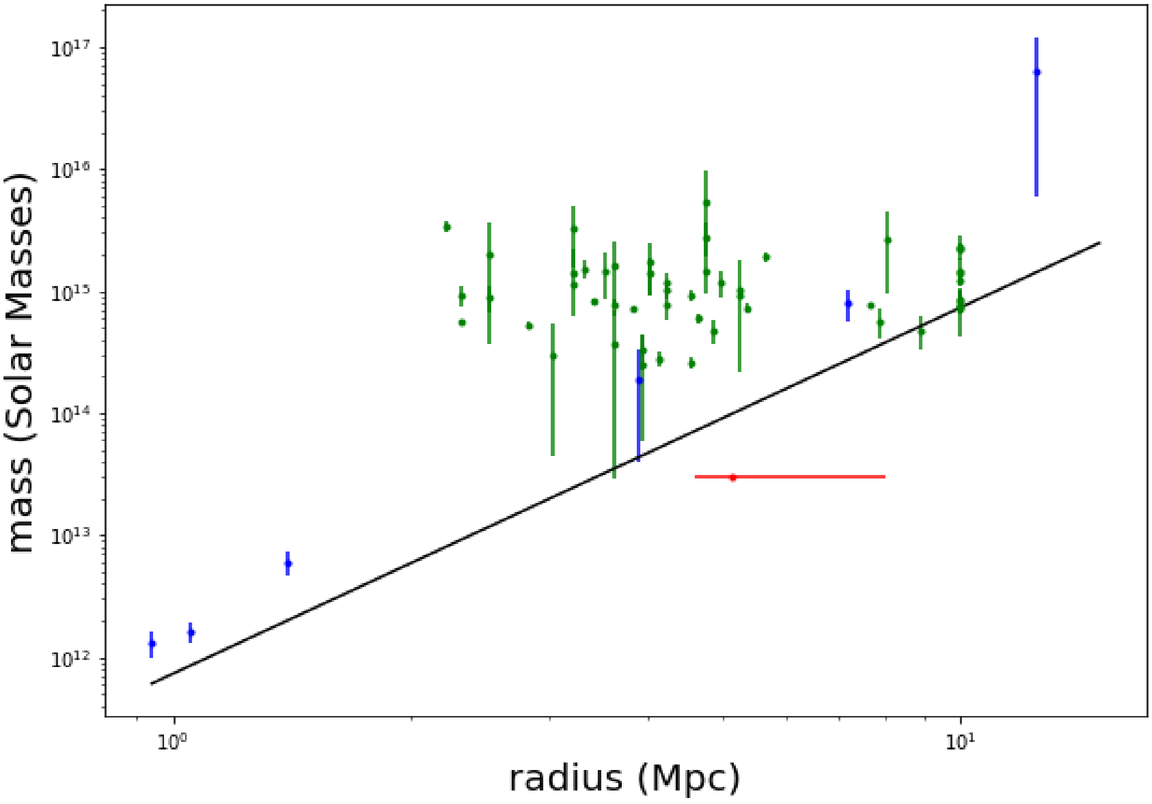

Figure 10-1: Observed masses and radii of galaxy clusters are compared to the GR prediction (black line). Vertical green lines represent the errors on the estimation of the masses from [86] and blue lines correspond to other cosmological structures in [75]. The object with the most significant deviation is NGC5353/4 plotted in red [85], which is shown in more detail in fig.(**10-2**).

The errors have been obtained by Gaussian propagation from the errors on m_{obs} corresponding to r_{MAX} in [86] for A655 and A1413, and from the probability distribution for the size of NGC5353/4 in [85] using the normalization relation

$$\int \rho_r(r)dr = \int \rho_\Delta[\Delta(r)]d\Delta = 1 \tag{10-13}$$

where ρ_r and ρ_Δ are the probability density functions of the size r and Δ respectively. The lower and upper bound are taken from the symmetric two-tail limits on the distribution and the main value is taken as the maximum likelihood estimate for Δ. The tightest constraints for GR come from A1413 and NGC5353/4, whose deviation from GR is respectively of order $1.84\,\sigma$ and $2.61\,\sigma$, implying that there is not very strong evidence of the need for a modification of GR.

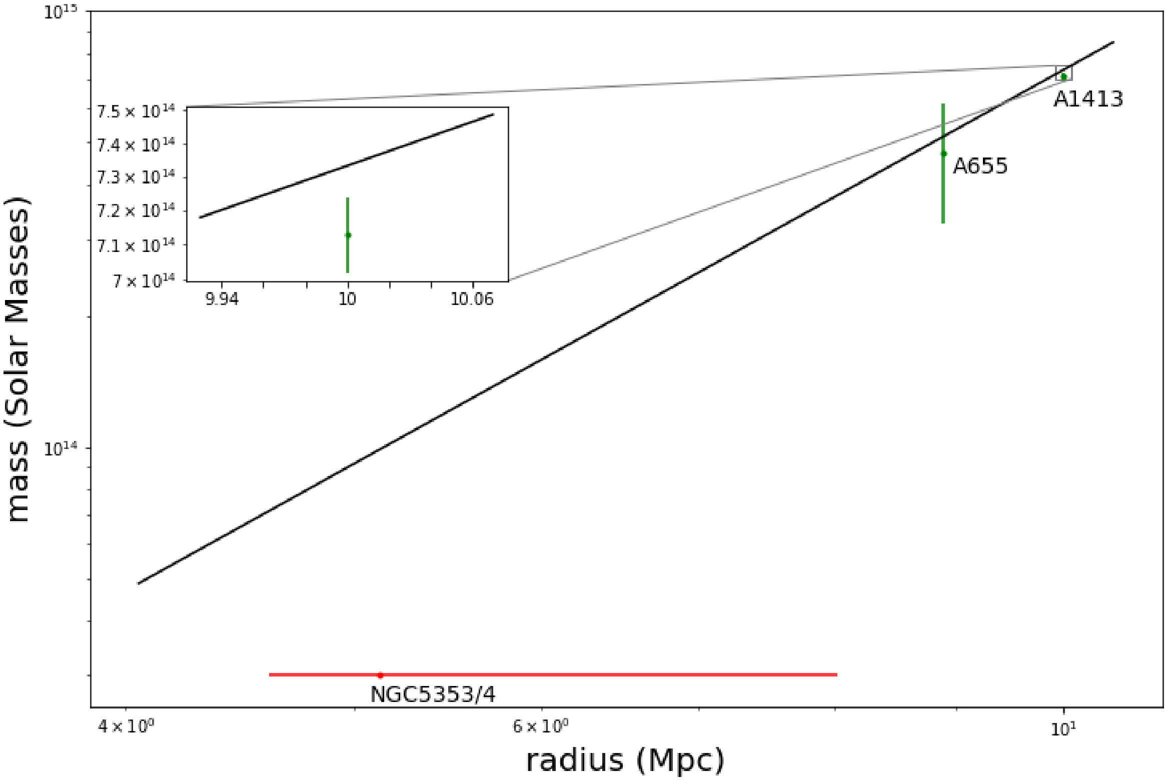

Figure 10-2: Observed masses and radii of the A655, A1413 and NGC5353/4 galaxy clusters. These are the objects with the most significant deviation from the GR prediction, respectively of order 0.19σ for A655, 1.84σ for A1413 (see inset) and $2.61\,\sigma$ for NGC5353/4.

10.3 $f(\mathcal{R})$ theories

In this case, the action is independent of the scalar field, and in the Jordan frame is

$$\mathcal{S} = \int d^4x\sqrt{-g}\left[\frac{1}{2}f(\mathcal{R}) - 2\Lambda + \mathcal{L}_m\right] , \tag{10-14}$$

with the effective gravitational constant given by

$$\tilde{G}_{eff} = \frac{1}{8\pi F}\frac{1+4\frac{k^2}{a^2}\frac{F_{,R}}{F}}{1+3\frac{k^2}{a^2}\frac{F_{,R}}{F}} . \tag{10-15}$$

On sub-horizon scales ($\frac{k^2}{a^2}\frac{F_{,R}}{F} \gg 1$) it reduces to [82]

$$\tilde{G}_{eff} = G_{eff} = \frac{1}{6\pi F} , \tag{10-16}$$

and the turn around radius is given by

$$r_{TA} = \sqrt[3]{\frac{m}{2\pi\Lambda F}} , \tag{10-17}$$

which corresponds to this expression for the GSM

$$m_{gs} = 2\pi\Lambda F r_{obs}^3 . \tag{10-18}$$

Observational data imply $F < (0.0486 \pm 0.0149)G^{-1}$ for A655, $F < (0.0516 \pm 0.0008)G^{-1}$ for A1413, and $F < 0.0051^{+0.0009}_{-0.0171}$ for NGC5353/4. It can noted that GR is not incompatible with observations, since the tightest constraint on F, corresponding to NGC5353/4 is $2.61\,\sigma$ away from the GR limit $F = (6\pi G)^{-1} \approx 0.0531G^{-1}$.

10.4 $\mathcal{R}^n$ theories

For these theories the action is given by

$$f(\mathcal{R}, \phi, X) = \frac{1}{8\pi G}\mathcal{R} + \frac{\alpha}{8\pi G}\mathcal{R}^n, \tag{10-19}$$

and the corresponding effective gravitational constant is

$$G_{eff} = \frac{4G}{3(1+n\alpha\mathcal{R}^{n-1})} = \frac{4G}{3(1+\alpha\beta)}, \tag{10-20}$$

where $\beta = n\mathcal{R}^{n-1}$, which gives the following expressions for the turnaround radius and GSM

$$r_{TA} = \sqrt[3]{\frac{4Gm}{\Lambda[1+\alpha\beta]}} , \tag{10-21}$$

$$m_{gs} = \frac{\Lambda r_{obs}^3[1+\alpha\beta]}{4G}\,. \tag{10-22}$$

In fig.(**10-3**) we plot the regions of the (α,β) given by [87]. In figs. (**10-4**) and (**10-5**) we plot the regions of the (α,β) parameters space satisfying the condition $m_{obs} > m_{gs}$ for A1413 and NGC5353/4 galaxy clusters respectively. The strongest constraints, coming from the NGC5353/4 galaxy, are overlapped with fig.(**10-3**) and plotted in fig.(**10-6**).

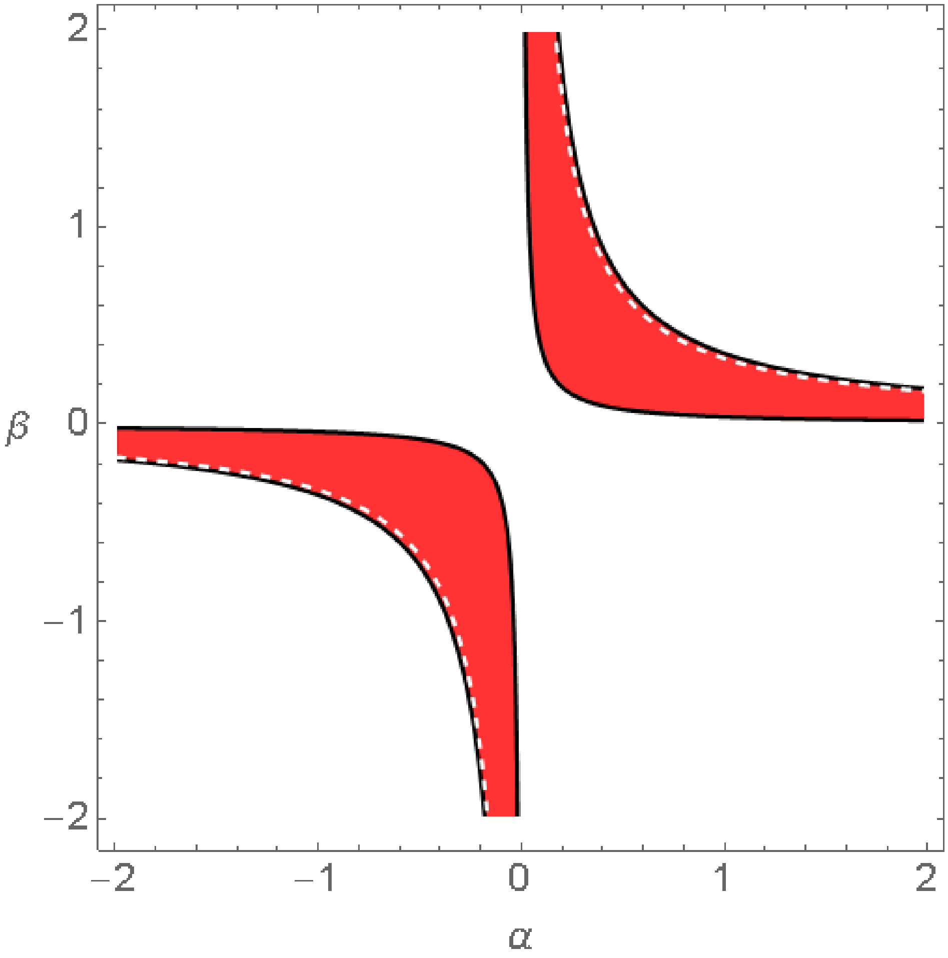

Figure 10-3: Allowed regions of the (α, β) parameters space for R^n theories, respectively in units of Mpc^{2n-2} and Mpc^{2-2n} according to [87]. The white dashed line corresponds to GR.

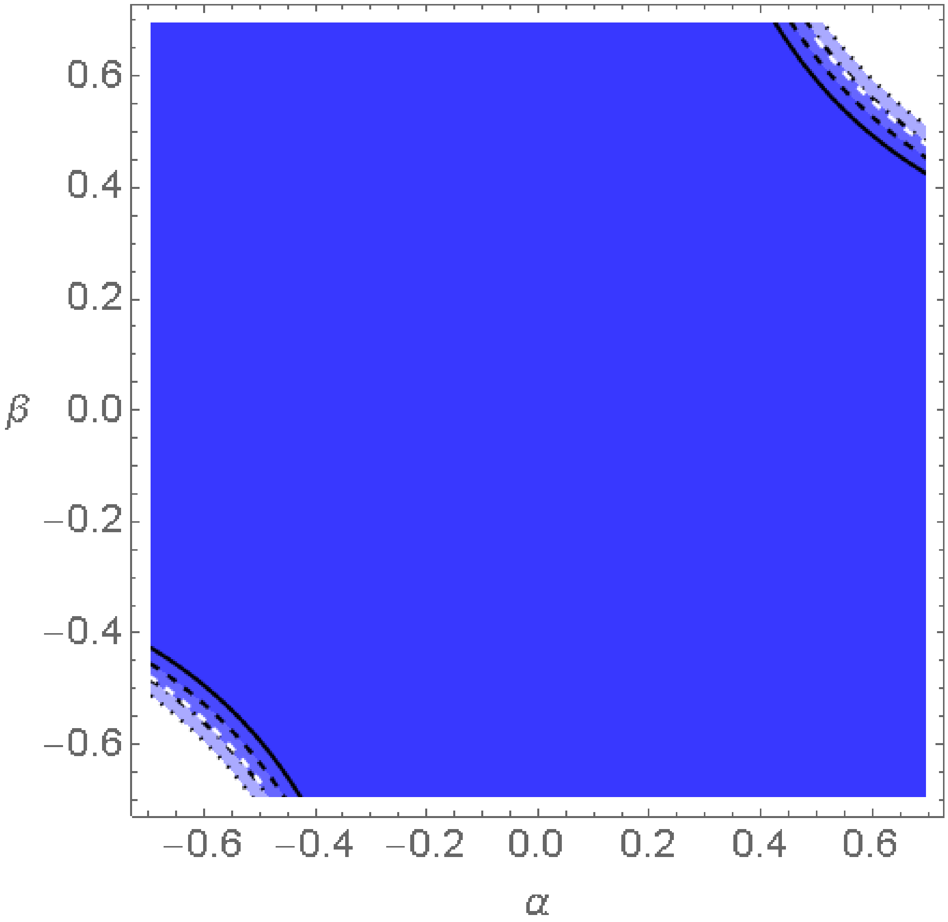

Figure 10-4: Allowed regions of the (α, β) parameters space for $\mathcal{R}^n$ theories, respectively in units of Mpc^{2n-2} and Mpc^{2-2n}. This constraints come from the galaxy cluster A1413. The dark blue region corresponds to $m_{obs} > m_{gs}$ and the other colours to three different confidence bands defined by $m_{obs} + n\,\sigma_m > m_{gs}$, delimited by dashed (n=1), dot-dashed (n=2), and dotted (n=3) lines respectively. The continuous black line corresponds to the parameters which give $m_{obs} = m_{gs}$. The white dashed line corresponds to GR.

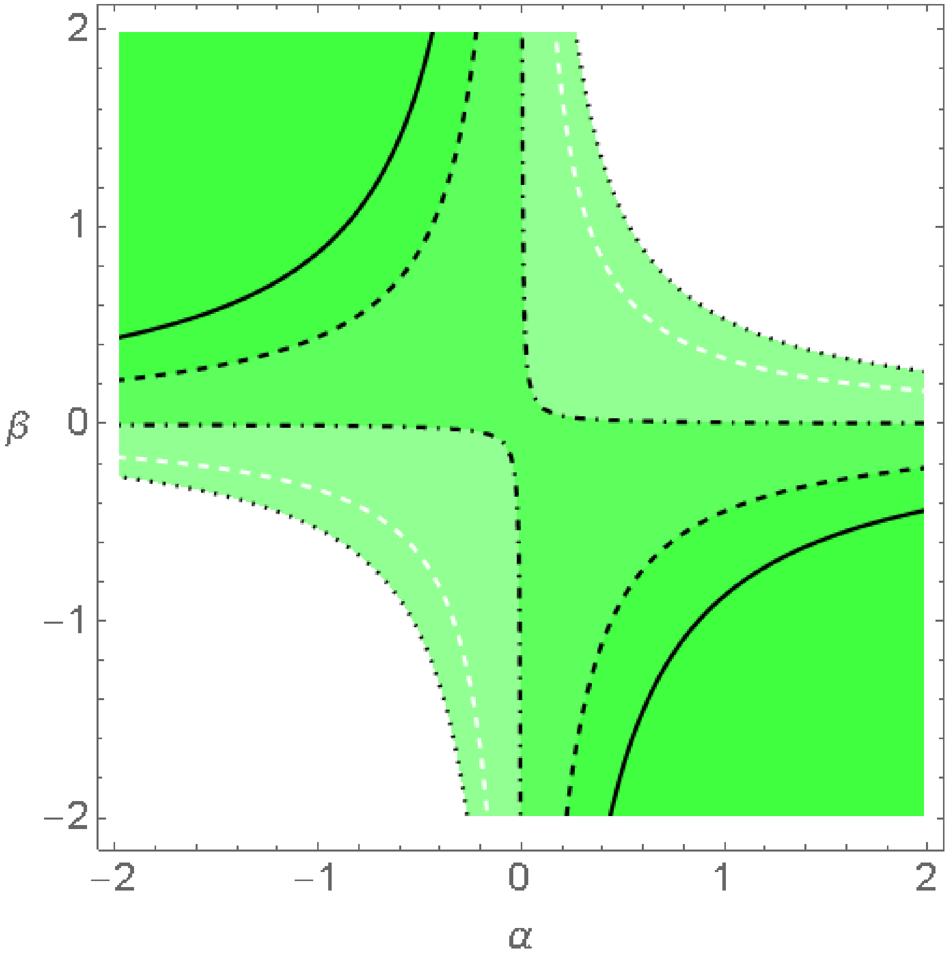

Figure 10-5: Allowed regions of the (α, β) parameters space for $\mathcal{R}^n$ theories, respectively in units of Mpc^{2n-2} and Mpc^{2-2n}. The main constraints come from the galaxy cluster NGC5353/4 studied in [85]. The dark green region corresponds to $m_{obs} > m_{gs}$, and other regions are the confidence bands as defined in fig.(**10-4**). The continuous black line corresponds to the parameters which give $m_{obs} = m_{gs}$. The white dashed line corresponds to GR.

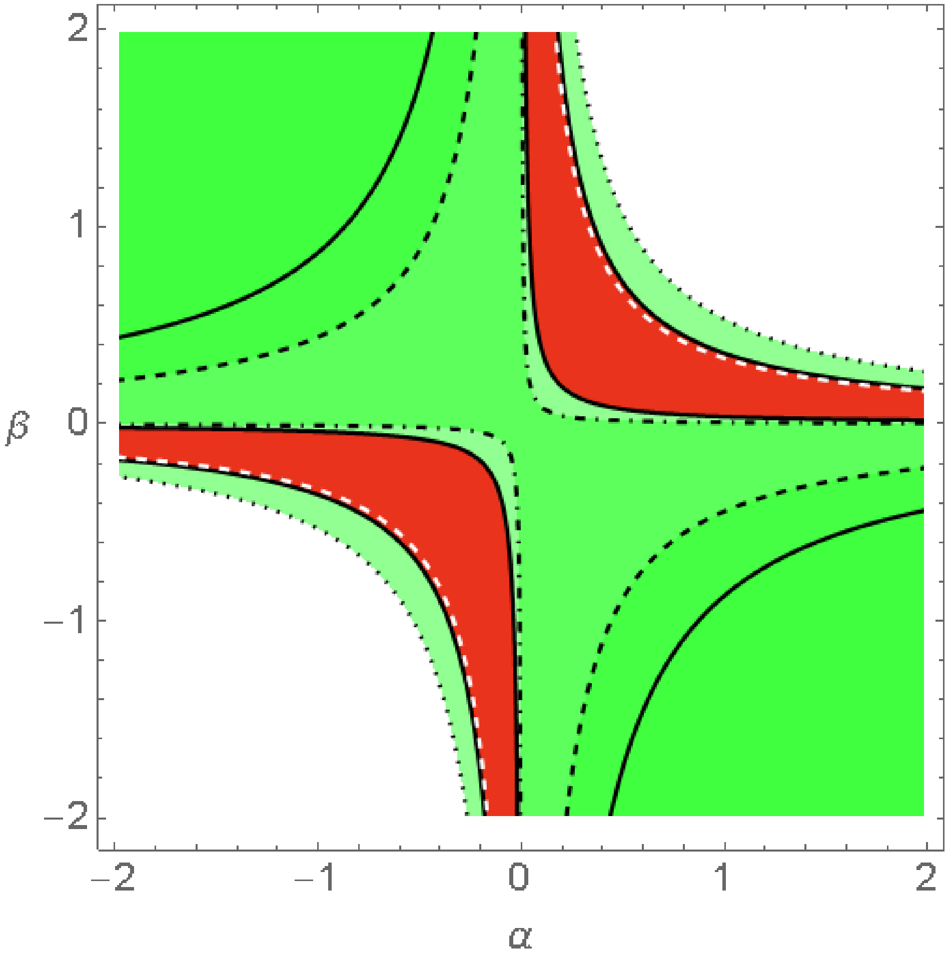

Figure 10-6: Allowed regions of the (α, β) parameters space for $\mathcal{R}^n$ theories, respectively in units of Mpc^{2n-2} and Mpc^{2-2n}. This figure shows the overlapping regions between fig.(**10-3**) and fig.(**10-5**).

10.5 Generalized Brans-Dicke

These theories [88, 89] are a generalization of Brans-Dicke theory [80], with a more general kinetic term, defined by the action

$$f(\mathcal{R}, \phi, X) = \frac{\phi}{8\pi G}\mathcal{R} + \frac{g(\phi)}{4\pi G}X\,. \tag{10-23}$$

After decomposing the scalar field as the sum of a homogeneous background component and a space-dependent perturbative part according to

$$\phi(t, x) = \overline{\phi}(t) + \delta\phi(t, x)\,, \tag{10-24}$$

at leading order in perturbations, the effective gravitational constant is given by

$$G_{eff} = \frac{4 + 2\phi_0\, g_0}{3\phi_0 + 2\phi_0^2\, g_0} G\,, \tag{10-25}$$

where $\phi_0 = \bar{\phi}(t_0)$, $g_0 = g(\phi_0)$, and t_0 is the cosmic time corresponding to the red-shift of the observed structure.

The corresponding turnaround radius and GSM are given by

$$r_{TA} = \sqrt[3]{\frac{3Gm}{\Lambda}\frac{4+2\phi_0 g_0}{3\phi_0 + 2\phi_0^2 g_0}}\,, \tag{10-26}$$

$$m_{gs} = \frac{r_{obs}^3 \Lambda}{3G}\frac{3\phi_0 + 2\phi_0^2 g_0}{4+2\phi_0 g_0}\,. \tag{10-27}$$

The regions of the (ϕ_0, g_0) parameters space satisfying the condition $m_{obs} > m_{gs}$ are shown in fig.(**10-7**) for the strongest constraints, which come from the NGC5353/4 galaxy cluster.

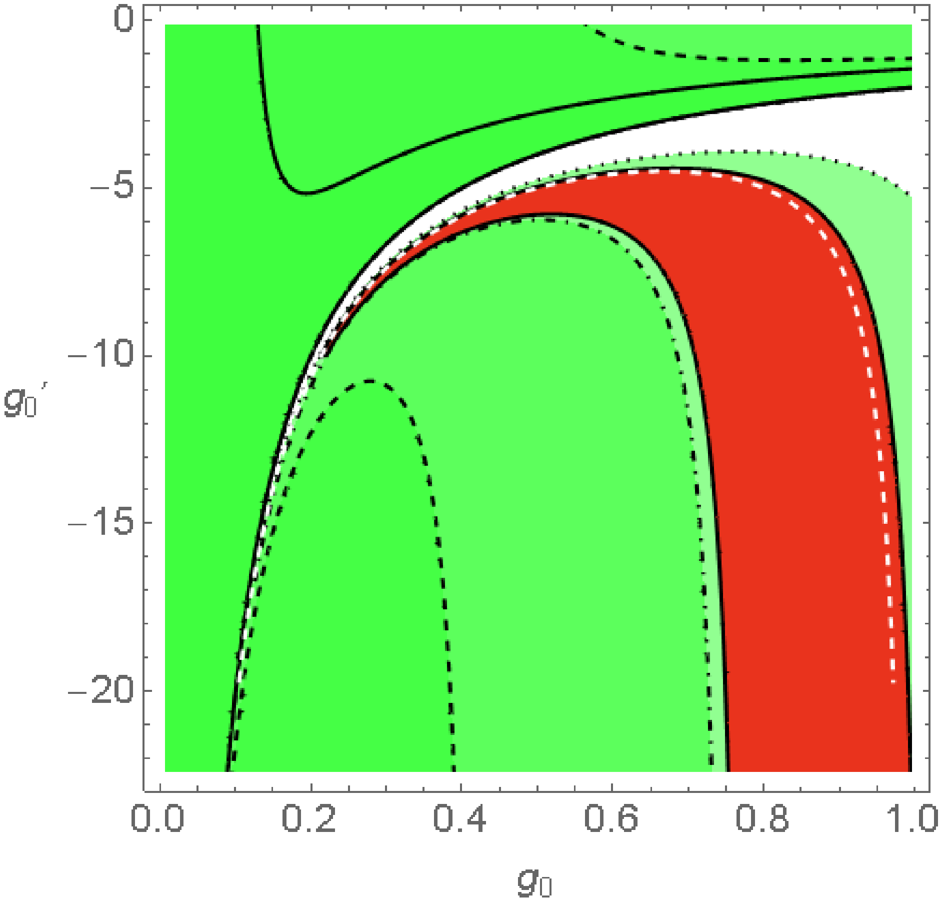

Figure 10-7: Allowed regions of the (ϕ_0, g_0) dimensionless parameters space, for generalized Brans-Dicke theories. The main constraints come from the galaxy cluster NGC5353/4 studied in [85]. The dark green region corresponds to $m_{obs} > m_{gs}$, and the other regions are the confidence bands as defined in fig.(**10-4**). The continuous black line corresponds to the parameters which give $m_{obs} = m_{gs}$. The white dashed line corresponds to the GR limit.

10.6 Quintessence

The action of Quintessence is given by

$$f(\mathcal{R},\phi,X)=\frac{g(\phi)}{8\pi G}\mathcal{R}-\frac{1}{4\pi G}X\,, \tag{10-28}$$

and in this case, the effective gravitational constant is

$$G_{eff}=\frac{G}{g_0}\frac{2g_0+4g_0'^2}{2g_0+3g_0'^2}\,, \tag{10-29}$$

where $g_0=g(\phi_0)$, $g_0'=g'(\phi_0)$, $\phi_0=\overline{\phi}(t_0)$ and the turnaround radius and GSM are given by

$$r_{TA}=\sqrt[3]{\frac{3Gm}{g_0\Lambda}\frac{2g_0+4g_0'^2}{2g_0+3g_0'^2}}\,, \tag{10-30}$$

$$m_{gs}=\frac{g_0\Lambda r_{obs}^3}{3G}\frac{2g_0+3g_0'^2}{2g_0+4g_0'^2}\,. \tag{10-31}$$

We plot in fig.(**10-8**) the regions of the $(\phi_0,\ g_0)$ parameters space satisfying the condition $m_{obs}>m_{gs}$, with the strongest constraints coming from the NGC5353/4 galaxy cluster.

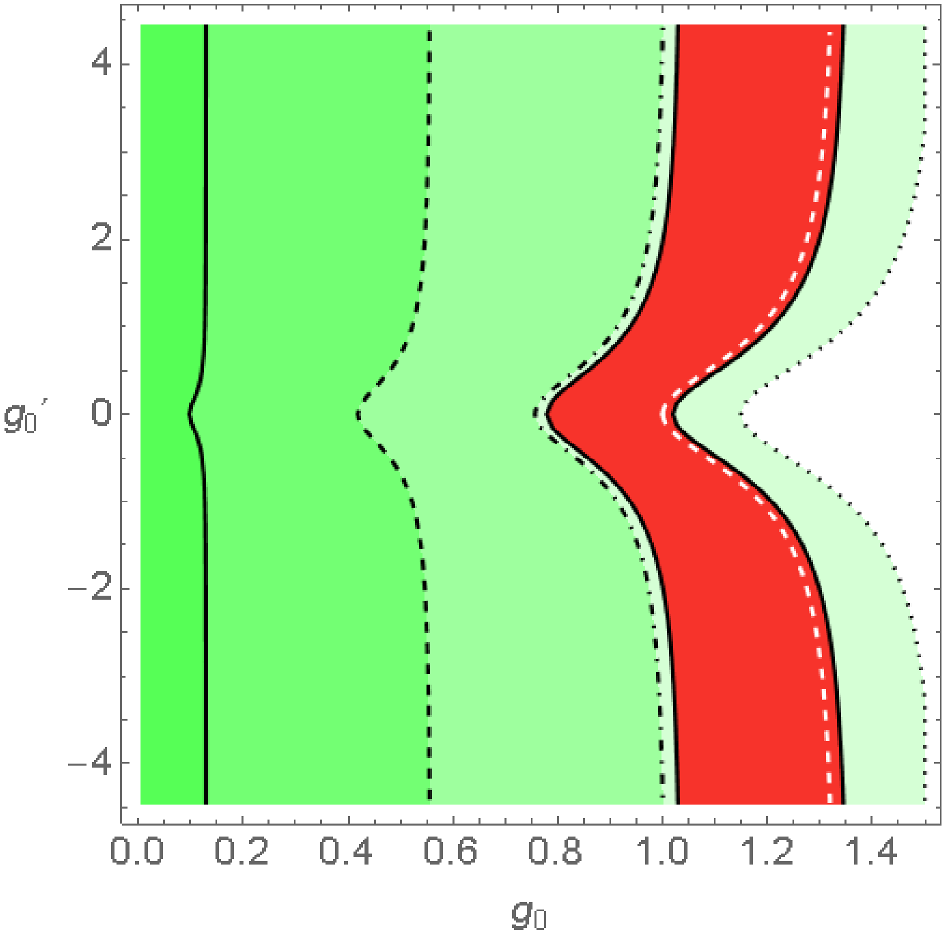

Figure 10-8: Allowed regions of the (g_0, g_0') dimensionless parameters space for Quintessence. The main constraints come from the galaxy cluster NGC5353/4 studied in [85]. The dark green region corresponds to $m_{obs} > m_{gs}$, and the other regions are the confidence bands as defined in fig.(**10-4**). The continuous black line corresponds to the parameters which give $m_{obs} = m_{gs}$. The white dashed line corresponds to the GR limit.

11 Deep learning reconstruction of large scale structure from supernovae luminosity distance

Another significant cosmological effect of gravity is its impact on luminosity distance. The matter content of large-scale structures curves space-time according to Einstein's Field Equations, which modifies the light-like geodesics followed by photons and consequently the luminosity distance. It is possible to reconstruct the matter density field from this effect on the luminosity distance, and this procedure is called the inversion problem [31, 32, 33, 34, 35, 36]. It is a unique method to reconstruct the density field at high redshift where only SNe can be observed. This problem has been solved previously with some numerical and analytical techniques under very restrictive symmetry assumptions [90, 91, 92] such as spherical symmetry, while in this thesis we will develop a completely general approach valid for an arbitrary geometry, based on the use of artificial intelligence.

We want to solve the inversion problem of reconstructing the density contrast and velocity fields from their effects on the luminosity distance using a CNN. To train the CNN architecture in fig.(**11-1**), 10^3 random density and velocity profiles were generated using the nbodykit package [93]. The CNN training set is then obtained by computing the effects of these inhomogeneities on the luminosity distance. Finally, the inversion problem is solved by training the CNN to reconstruct the density and velocity fields from the luminosity distance synthetic data obtained in the previous step.

This chapter is organized as follows: the first section explains how the effects on the luminosity distance are calculated from the density and velocity fields, the second section describes how the random density fields are generated, the third section shows the neural network architecture we adopt, the function which is minimized, and provide details about the training process. In the last sections, we present the results of the inversion.

11.1 Effects of cosmic structure on the luminosity Distance

A direct measurement of cosmological distance, through parallax or triangulation, is only possible for objects that are relatively close to us, while at higher red-redshift, we can only measure the luminosity distance $D_L(z)$.

The luminosity distance is defined as

$$D_L = \sqrt{\frac{L}{4\pi F}}, \tag{11-1}$$

where we denote the observed flux as F and the source's absolute luminosity as L.

We compute the effects of the inhomogeneities on the luminosity distance using the dominating terms in the linear perturbation theory formula [37]

$$D_L(z_S) = (1+z_S)(\chi_0 - \chi_S)(1 - k_v - k_\delta)\,, \tag{11-2}$$

where z is the red-shift, χ is the comoving distance, and k_v and k_δ correspond to the effects [94] of the peculiar velocity and the density contrast respectively

$$k_v = \frac{1+z_S}{(\chi_O - \chi_S)H_s}\boldsymbol{v_O}\cdot\boldsymbol{n} + \left[1 - \frac{1+z_S}{(\chi_O - \chi_S)H_s}\right]\boldsymbol{v_S}\cdot\boldsymbol{n}, \tag{11-3}$$

$$k_\delta = \frac{3}{2}H_0^2\Omega_m\int_{\chi_S}^{\chi_O}\frac{\chi(\chi_S - \chi)[1+z(\chi)]}{(\eta_O - \eta_S)}\delta\,d\eta\,. \tag{11-4}$$

In the above equations, subscripts $_s$ and $_o$ denote quantities evaluated at the source and observer, $\boldsymbol{n}$ is the unit vector between the source and the observer, and $H_S = H(z_S)$ is the Hubble parameter at the source, obtained from the Friedmann's equation

$$H(z) = H_0\sqrt{\Omega_\Lambda + \Omega_m(1+z)^3}\,. \tag{11-5}$$

The red-shift $z(\chi)$ associated with a given comoving distance is obtained by inverting numerically the relationship

$$\chi(z) = \int_0^z \frac{dz'}{H(z')}\,. \tag{11-6}$$

Using eq.(11-2), we obtain the luminosity distance for each cell of the grid. For each simulation, we generate a density profile grid δ_G with L^3 elements, a velocity grid v_G with L^3 elements, corresponding to the line of sight projection of the source velocity $\boldsymbol{v_S}\cdot\boldsymbol{n}$, and a luminosity distance grid D_G with L^3 elements.

11.2 Simulation of cosmic structure

We use nbodykit package [93] to generate the density and velocity fields needed as inputs for calculating the training set. The mock catalogs are generated using Planck 2018 [95] cosmological parameters. Using nbodykit averaging functions, we obtain the density and velocity fields on a discrete three-dimensional grid defined over a cube of edge length 150 Mpc, consisting of 11^3 cubical cells of equal edge length. The mock catalogs obtained in this way have statistical properties in good agreement with the results of N-body simulations [93].

The solution of the inversion problem can be summarized in this way:

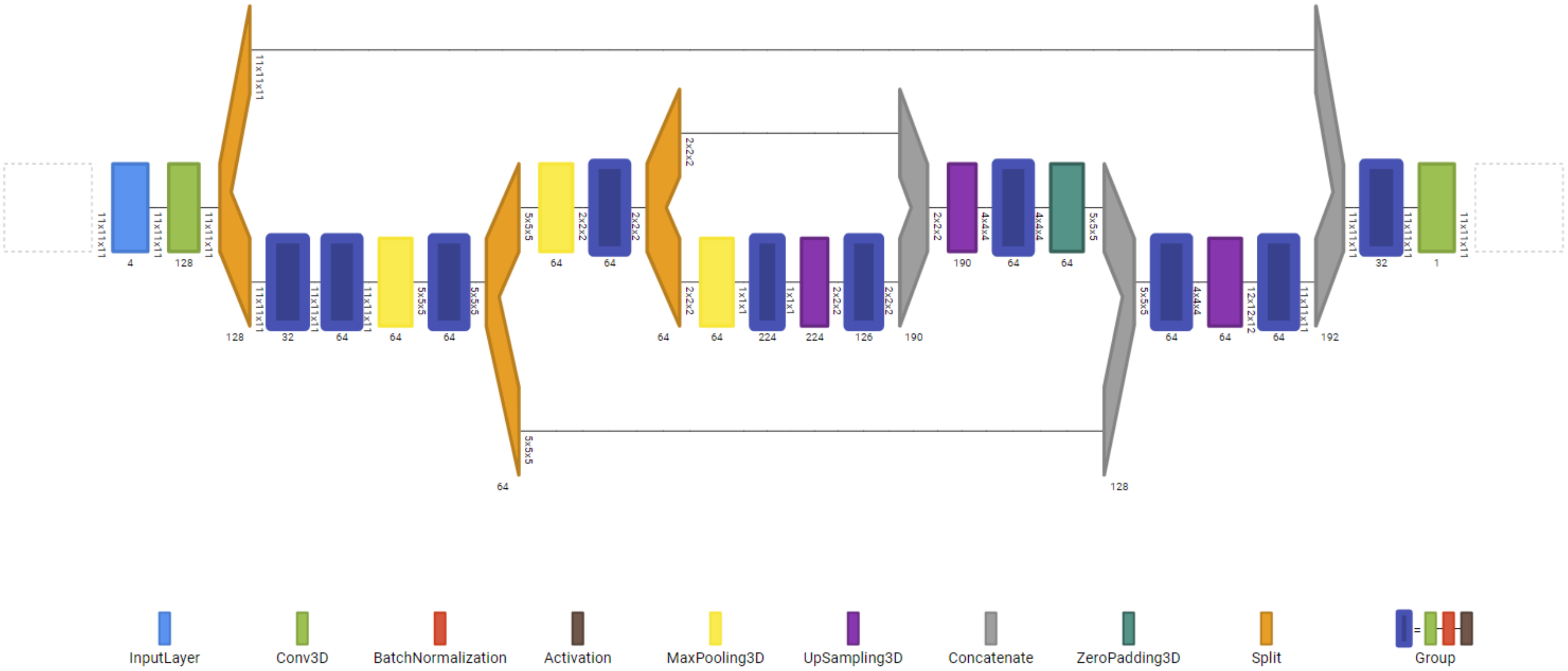

Figure 11-1: Diagram of the neural network used to solve the inversion problem, based on a modified version of U-Net. The colors represent different types of layers, and the grey lines between the split and concatenate layers represent the residual connections. The number under the layers corresponds to the number of channels of the layer.

- generate many random grids for the radial velocity and density fields $\{\delta_G, v_G\}$
- compute the grid $D_G = f(\delta_G, v_G)$ for each $\{\delta_G, v_G\}$ using eq.(11-2)
- train a CNN to invert the above relationship i.e. to obtain $\{\delta_G, v_G\} = f^{-1}(D_G)$

where we are denoting symbolically with f^{-1} the process of the solution of the inversion problem. The solution of the inversion problem is, in general, not unique since different inhomogeneities could produce the same effects on D_L. However, we can train the CNN to minimize the error of the inversion problem within the limits of the above-mentioned intrinsic degeneracy of the inversion problem.

11.3 Neural network architecture

We solve the IP using convolutional neural networks; specifically, a modified version of the U-Net architecture [96]. We train two CNN separately, one for the density field δ_G and another for the velocity field v_G. The architecture is symmetrical and has two main parts: the left part is the encoder, which consists of convolutional layers, while the right side is the decoder. The latter uses nearest-neighbor interpolation to upsample the data, which is used to reconstruct the density and velocity fields from their effects on the luminosity distance.

The simulated input data used to train the CNN is a four-dimensional array of size $11 \times 11 \times 11 \times 4$. This is because for each of the 11^3 cells of the grid, there is the corresponding value D_G and the three spatial coordinates of the cell. This is necessary to provide information about the spatial location of the cells, which is important to determine the effects on the luminosity distance. The outputs of the CNNs are three-dimensional arrays of size $11x11x11$, which corresponds to the density and radial component of the source velocity in each grid cell.

11.3.1 Loss function

We train two different networks, one for δ_G and the other for v_G. In both cases we minimize the loss function given by Mean Absolute Error:

$$MAE(y, \hat{y}) = \frac{1}{m} \sum_{i=1}^{m} \frac{1}{L^3} \sum_{c=1}^{L^3} |y_{ic} - \hat{y}_{ic}|, \qquad (11\text{-}7)$$

where m is the total number of simulations, y_{ic} and $\hat{y}_{ic}$ are the inputted and predicted data respectively for each cell c in each simulation i. We apply early stopping to select the network parameters that best fit the test set to avoid overfitting and have good generalization results.

Since both δ_G and v_G can often have very small values, the Mean Average Percentage Error (MAPE) is not a good measure of the goodness of fit because it can often diverge due to the presence of a small quantity in the denominator. For this reason, we have chosen the MAE as loss function and metric to measure the inversion results accuracy.

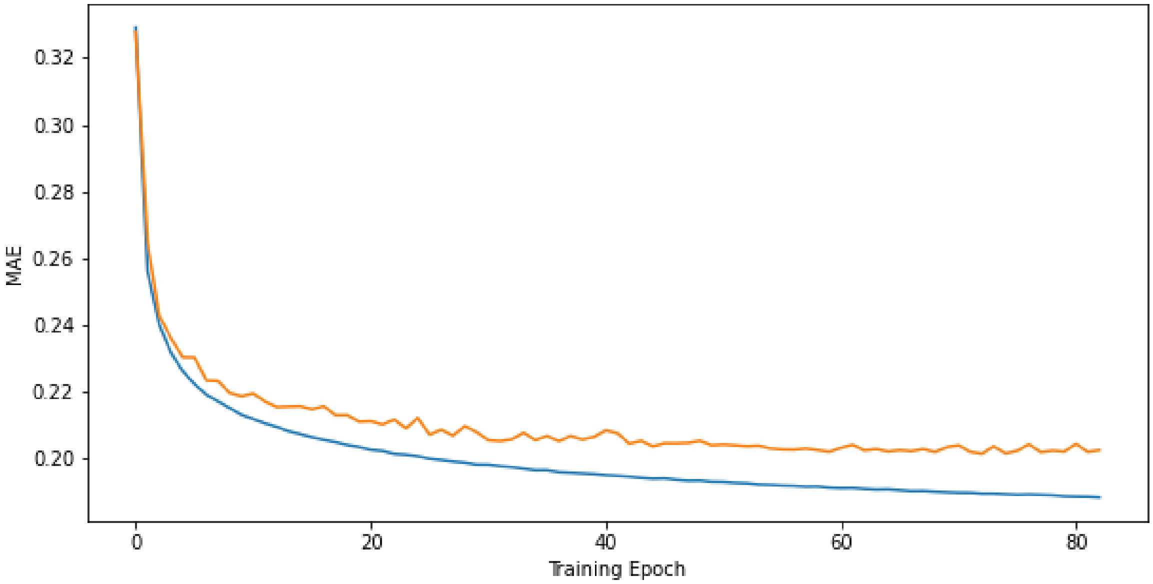

Figure 11-2: Training curves of the Mean absolute error (MAE) for the density contrast δ. The orange and blue curves correspond respectively to the test and training datasets.

11.4 Results of the inversion of the density field

The learning curves for δ are shown in fig. (**11-2**). The probability distribution of the δ field of the test set and the corresponding reconstructed δ obtained applying the neural network to the luminosity distance are shown in fig.(**11-3**). As it can be seen, the reconstructed δ follows approximately the same distribution of the test set, showing that the neural network can recover the statistical properties of the input data set. Different cross-sections of δ_G and their corresponding reconstructions are shown in fig. (**11-4**). The overall pattern is visible on the predicted cross-section. The MAE of the reconstructed δ is 0.2012, which is considerably smaller than the standard deviation $\sigma_\delta = 0.5546$ of the test set, which can be used as a benchmark to assess the efficacy of the inversion.

11.5 Results of the inversion of the peculiar velocity field

The mean absolute error of the source velocity in the line of sight is shown in fig. (**11-5**). There is no apparent overfit between the training and test curves. The distributions of the velocity in the test set and their prediction overlap almost completely, as seen in fig. (**11-6**). The cross-section of the predicted velocity also exhibits the same features as the velocity in the test set, as seen in fig. (**11-7**). The MAE of the reconstruction is $24.3285 km/s$ which is

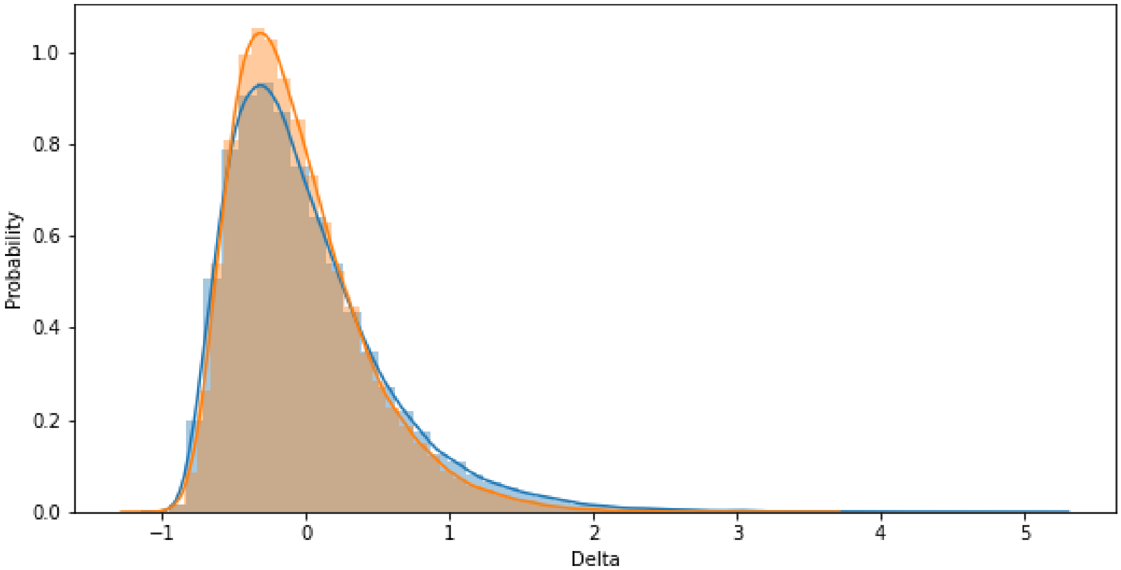

Figure 11-3: Probability distribution of the δ field of the test set (blue), and corresponding reconstructed δ (orange) obtained applying the neural network to the luminosity distance.

much smaller than the standard deviation $\sigma_v = 174.8255 km/s$.

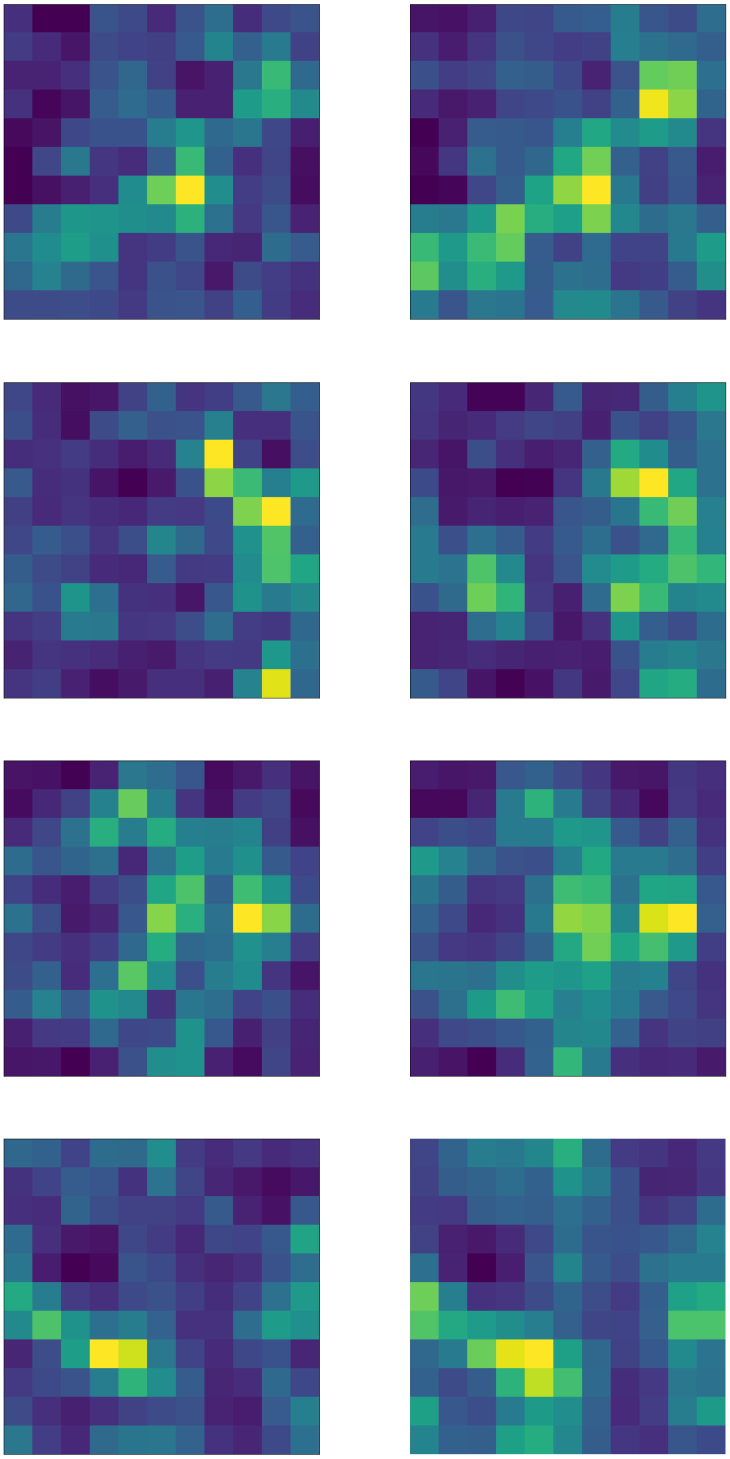

Figure 11-4: Cross-section of the different three-dimensional density contrast fields with a plane perpendicular to the z-axis. The left column is for the test set, and the right column is the corresponding δ reconstructed from the luminosity distance.

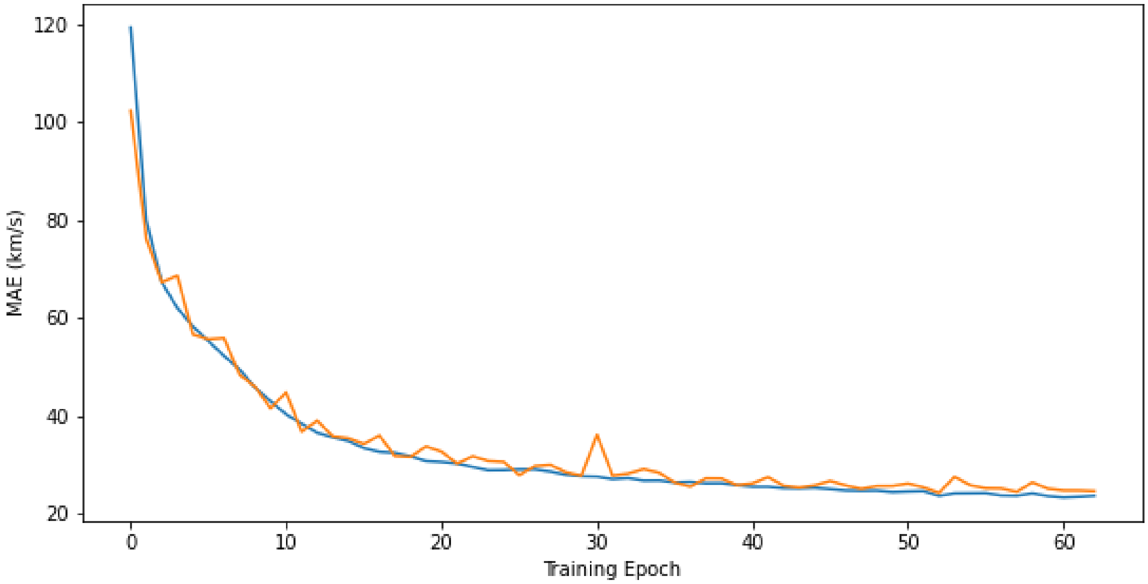

Figure 11-5: Training curve of the Mean absolute error (MAE) of the velocity for the training and test data sets in blue and orange respectively.

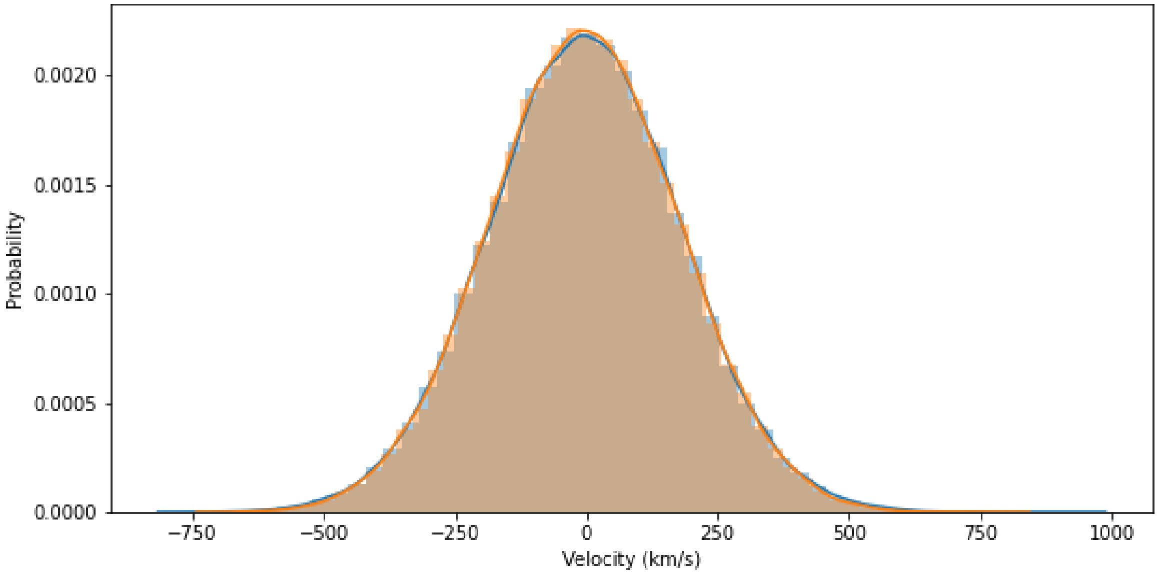

Figure 11-6: Distribution of the velocity of the test set in blue and its reconstruction in orange.

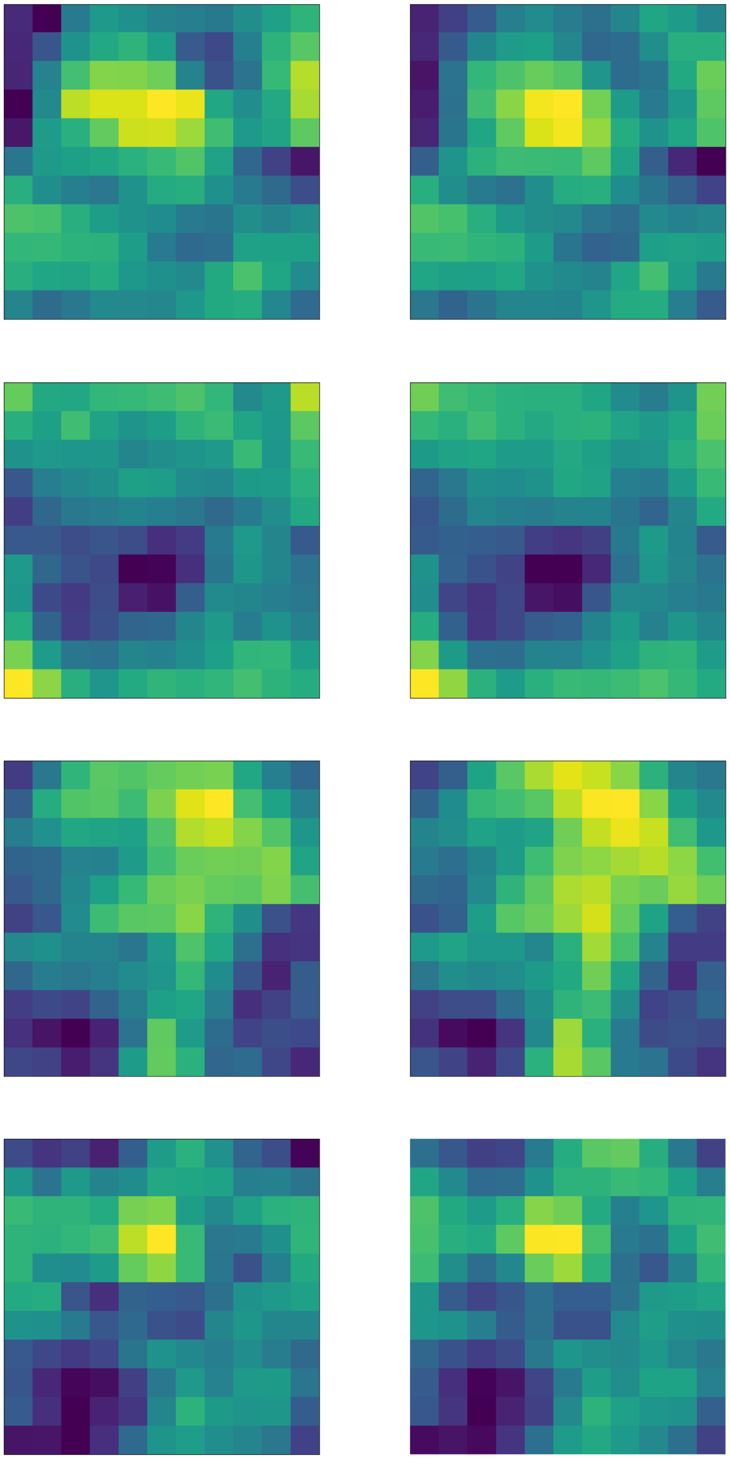

Figure 11-7: Cross-section of the velocity field for different simulations in the test set. The left column corresponds to the velocity field of the test set and the images on the right column are their respective reconstructions.

12 Conclusions

We have studied gravity in the weak and strong regimes in different scenarios. We trained a neural network with frequency domain gravitational-wave data to obtain black hole merger masses in the strong gravity regime. In the weak gravity regime, we computed the Bardeen potentials of SSS metrics and used the corresponding turnaround radius and gravitational stability mass to constrain modified gravity theories using observational galaxy cluster data. Finally, we tackled an inversion problem with a neural network on a cosmological scale, reconstructing the density and velocity fields from the luminosity distance.

In the strong gravity regime, numerical relativity has been used to simulate black hole mergers. The spectrograms of these simulated GW signals have been used to train a new convolutional neural network, FCNN, to determine the merger masses, and compared its performance with other CNN trained on time-domain data (TCNN) [10]. The networks were trained for 1000 epochs using synthetic gravitational wave signals with a 70-30 train/development split, the mean absolute percentage error between the masses and their predictions was minimized. The FCNN was trained on spectrograms, allowing it to reduce the input dimension, resulting in a lower number of parameters in the final fully-connected layers of the network, reducing its variance.

The execution time of the FCNN is, in general, much lower than the TCNN because the FCNNs have much fewer parameters. Adding the computational time of the spectrogram, we obtain a total time which is on average only about 6% greater than that of a CNN working on the time domain data, but with a slightly better MAPE and substantially less over-fit, due to the smaller number of parameters.

Regarding weak gravity, the Bardeen potentials from SSS metrics were computed with cosmological perturbation theory. We applied the method to the Schwarzschild de Sitter metric, confirming it does indeed allow to compute the Newtonian potential correctly due to a point mass in an expanding universe. Using the gauge invariance of the Bardeen's potentials, we have obtained a gauge-invariant definition of the turnaround radius, checking it is consistent with the result obtained in static coordinates for the SDS metric.

We have then applied the method to derive general expressions for the Bardeen's potentials for a class of SSS metrics obtained by adding a term linear in the mass and proportional to a general function of the radius to the de Sitter metric. We have computed the Bardeen's potentials for an SSS solution of the Brans-Dicke theory in static coordinates, confirming the results obtained independently by solving the Brans-Dicke field equations in the Newton gauge. Bardeen's potentials have also been derived explicitly for logarithmic, power-law, and exponential modifications. We applied the method to study SSS metrics which give flat rotation curves. After re-writing them as perturbations of an FRW background, we have computed the energy density radial profile, obtaining the expected behavior together with a contribution from the cosmological constant.

Using the same framework, we have derived the theoretical prediction of the gravitational stability mass for a broad class of scalar-tensor theories, including $f(R)$, Quintessence, and generalized Brans-Dicke. Most of the observations are consistent with GR except the galaxy clusters A655, A1413, and NGC5353/4, which have masses smaller than the GR prediction.

The tightest constraints for GR come from A1413 and NGC5353/4, whose deviation from GR is respectively of order $1.84\,\sigma$ and $2.61\,\sigma$, implying that there is no statistically significant evidence of the need for a modification of GR.

Finally, a set of mock lognormal density profiles with their corresponding velocity profiles were generated using large-scale structure simulations. The direct problem involved the computation of the luminosity distance for each simulation, and the inverse problem was solved by training a fully convolutional neural network with the data generated by the direct problem.

There are different applications of the results obtained in this thesis that would be interesting to apply to observational data. The FCNN could be applied to gravitational-wave data from the LIGO or LISA detector [2]. A new neural network could be designed to estimate additional parameters such as the spin of the black holes. The GSM and TAR could be used to constrain gravity theories using observations from the Euclid mission [97, 98, 99, 100]. The inversion method we have developed could be used to reconstruct the density and velocity fields from future SNe catalogs [101]. It would also be interesting to extend the inversion method to obtain other cosmological parameters.

Apart from applying these analysis methods to new datasets, several theoretical problems could be interesting to investigate in the future. Regarding gravitational waves produced by black hole mergers, it would be interesting to study the effects of modified gravity theories and constrain their parameters using gravitational-wave observations. For the calculation of the GSM and the TAR, non-gravitational physics or deviations from spherical symmetry [102, 103] could be taken into account.

Bibliography

[1] A. Einstein, Sitzungsber. Preuss. Akad. Wiss. Berlin (Math. Phys.) 1915, 831 (1915).

[2] Virgo, LIGO Scientific, B. P. Abbott *et al.*, Phys. Rev. Lett. 116, 061102 (2016), arXiv:1602.03837.

[3] B. F. Schutz, (2000), arXiv:gr-qc/0003069.

[4] B. P. Abbott *et al.*, The Astrophysical Journal 909, 218 (2021).

[5] B. F. Schutz, Nature 323, 310 (1986).

[6] LIGO Scientific, Virgo, Fermi-GBM, INTEGRAL, B. P. Abbott *et al.*, Astrophys. J. 848, L13 (2017), arXiv:1710.05834.

[7] B. P. Abbott *et al.*, Phys. Rev. D93, 112004 (2016), arXiv:1604.00439, [Addendum: Phys. Rev.D97,no.5,059901(2018)].

[8] H. Shen, D. George, E. A. Huerta, and Z. Zhao, (2017), arXiv:1711.09919.

[9] W. Wei and E. A. Huerta, Phys. Lett. B800, 135081 (2020), arXiv:1901.00869.

[10] D. George and E. A. Huerta, Phys. Rev. D97, 044039 (2018), arXiv:1701.00008.

[11] D. George and E. A. Huerta, Phys. Lett. B778, 64 (2018), arXiv:1711.03121.

[12] D. George and E. A. Huerta, Deep Learning for Real-time Gravitational Wave Detection and Parameter Estimation with LIGO Data, in *NiPS Summer School 2017 Gubbio, Perugia, Italy, June 30-July 3, 2017*, 2017, arXiv:1711.07966.

[13] A. Rebei *et al.*, Phys. Rev. D100, 044025 (2019), arXiv:1807.09787.

[14] H. Gabbard, M. Williams, F. Hayes, and C. Messenger, Phys. Rev. Lett. 120, 141103 (2018), arXiv:1712.06041.

[15] X. Fan, J. Li, X. Li, Y. Zhong, and J. Cao, Sci. China Phys. Mech. Astron. 62, 969512 (2019), arXiv:1811.01380.

[16] J. A. Gonzalez and F. S. Guzman, Phys. Rev. D97, 063001 (2018), arXiv:1803.06060.

[17] A. J. K. Chua, C. R. Galley, and M. Vallisneri, Phys. Rev. Lett. 122, 211101 (2019), arXiv:1811.05491.

[18] H. Nakano *et al.*, Phys. Rev. D99, 124032 (2019), arXiv:1811.06443.

[19] J. P. Marulanda, C. Santa, and A. E. Romano, Physics Letters B 810, 135790 (2020).

[20] J. Amaré *et al.*, Physical Review Letters 123 (2019).

[21] H. Stefancic, Phys. Lett. B670, 246 (2009), arXiv:0807.3692.

[22] A. De Felice and S. Tsujikawa, Living Rev. Rel. 13, 3 (2010), arXiv:1002.4928.

[23] T. Clifton, P. G. Ferreira, A. Padilla, and C. Skordis, Phys. Rept. 513, 1 (2012), arXiv:1106.2476.

[24] D. Tanoglidis, V. Pavlidou, and T. Tomaras, (2016), arXiv:1601.03740.

[25] S. Bhattacharya, K. F. Dialektopoulos, A. E. Romano, C. Skordis, and T. N. Tomaras, (2016), arXiv:1611.05055.

[26] V. Faraoni, Phys. Dark Univ. 11, 11 (2016), arXiv:1508.00475.

[27] C. Santa Vélez and A. Enea Romano, JCAP 06, 022 (2020), arXiv:1905.07620.

[28] I. Odderskov and S. Hannestad, Journal of Cosmology and Astroparticle Physics 2017, 060–060 (2017).

[29] N. Brouzakis and N. Tetradis, Physics Letters B 665, 344–348 (2008).

[30] A. E. Romano and P. Chen, The European Physical Journal C 74 (2014).

[31] L. Guasch, O. Calderon Agudo, M.-X. Tang, P. Nachev, and M. Warner, npj Digital Medicine 3 (2020).

[32] Z. Zhang and Y. Lin, Data-driven seismic waveform inversion: A study on the robustness and generalization, 2019, arXiv:1809.10262.

[33] O. Senouf *et al.*, Self-supervised learning of inverse problem solvers in medical imaging, 2019, arXiv:1905.09325.

[34] P. Henzler, V. Rasche, T. Ropinski, and T. Ritschel, Single-image tomography: 3d volumes from 2d cranial x-rays, 2018, arXiv:1710.04867.

[35] Y. Chen and E. Saygin, Seismic inversion by hybrid machine learning, 2020, arXiv:2009.06846.

[36] W. Zhu, K. Xu, E. Darve, and G. C. Beroza, A general approach to seismic inversion with automatic differentiation, 2020, arXiv:2003.06027.

[37] C. Bonvin, R. Durrer, and M. A. Gasparini, Physical Review D 73 (2006).

[38] C. García, C. Santa, and A. E. Romano, (2021), arXiv:2107.05771.

[39] S. Ruder, An overview of gradient descent optimization algorithms, 2017, arXiv:1609.04747.

[40] I. Goodfellow, Y. Bengio, and A. Courville, *Deep Learning* (MIT Press, 2016), `http://www.deeplearningbook.org`.

[41] T. Hastie, R. Tibshirani, and J. Friedman, *The Elements of Statistical Learning*Springer Series in Statistics (Springer New York Inc., New York, NY, USA, 2001).

[42] A. Geron, *Hands-on machine learning with Scikit-Learn and TensorFlow : concepts, tools, and techniques to build intelligent systems* (O'Reilly Media, Sebastopol, CA, 2017).

[43] F. Rosenblatt, Psychological Review 65, 386 (1958).

[44] D. E. Rumelhart, G. E. Hinton, and R. J. Williams, Nature (1986).

[45] K. Fukushima, Biological Cybernetics 36, 193 (1980).

[46] Y. LeCun *et al.*, Neural Computation 1, 541 (1989).

[47] R. d'Inverno, *Introducing Einstein's Relativity* (Oxford University Press, UK (1998)).

[48] J. A. W. Charles W. Misner, Kip S. Thorne, *Gravitation* (W. H. Freeman and Company, UK (2009)).

[49] L. Ryder, *Introduction to General Relativity* (Cambridge University Press, UK (2009)).

[50] J. W. York, Phys. Rev. Lett. 28, 1082 (1972).

[51] G. W. Gibbons and S. W. Hawking, Phys. Rev. D 15, 2752 (1977).

[52] Supernova Cosmology Project, S. Perlmutter *et al.*, Astrophys. J. 517, 565 (1999), arXiv:astro-ph/9812133.

[53] Supernova Search Team, A. G. Riess *et al.*, Astron. J. 116, 1009 (1998), arXiv:astro-ph/9805201.

[54] S. Weinberg, Rev. Mod. Phys. 61, 1 (1989).

[55] A. N. L. M. P. Hobson, G. P. Efstathiou, *General Relativity: An Introduction for Physicists* (Cambridge University Press, (2006)).

[56] D. Lovelock, J. Math. Phys. 13, 874 (1972).

[57] D. Lovelock, J. Math. Phys. 12, 498 (1971).

[58] C. L. Bennett *et al.*, The Astrophysical Journal Supplement Series 208, 20 (2013).

[59] D. Baumann, Cosmology Part III Mathematical Tripos , 77, www.damtp.cam.ac.uk/user/db275/Cosmology/Lectures.pdf.

[60] S. Weinberg, *Cosmology* (Oxford University Press, UK (2008)).

[61] A. Riotto, Inflation and the theory of cosmological perturbations, in *Astroparticle physics and cosmology. Proceedings: Summer School, Trieste, Italy, Jun 17-Jul 5 2002*, pp. 317–413, 2002, arXiv:hep-ph/0210162.

[62] J. M. Bardeen, Phys. Rev. D22, 1882 (1980).

[63] T. Biswas and A. Notari, JCAP 0806, 021 (2008), arXiv:astro-ph/0702555.

[64] R. Durrer, Lecture Notes in Physics , 31–69 (2004).

[65] J. M. Ezquiaga and M. Zumalacárregui, Physical Review Letters 119 (2017).

[66] A. Einstein, Sitzungsber. Preuss. Akad. Wiss. Berlin (Math. Phys.) 1918, 154 (1918).

[67] S. A. Usman *et al.*, Classical and Quantum Gravity 33, 215004 (2016).

[68] A. Raman, 2018 IEEE Global Conference on Signal and Information Processing (GlobalSIP) (2018).

[69] S. Chandrasekhar, *The Mathematical Theory of Black Holes* (Oxford University Press, UK (1983)).

[70] K. Schwarzschild, Sitzungsber. Preuss. Akad. Wiss. Berlin (Math. Phys.) 1916, 189 (1916), arXiv:physics/9905030.

[71] E. Schmutzer, Acta Physica 24, 325 (1968).

[72] G. W. Gibbons, C. M. Warnick, and M. C. Werner, Class. Quant. Grav. 25, 245009 (2008), arXiv:0808.3074.

[73] G. C. McVittie, Mon. Not. Roy. Astron. Soc. 93, 325 (1933).

[74] N. Kaloper, M. Kleban, and D. Martin, Phys. Rev. D81, 104044 (2010), arXiv:1003.4777.

[75] V. Pavlidou and T. N. Tomaras, JCAP 1409, 020 (2014), arXiv:1310.1920.

[76] V. Pavlidou and B. D. Fields, Phys. Rev. D71, 043510 (2005), arXiv:astro-ph/0410338.

[77] V. R. Eke, S. Cole, and C. S. Frenk, Monthly Notices of the Royal Astronomical Society 282, 263–280 (1996).

[78] V. Faraoni, Phys. Rev. D81, 044002 (2010), arXiv:1001.2287.

[79] S. Bhattacharya, K. F. Dialektopoulos, A. E. Romano, and T. N. Tomaras, Phys. Rev. Lett. 115, 181104 (2015), arXiv:1505.02375.

[80] C. Brans and R. H. Dicke, Phys. Rev. 124, 925 (1961), [,142(1961)].

[81] C. G. Boehmer, T. Harko, and F. S. N. Lobo, Astropart. Phys. 29, 386 (2008), arXiv:0709.0046.

[82] S. Tsujikawa, Phys. Rev. D76, 023514 (2007), arXiv:0705.1032.

[83] C. S. Velez and A. E. Romano, JCAP 1805, 041 (2018), arXiv:1611.09223.

[84] H. Yu, A. L. Serra, A. Diaferio, and M. Baldi, Astrophys. J. 810, 37 (2015), arXiv:1503.08823.

[85] J. Lee, S. Kim, and S.-C. Rey, Astrophys. J. 815, 43 (2015), arXiv:1511.00056.

[86] K. Rines, M. J. Geller, A. Diaferio, and M. J. Kurtz, Astrophys. J. 767, 15 (2013), arXiv:1209.3786.

[87] A. Avilez and C. Skordis, Phys. Rev. Lett. 113, 011101 (2014), arXiv:1303.4330.

[88] A. De Felice and S. Tsujikawa, JCAP 1007, 024 (2010), arXiv:1005.0868.

[89] N. Roy and N. Banerjee, Phys. Rev. D95, 064048 (2017), arXiv:1702.02169.

[90] A. E. Romano and P. Chen, The European Physical Journal C 74 (2014).

[91] A. E. Romano, International Journal of Modern Physics D 27, 1850102 (2018).

[92] H.-W. Chiang, A. E. Romano, F. Nugier, and P. Chen, Journal of Cosmology and Astroparticle Physics 2019, 016–016 (2019).

[93] N. Hand *et al.*, Astron. J. 156, 160 (2018), arXiv:1712.05834.

[94] K. Bolejko *et al.*, Phys. Rev. Lett. 110, 021302 (2013), arXiv:1209.3142.

[95] N. Aghanim *et al.*, Astronomy & Astrophysics 641, A6 (2020).

[96] O. Ronneberger, P. Fischer, and T. Brox, U-net: Convolutional networks for biomedical image segmentation, 2015, arXiv:1505.04597.

[97] EUCLID, R. Laureijs *et al.*, (2011), arXiv:1110.3193.

[98] Euclid, I. Tereno *et al.*, IAU Symp. 306, 379 (2014), arXiv:1502.00903.

[99] Euclid, R. Scaramella *et al.*, IAU Symp. 306, 375 (2014), arXiv:1501.04908.

[100] Euclid, J. Amiaux *et al.*, Proc. SPIE Int. Soc. Opt. Eng. 8442, 84420Z (2012), arXiv:1209.2228.

[101] J. Guillochon, J. Parrent, L. Z. Kelley, and R. Margutti, The Astrophysical Journal 835, 64 (2017).

[102] A. Giusti and V. Faraoni, (2019), arXiv:1905.04263.

[103] V. Pavlidou. Private communication